A study on flexible thermoelectric materials with nanostructured oxide semiconductors for wearable power generator

DOCTORAL THESIS

A Study on Flexible Thermoelectric Materials with Nanostructured Oxide Semiconductors for Wearable Power Generator

Khan Faizan

(55645018)

Graduate School of Science and Technology,

Educational Division,

Department of Nanovision Technology,

Shizuoka University, Japan

September 2019

Abstract

In the case of long-term monitoring for patients with chronic diseases, hospitalized patients or the elderly, their activity is restricted due to the wiring of the medical devices. To free patients from these restrictions, low-cost and personalized wireless physiological diagnostic tools are desired. However, for measuring the physiological electric signal such as electroencephalography (EEG), electrocardiography (ECG) and electromyography (EMG), the wireless sensor attached to the body requires a battery for amplifier and transmitter included in the sensor. This leads to a limitation in the device miniaturization and to the frequent exchange of the battery. Therefore, we propose a novel wireless sensor with self-power generation by using wearable thermoelectric devices not only as a power generator from body heat but also as an amplifier of electric signals. For this device, flexible thermoelectric materials with appropriate thermoelectric properties are required to enhance the heat-electricity conversion efficiency. To achieve high power-generation efficiency using thermoelectric technology, it is necessary to increase the thermoelectric figure-of-merit Z, denoted as, $Z = (S^2\sigma)/\kappa$, where S is the Seebeck coefficient, σ is the electrical conductivity and κ is the thermal conductivity of the thermoelectric material. Therefore, it is necessary to achieve an increase in S and a decrease in κ simultaneously. One method of overcoming this issue is the introduction of nanostructured semiconductors due to the confinement effect of carriers and phonons. We have focused our attention on nanostructured ZnO and rGO as a thermoelectric material since ZnO and rGO are easily obtainable materials, they are inexpensive, and moreover, they are non-toxic for human skin. Hence, ZnO and rGO related flexible materials are available for clothing. For a thermoelectric device, however, the characteristics of these materials are not sufficient near room temperature. In our previous papers, although we have measured the Seebeck coefficient of ZnO/cotton-fabric materials, it was obtained by applying the temperature gradient along the layer plane (in the horizontal direction). However, the temperature gradient must lie along the thickness direction of the layer (in the vertical direction) for practical use of wearable devices. There are some reports related to the evaluation of the Seebeck coefficient in the vertical direction of the sample. However, these Seebeck coefficient measurements were applied not to the flexible layer materials but bulk or rigid materials. Also, since the cotton fabric is an insulator, less power in the vertical direction may be obtained due to its small electric current. Therefore, we have focused on conductive carbon fabric (CAF), nickel-copper fabric (NCF) and silver fabric (50% Ag), as a flexible substrate. Many researchers worked on the Seebeck coefficient and electrical conductivity of flexible materials such as carbon fiber, nickel foam. However, none reported the thermoelectric properties of these fabrics, especially in the vertical direction. In this study, we have fabricated nanostructured ZnO and rGO materials over three conductive fabrics using a two-step hydrothermal method. Different morphologies were

prepared by altering the reactant's concentration ratio, growth time, annealing temperature and analyzed by x-ray diffractometer (XRD), scanning electron microscopy (SEM) and energy dispersive x-ray (EDX) analysis. Furthermore, we constructed systems for the measurement of Seebeck coefficient and electrical conductivity of flexible layer material in the vertical direction. It will be demonstrated that the Seebeck coefficient of these fabrics in the vertical direction is close to that evaluated in the horizontal direction. Moreover, the influence of air on the Seebeck coefficient in the stacked fabric layers will be presented.

Acknowledgement

Praise is to Allah forever for His everlasting love and compassion and for granting me the strength and passion for pursuing this doctoral course. I would like to express my deep sense of gratitude and indebtedness with full honour and respect to my supervisor, **Prof. Hiroya Ikeda**, who accepted me as a doctoral student in his laboratory and continuously inspired me during all stages of my research. His constant encouragement and concern during the execution of the present work will be remembered with gratefulness for all time to come.

I would like to give my sincere gratitude to **Prof. Yasuhiro Hayakawa**, who helped me with his precious advice. He allowed me to work in his laboratory without any restrictions.

I express my regards to **Dr. Yuhei Suzuki, Prof. Mani Navaneethan**, and **Dr. J. Archana**, who supported me with their advice, moral support and kind cooperation they extended to me in their capacity as faculty members in Department of Graduate School of Science and Technology. I extend my special thanks to my seniors **Prof. V. Pandiyarasan, Mr. Chandra Prakash Goyal** and **Ryoko Sakai**, for helping me during this research almost every day. I will pray to the GOD to bless me with these kinds of seniors and staff member in my future life also. I would like to say thanks to all my friends for their great support, which helped me to persevere in my moments of self-doubt. The enjoyable moments spent with them will always be memorable. I thank all those who have contributed directly or indirectly to this work. Most of all, precious thanks to my parents, who bravely sent me to Japan for my further studies and prayed for me in every second of my life. Finally, I would like to express my heartfelt thanks to all the committee members **Assoc. Prof. Yoichiro Neo, Prof. Naoki Wakiya, Prof. Kazuhiko Hara** for their proper guidance, valuable comments and suggestions on this thesis.

Contents

Chapter 1: Introduction and Literature Review

1.1. Background

With an increase in everyday consumption of nonrenewable energies such as oil, coal, natural gas, in the form of daily life activities such as powering our vehicles, electricity for our electronics gadgets, household, etc., it became a matter of concern to think over it. Finding the best solution to minimize the wastage of these resources without reducing the consumption or effecting the daily lifestyle is a big problem. On the other hand, expectations from renewable energy resources have also been increased under the growing concern of environmental issues such as global warming and depletion of energy resources [1].

The sudden hike in personal electrical and electronic devices over recent decades has increased demand for electricity power [2]. Despite an immense reduction in energy consumption, still personal electronic devices face issues of maintaining enough power supply, especially the devices required to run continuously in such a state where fixing battery or being charged with alternating current line cord is difficult. Examples of such conditions include electronics implantable for environmental monitoring devices or medical purposes, systems built-in wireless monitoring for health care or devices used for biometric parameter collection, and systems used by individual soldiers. Providing power to these devices with external batteries restricts their flexibility and ability to work at a large distance, while the frequent discharging and again recharging of these batteries may cause reliability issues [3]. A device that is highly efficient, self-sustaining, maintenance-free is highly desirable but challenging to develop. One solution to this issue can be counteracted by using thermoelectric power generators (TEGs). These generators have the ability to convert waste heat directly into electricity.

.

1.2. Motivation of current work (wearable thermoelectric power generator)

A lot of strategies were considered for the development of wearable thermoelectric power generator (WTEG). Solar cells based on the irradiation of light source, which is restricted to the availability of light source during the conversion hours. Piezoelectric, electrostatic or electromagnetic power generators rely on the continuous mechanical motion for their working. However, it is totally impractical for the human body to be in continuous motion, especially for the ill or elderly. Pyroelectric generators rely on short term temperature of the whole material, rather than temperature gradient making these types of generators impractical as well. However, the temperature difference between the surrounding environment and our body is ideal for thermoelectric conversion (TE) because the generation of electricity in the TE device is based on the temperature difference.

A promising solution of integrating power generator with flexible fabrics gives a hope to provide electricity to our electronic gadgets. An ideal wearable power generator should not only convert waste heat into energy but also be light in weight, non-toxic to human body, easy

wearable, and washable. At this stage, it is imperative to integrate power supply with flexible fabrics [4]

Using commercial TE thermopile flexible TEG has already been prepared [5], using different substrates such as Bi-Te based alloy [6],[7], polymer composite, glass plate, silicon wafer or plastic film [7]. Several alloys show promising results, but the best performance was given by Bi-Te based alloy at room temperature (RT). However, their applications are limited because of their potential toxicity and poor processing [8], [9]. None of the flexible devices is practically wearable due to their impermeability. Therefore, combining these devices, along with wearable fabrics, may harm our body and will not allow air and moisture to pass through it. It is important to focus on materials and fabrics that are comfortable to wear and provide enough TE power generation. An example of WTEG is shown in Fig.1.

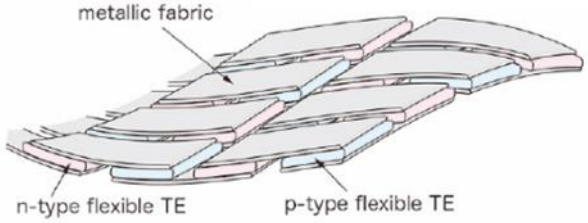

Fig 1. An example of WTEG

1.3. History of wearable thermoelectric power generator

- In 1980, it was Bulova who first showed the Thermatron at a watch fair. It is based on the Seebeck effect to generate energy and power the quartz movement. Using this technology, the Centre Electronique Horloger (CEH) in Neuchâtel - which has now changed into CSEM developed watches which run on the body heat. The Thermatron used two metal sheets, one of which connected to the backside (case, which is in contact with the human wrist) and another one to the top of the case, which acted as a TE generator [10].

- In 1988, two Japanese brands, Seiko and Citizen, gave a great boost in the market by developing their first watch based on thermoelectric. 22 μW of electrical power with an electrical efficiency of 0.1% was the unique qualities of this watch under normal usage conditions. This opens and idea for watchmakers to think more and more to show their expertise in the field of TE and develop watches that take enough heat from the human body for their proper functioning. Similar to the trend of automatic watches for decades, TE watches would be the next big thing in the watch industry [11]

Figure 2: A thermoelectric watch

- In 2010, European telecommunications provider, Orange, came out with a new prototype of a pair of special rubber boots that convert waste heat from your feet into electrical power. The reported electricity generated was enough to charge battery-powered handhelds, such as cell phones. Walking for 12 hours can charge your mobile phone for an hour. Conclusively, running for longer distance will produce more heat, and hence more electricity will be delivered. These boots are environmentally friendly, sustainable and are alternatives to external electrical power sources used to charge our electrical gadgets. Since everyone has to move anywhere every day, so they were practical too. Thermoelectric modules in the form of n-type and p-type semiconductors that forming a thermocouple are arranged in their power generating soles. The first thermopile is created by connecting thermocouple electrically, forming an array of multiple thermocouples, then sandwiched in between two thin ceramic wafers. One surface of ceramic wafer becomes hot due to continuous heat supply from our body, and another one becomes cold (surface to the outer part), and hence capable of generating heat [12]

Figure 3: Wearable thermoelectric boots

- In 2014, a team of The Korea Advanced Institute of Science and Technology (KAIST) headed by Byung Jin Cho, a professor of electrical engineering developed an extremely light in weight and flexible glass fabric based TE generator, which is capable of generating electricity directly from the human body. The extent of flexibility is so unique that the allowable bending radius of the generator is as low as 20 mm. Further, the device will work under normal conditions even if the generator bends upward and downward for up to 120 cycles [13].

Figure 4. Flexible glass based TEG

- In 2018, Choong Sun Kim et al. from KAIST reported self-powered wearable electrocardiography using a wearable TEG. Using body heat as a source Choong Sun Kim developed a wearable TE generator that can sense ECG signal, this generator was fabricated on flexible PCB. Flexible heat sink based on polymer and fiber that enhances liquid evaporation is devised to get a large temperature difference. For the first 10 minutes, the output power density was 38 $\mu W/cm^2$, and after 22 hours of continuous driving of a circuit, it was reported as 13 $\mu W/cm^2$. According to researchers, to drive the ECG system, including the sensors and the power management circuits continuously, the power, as mentioned above, is high enough and satisfactory [14].

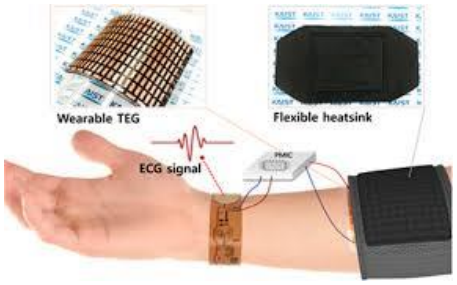

Figure 5. A self-powered ECG set up [14]

1.4. Thermoelectric effect

It was Thomas Johann Seebeck a Baltic German physicist , who, in 1822, who observed TE effect, he proposed the first TE generator that converted heat energy into voltage. According to the basic definition of the TE effect, it is defined as the phenomena of direct conversion of temperature differences to electric voltage and vice versa through thermocouple. In 1834, Jean Charles Peltier a French physicist reported thermoelectric refrigeration, reverse of Seebeck effect. In the mid of 19th century, Irish-born William Thomson (Lord Kelvin) completed the thermoelectric theory by compiling the observation of Seebeck and Peltier. In the subsequent sections will review these three effects and look at their contribution to the thermoelectric figure-of-merit ZT [15]:

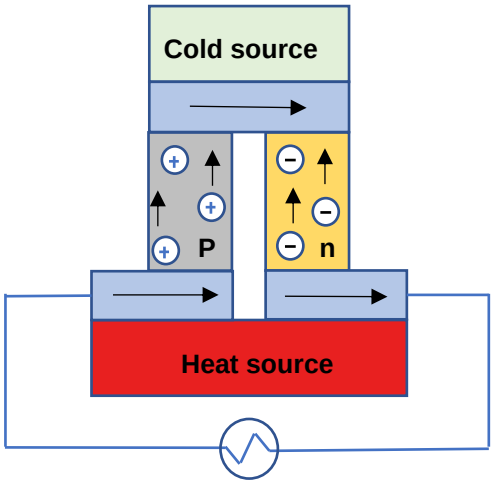

Figure 6. A basic thermoelectric circuit

1.4.1. Seebeck effect

The conversion of heat directly into electricity at the junction of different types of wire is known as Seebeck effect. Consider a rod of finite length of a conducting material that is heated at one end only. Due to this heating, a temperature gradient will occur inside the rod causes the charge carriers to flow from the heated side to cooler side. Below critical temperature, entropy is transported by the charge carriers present in the material, except for superconductors. These charge carriers will continue to move to the cooler side of the material until and unless an

equilibrium state is established as shown in the figure. More and more charge carriers will flow on increasing the temperature gradient from the equilibrium. Increasing the temperature gradient from the equilibrium state will cause more charge carriers to move to the cooler side establishing a new potential difference. Generation of maximum voltage (Vmax) is then limited by the melting point (Mp) of the material [15].

1.4.2. Peltier effect

This effect is defined as the production of temperature difference at two different electrical junctions of two different conductors, when a certain voltage is applied. The generation of Peltier heat per unit time is defined as $Q = (\pi B - \pi C) I$, where πB is the Peltier coefficient of conductor B and πC is that of C, I is the current from B to C [15].

1.4.3. Thomson effect

Whenever a current is passed through a portion of single conductor having temperature gradient, there will a production of heat. This statement can be concluding as $q = \beta I \Delta T$, where q is heating rate, I is the electric current, ΔT is the temperature difference and β is the Thomson's coefficient [15].

1.5. Thermoelectric materials

As one of the energy-harvesting devices, the WTEG has attracted significant attention since it can reuse the waste heat as an electric power. For this device, flexible TE materials with appropriate TE properties are required to enhance the heat-electricity conversion efficiency. To achieve high power-generator efficiency using TE technology, it is necessary to increase the TE figure-of-merit Z, denoted as

$$Z = \frac{S^2 \sigma}{\kappa} \quad , \qquad (1)$$

where S is the Seebeck coefficient, σ is the electrical conductivity and κ is the thermal conductivity of the TE material [16]. Generally, metals have low Seebeck coefficient values and high in thermal conductivity values, which cannot be compensated by their high electric conductance. Conversely, insulators have very high Seebeck coefficient, but having high electrical resistivity. Semiconductors are positioned in the middle of metals and insulators, as shown in figure 7 [17]. Therefore, it is necessary to achieve an increase in S and σ and a decrease in κ, simultaneously. One method of overcoming this issue is the introduction of nanostructured semiconductors due to the confinement effect of carriers and phonons [18]-[20]. One method to achieve high figure of merit is introduction of nanostructured semiconductors.

Nanostructures are expected for the enhancement of the figure of merit because of the following reasons; (i) A decrease in the thermal conductance by an increase in boundary scattering of phonons, and (ii) enhancement of Seebeck coefficient since the electron confinement effect raises the energy which is carried by electrons. For the fabrication of high performing TE materials the selection of material plays an important role. Although, conducting polymer (CP) are favorable materials for the application of thermoelectric but most of the CPs such as polyaniline, polypyrrole, and poly (3,4-ethylenedioxythiophene), polystyrene sulfonate (PEDOT:PSS) are expensive and required complex treatments to achieve good electrical conductivity. Many researchers focus their attentions on oxide nanomaterials for wearable power generators that may provide maintenance free system, environmentally stable, mechanically flexible, cost effective and light in weight.

We have focused our attention on nanostructured ZnO and rGO as TE materials [21], [22], since these are easily obtainable and inexpensive, and moreover, they are nontoxic for human skin. Hence, ZnO and rGO related flexible materials are available for clothing. From point of TE view, however, characteristics of ZnO and rGO are not sufficient near room temperature. In our previous papers [21], [22], although we have measured the Seebeck coefficient of ZnO/cotton-fabric materials, it was obtained by applying the temperature gradient along the layer plane (in the horizontal direction). However, the temperature gradient must lie along the thickness direction of the layer (in the vertical direction) for a practical use of wearable devices. There are some reports related to the evaluation of the Seebeck coefficient in the vertical direction of the sample [23] - [25]. However, these Seebeck coefficient measurements were applied to bulk or rigid materials, not the flexible layers materials in which we are interested

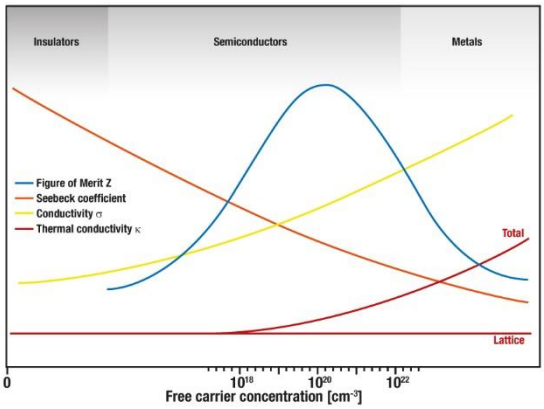

Figure 7: Dependence of Seebeck coefficient, conductivity, thermal conductivity, and figure of merit with respect to free carrier [17]

1.6. Conducting fabrics

Since the cotton fabric is an insulator, less power in the vertical direction may be obtained due to its small electric current. Therefore, we have focused on different conductive fabrics such as carbon fabric (CAF), nickel-copper (NCF) and silver fabric as a flexible substrate. Many researchers worked on the Seebeck coefficient of flexible materials such as carbon fiber [26] - [29], nickel substrate [30] - [31], and other substrates. However, none reported the TE properties of flexible fabrics, especially in the vertical direction. In this study, we constructed a system for measuring the Seebeck coefficient and electrical resistivity of flexible layer

material in the vertical direction and evaluated that of CAF, NCF and silver fabric. It will be demonstrated that the Seebeck coefficient of these fabric layers in the vertical direction is close to that evaluated in the horizontal direction. Moreover, the influence of air on the Seebeck coefficient in stacked layers will be presented.

Although, Seebeck coefficient is the most important parameter in the equation (1) of the figure of merit (Z), as Z is directly proportional to the square values of Seebeck coefficient, which is linearly varying to the other parameters. Besides linear relationship of electrical conductivity with figure of merit, σ is one of the important parameters which decides the value of figure of merit. Several researchers reported a lot of techniques to increase the conductivity such as introduction of metal doping [32], metal salts [33], heating [34] and so on. In this study we chosen different conducting fabrics to enhance the electrical conductivity and hence figure of merit and study the formation of ZnO and rGO oxides over them. These fabrics have different basic properties and different application some of them are listed as follows:

1.6.1. Nickel copper fabric (NCF)

This fabric is purchased from Beijing, China. NCF contains 23% of copper, 27% of nickel and 50% of polyester. The thickness of NCF is 0.27 mm, yarn count is 80D, weight- 100gm/sqm, shielding efficiency is greater than 99.9%. Some of the applications of NCF are listed below:

- Movable field-operation shielding room
  Besides the enormous application of NCF these fabrics are applicable to field conditions, to prevent the emission of electronic devices and they provide high information security from electromagnetic leakage. Moreover, they can be used in providing field conditions, operational command room, important communications hub, confidential room for checking electromagnetic information leakage and provides protection.

- Movable shielding laboratory
  NCF, Conductive fabrics are eco-friendly fabric, can be applied to the human body and have household uses. For example, they are used in enterprise, in many laboratories which uses them for the purpose of detection, measurement, and other research-related fields. These fabrics are resistant up to high temperatures and can be used in daily life such as shielding bags, curtains, and containers for cell phone, communication repeater, laboratories in school, organizations, and semi-conductor production lines, etc [35].

1.6.2. Carbon fabrics (CAF)

Used fabric in this thesis was purchased from Sainergy fuel cell India pvt. ltd, weave

construction plain, wrap per(cm)-19.3, weight- 132 g/m, thickness- 0.25 mm. Several reports are available on carbon fabric, since carbon fibers are highly conducting and having application not only in TE but also in aerospace, automotive, and goods industries [36].

1.6.3. Silver fabrics (50% Ag)

Used silver fabrics contain 50% silver and 50% nylon, yarn count is 40D, weight is 80gm/sqm, shielding effect is more than 99.9% and attenuation 40-60 dB. This fabric is comfortable to wear, easy to wash. This fabric is also having a lot of applications such as, health protection, computers, telecommunications, radio and television, medical and scientific research institut es, etc.

References

1. Yuhei SUZUKI, Faiz SALLEH, Yoshinari KAMAKURA, Masaru SHIMOMURA and Hiroya IKEDA, Phonon-Drag Effect on Seebeck Coefficient in Co-Doped Si Wire with Submicrometer-Scaled Cross Section, Ieice trans. electron., e100–c, 5, 486-489, 2017
2. Krupenkin, T. & Taylor, J. A. Reverse electrowetting as a new approach to highpower energy harvesting. Nat. Commun., 2, 448, 2011.
3. Mercier, P. P., Lysaght, A. C., Bandyopadhyay, S., Chandrakasan, A. P. & Stankovic, K. M. Energy extraction from the biologic battery in the inner ear. Nat. Biotechnol., 30, 1240–1243, 2012.
4. Yong Du, Kefeng Cai, Song Chen, Hongxia Wang, Shirley Z. Shen, Richard Donelson & Tong Lin, Thermoelectric Fabrics: Toward Power Generating Clothing, Sci Rep, 5, 6411, 1-6, 2015
5. Leonov, V. Thermoelectric energy harvesting of human body heat for wearable sensors. IEEE Sens. J. 13, 2284–2291, 2013.
6. J. Lee, H.J. Kim, L. Chen, S. H. Choi, G. N. Mathur, V. K. Vardan, Development of thermoelectric inks for the fabrication of printable thermoelectric generators used in mobile wearable health monitoring systems. Proc. SPIE 8691, 86910R, 2013.
7. L. Francioso, C. De Pascali, A. Taurino, P. Siciliano and A. De Risi, Wearable and flexible thermoelectric generator with enhanced package. Proc. SPIE 8763, 876306, 2013
8. Q. Yao, L. Chen, W. Zhang, S. Liufu, and X. Chen, Enhanced thermoelectric performance of single-walled carbon nanotubes/polyaniline hybrid nanocomposites. ACS Nano 4, 2445–2451, 2010.
9. F. J. DiSalvo, Thermoelectric cooling and power generation. Science 285, 703–706, 1999.
10. https://quillandpad.com/2018/08/10/watches-powered-by-body-heat-did-the-bulova-thermatron-foretell-a-matrix-powerwatch-heat-driven-future/
11. https://ecofriend.com/everything-i-need-to-know-about-thermoelectric-generators.html
12. https://newatlas.com/thermoelectric-orange-power-wellies-generate-electricity/15346/
13. https://phys.org/news/2014-04-thermoelectric-glass-fabric-wearable-electronic.html
14. Choong Sun Kim, Hyeong Man Yang, Jinseok Lee, Gyu Soup Lee, Hyeongdo Choi, Yong Jun Kim, Se Hwan Lim, Seong Hwan Cho, and Byung Jin Cho, Self-Powered Wearable Electrocardiography Using a Wearable Thermoelectric Power Generator, ACS Energy Lett. 3, 501−507, 2018
15. D. M. Rowe, Thermoelecrics handbook: macro to nano, edited by D. M. Rowe (Taylor and Francis, Boca Raton, 2006.
16. A.F. Ioffe, Physics of Semiconductors, Infosearch Lid., London, 1960.
17. Z. Dughaish, "Lead Telluride as a Thermoelectric Material for Thermoelectric Power

Generation," Physica B, 322, 205-223, 2002.
18. L.D. Hicks and M.S. Dresselhaus, “Thermoelectric figure of merit of a one-dimensional conductor,” Phys. Rev. B, 47, 16631– 16634, 1993.
19. D. Li, Y. Wu, P. Kim, L. Shi, P. Yang, and A. Majumdar, “Thermal conductivity of individual silicon nanowires,” Appl. Phys. Lett., 83, 14, 2934–2936, 2003.
20. N. Neophytou and H. Kosina, “Effects of confinement and orientation on the thermoelectric power factor of silicon nanowire,” Phys. Rev. B, 83, 24, 245305-1–16, 2011.
21. V. Pandiyarasan, S. Sathiyamoorthy, F. Khan, A. Ghosh, M. Abhijit, Y. Hayakawa, and H. Ikeda, “Incorporation of ZnO and their composite nanostructured material into a cotton fabric platform for wearable device applications,” Carbohydr. Ploym.,157, 1801–1808, 2017.
22. V. Pandiyarasan, S. Sathiyamoorthy, J. Archana, M. Navaneethan, M. Abhijit, Y. Hayakawa, and H. Ikeda, “Fabrication of hierarchical ZnO nanostructures on cotton fabric for wearable device applications,” Appl. Surf. Sci., 418, 352–361, 2017.
23. P.H.M. Bottger, E. Flage-Larsen, O.B. Karlsen, and T.G. Finstad, “High temperature Seebeck coefficient and resistance measurement system for thermoelectric materials in the thin disk geometry,” Rev. Sci. Instrum., 83, 2, 025101-1–6, 2012.
24. S.J. Kim, J.H. We, G.S. Kim, and B.J. Cho, “Simultaneous measurement of the Seebeck coefficient and thermal conductivity in the cross-sectional direction of thermoelectric thick film,” J. Appl. Phys., 112, 10, 104511-1–5, 2012.
25. Q. Liu, D. Hu, H.Wang, M. Stanford, H.Wang, and B. Hu, “Surface polarization enhanced Seebeck effects in vertical direction multilayer metal-polymer-metal thin film devices,” Phys. Chem. Phys., 16, 40, 22201–22206, 2014.
26. D. Robson, F.Y.I. Assabghy, and D.J.E. Ingram, “Some electronic properties of polycrylonitrile-based carbon fibers,” J. Phys. D: Appl. Phys., 5, 1, 169–179, 1972.
27. H.Y. Cao, W. Yao, and J.J. Qin, “Seebeck effect in graphite carbon fiber cement-based composite,” Adv. Mat. Res., 177, 566–569, 2011.
28. E.J.X. Pang, A. Chan, and S.J. Pickering, “Thermoelectrical properties of intercalated recycled carbon fiber composite,” Composites: Part A, 42, 10, 1406–1411, 2011.
29. E.J.X. Pang, S.J. Pickering, A. Chan, K.H. Wong, and P.L. Lau, “N type thermoelectric recycled carbon fiber sheet with electrochemically deposited Bi2Te3,” J. Solid State Chem., 93, 147–153, 2012.
30. Jinping Liu, Yuanyuan Li, and Xintang Huang, ZnO Nanoneedle Arrays Directly Grown on Bulk Nickel Substrate for Li Ion Battery Electrodes with Improved Performance, INEC, 1-5, 2008.
31. M. Aziz Choudhary, Zahoor Ahmad, Aysha Hassan, Y. Khan & Muhammad Aslem Synthesis and Characterization of ZnO/CuO nanocompsites on Porous 3D Ni Substrate and its Photo-electric Behavior, Synthesis and Reactivity in Inorganic, Metal-Organic, and

Nano-Metal Chemistry, 1-5, 2016.

32. H. K. Kim, T. Nakayama, J. Shimizu and K. Kimura, Effects of Metal Doping on Thermoelectric Properties of Arc-Melted and Hot-Pressed β-Rhombohedral Boron Materials Transactions, 49, 3, 593 to 599, 2008.
33. Mustafa Abdallh, Emaad Bakir, Emad Yousif, Study the electrical conductivity of crosslinked polyester doped with different metal salts, Journal of Saudi Chemical Society 18, 387–391, 2014.
34. Yong-zhenWang, YanWang, HanFei, Xiao-lan Cai, The effect of heat treatment on the electrical conductivity of highly conducting graphene films, CARBON, 51, 436, 2013.
35. https://www.alibaba.com/product-detail/emi-shielding-fabric-electromagnetic-wave-insulation_60550895461.html
36. Priyanka R. Jagadish, Lau Phei Li, Andy Chan, and Mohammad Khalid, Effect of Annealing on Virgin and Recycled Carbon Fiber Electrochemically Deposited with N-type Bismuth Telluride and Bismuth Sulfide, Materials and Manufacturing process, 0, 1-9, 2016.

Chapter 2: Fabrication Methods and Characterization Techniques

2.1. Fabrication methods

2.1.1. Scouring process

Scouring is a process of removing the natural impurities such as oil, wax, fat, etc and other added/external/adventitious impurities/contamination such as dirt, dust, etc from the fabric is called scouring. It is usually done by strong sodium hydroxide (NaOH). Removal of impurities from the fabric makes it more hydrophilic and it becomes easy to grow nanostructures over the fabric. Scouring process sounds very similar to the process named as souring, which carries out to remove alkali part from the fabric with the help of dilute acid [1].

2.1.2. Sol-gel synthesis process

This method of synthesis is one of the easiest and is a well-established synthesis approach to prepare mixed oxide composites and metal oxide nanoparticles (NPs). Using this method, it is possible to control texture and surface properties of the material. The sol-gel method consists of few steps such as hydrolysis, condensation and drying process. Under these consecutive steps, first, hydrolysis is to be carried out to produce metal hydroxide solution using corresponding precursors, followed by sudden condensation which gives the three-dimensional gels. Finally, the obtained gel should be converted to Xerogel or Aerogel by drying process depending on the mode of drying. Depending on solvent utilize sol-gel process can be classified into two types, aqueous sol-gel and nonaqueous sol-gel method. The term aqueous sol-gel should be used when water is used as a reaction medium and if the organic solvent is used as reaction medium, the process is termed as nonaqueous sol-gel. Nature of solvent and metal precursors plays an important role in the preparation of metal oxides NPs in sol-gel synthesis [2]. The sol-gel process is capable of forming membranes [3], chemical sensors [4], optical gain media [5], [6], electrochemical devices [7], photochromic and non-linear applications [8], and nanomaterials [9]. The sol-gel method has lot of advantages over other synthetic procedures, some of them are listed as below [10]:

- The sol-gel can produce a product of high purity and homogeneity.
- It is possible to conduct sol-gel processes low temperatures.
- It is possible to control particle size, size and stoichiometry of multiphase systems using sol-gel process,
- Thin-film fabrication can also be possible using this procedure.
- Various inorganic and organic hybrid materials can also be possible using this process.
- Microstructure during sintering (densification process) can be easily monitored.

2.1.3. Microwave process

Since 2000, Microwave synthesis has been employed for the synthesis of nanostructured materials as it combines the advantage of rapid and homogenous heating of precursor materials. In this process, electromagnetic waves penetrate into the material and transfer their energy volumetrically, which makes it possible to homogeneously heat the reaction solution. Which results in the formation of crystallites that have a narrow size distribution due to the uniform nucleation and rapid crystal growth[11]. Because of the generation of friction and collision of molecules electric fields and magnetic fields of microwave, this process is capable of heating the precursors in a very short time, which is an advantage of this process over other conventional methods [12].

2.1.4. Co- precipitation method

In this process, several stages occur simultaneously, such as nucleation, growth, coarsening, and/or agglomeration.

Following are the characteristic properties of Coprecipitation reactions

• Insoluble species are generally formed under conditions of high supersaturation.

• Followed by Nucleation, which is a crucial step, that results in a large number of small particles

•Ostwald ripening and aggregation, dramatically affect the size, morphology and some secondary processes that occur.

This method has the advantages of producing materials of high purity and crystallinity. It's a rapid and straightforward technique that has various possibilities to modify the particle surface state and overall homogeneity.

2.1.5. Chemical bath deposition (CBD) method

As compared to the commercial methods available, such as thermal evaporation, sputtering and other chemical methods, CBD method has attracted a lot of attention by the young researchers due to its enormous qualities such as replicability, adherent, uniform coatings, large area scaling, simplicity, convenience, and commercial production [13]. To prepare thin films using CBD, a few pieces of equipment like a hot plate and stirrer are sufficient. Better controlled particle's shape and size, particle composition and degree of particle aggregation is possible using this economic approach to prepare the nanocrystalline materials. It is straightforward to control the parameters of CBD to alter the properties of thin films. The preparative parameters of the CBD can be easily controlled to alter the properties of thin films [14].

2.1.6. Sonochemical method

Sonicated processes are accomplished by creating acoustic cavitation in liquids, which creates high pressure and temperature in a microscopic region, the main advantage of sonochemistry when compared to the many other methods used for the synthesis of nanomaterials.
Although there are numerous properties that are unique to the use of ultrasonic waves for the fabrication of nanomaterials in comparison to other methods but the main advantage of sonochemistry when compared to other methods are outlined in four different points [15]:

- Preparation of amorphous products
- Doping of nanomaterials into mesoporous materials.
- Nanoparticles' deposition on ceramic and polymeric surfaces
- Proteinaceous micro - and nanospheres formation

2.1.7. Hydrothermal synthesis

Hydrothermal growth method is a method of synthesizing chemical substance at high temperature and pressure in a sealed and heated solution via chemical reactions. The term 'hydrothermal' coined from earth sciences in the nineteenth century, due to high temperatures and pressures. In fact, some precious crystals such as quartz crystals are formed inside our earth itself, as it works as a huge hydrothermal vessel. In this process of synthesis, generally steel pressure vessel is used for the growth of crystal. At elevated temperatures and pressure, water acts as both, a catalyst and a component of solid phases during the reaction synthesis. Relatively mild operating conditions (reaction temperatures < 300 °C), a one-step synthesis procedure, environmental friendliness, and control over size and shape of nanoparticles, make it different from other synthesis procedures. Moreover, in terms of instrumentation, energy and material precursors this process is relatively inexpensive, compared with other solution synthesis methods [16] - [17].

2.1.8. Solvothermal synthesis

This method of synthesis is very similar to the hydrothermal method, except it uses organic solvents instead of water as a solvent in the synthesis procedure. Furthermore, when alcohols and glycerol are used as the reaction media, the reactions are termed as alcohothermal and glycothermal, respectively. This process takes advantage of both, the sol-gel process as well as the hydrothermal process. It deals with two-step process for the crystallization process, where nucleation of crystals formation by sol-gel process is followed by hydrothermal synthesis. By the precise control over pH, temperature, concentration of precursors, and additives or surfactants the size and morphology of formed products is easily controlled [18].

2.2. Sample characterization techniques

2.2.1. Scanning electron microscope (SEM)

A scanning electron microscope is a type of electron microscope that scans a focused electron beam over a surface to create an image of the sample. Electrons after interacting with atoms in the surface of the sample, produce different signals that can be used to obtain the information about surface topography and composition.

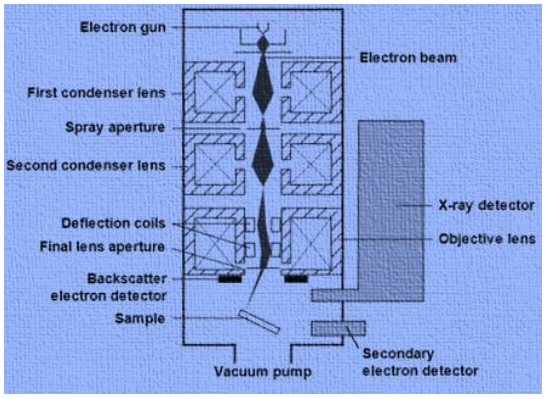

Figure 1. Principle of SEM [20]

Working of SEM: The electron beam is thermionically emitted by using an electron gun consisting of a tungsten filament cathode at the top of the column. This electron beam accelerates downwards and hits the surface of the sample after passing through a series of lenses and apertures that make it focused beam. In the chamber area, a sample is mounted on a stage. Both chamber area and column are in an evacuated state using pumps, unless the microscope is designed to operate in low vacuums. Scan coils are situated above the objective lens to control the position of electron beam on the sample. These coils allow the beam to be scanned over the surface of the sample. The beam of electrons is scanned in a raster scan pattern and the image is formed by the combination of beam's position and intensity of the detected signal. Secondary electrons emitted by atoms excited by electron beam are detected by the appropriate detector. The complete working is shown in Fig. 1 [19],[20]. In this thesis, the SEM images are recorded by JEOL JSM 7001F as shown in Fig. 2

Figure 2. Scanning electron microscope (JEOL JSM 7001F)

2.2.2. Energy-dispersive X-ray spectroscopy

Energy-dispersive X-ray spectroscopy (EDS, EDX, EDXS or XEDS), also known as energy dispersive X-ray analysis (EDXA), is one of the powerful technique used for the chemical characterization and elemental analysis of a sample. It deals with the interaction of a source of X-rays with a sample. The main principle of EDXA is that each element has a unique atomic structure which gives a specific set of peaks on its electromagnetic emission spectrum. Its characterization capabilities are due in large part to the fundamental principle that each element has a unique atomic structure allowing a unique set of peaks on its electromagnetic emission spectrum [21].

A highly focused beam of charged particles such as electron or photons or beam of X-ray is allowed to fall on the surface of the sample under investigation to study the characteristic X-ray from the specimen. As a matter of fact, an atom has all its electrons in the ground state (unexcited state) in its discrete energy levels that are bound to nucleus. When a highly focused beam of charged particles falls over the surface of the sample, it may excite an electron from the inner shell of the atom, resulting in ejection of electron from its place leaving a hole behind it. An electron from the higher energy level try to fill this hole, and the energy difference between the higher energy level and the lower energy level releases in the form of X-rays. These released X-rays are detected by the energy-dispersive spectrometer. As the released X-rays show the characteristics of the difference in energy levels, EDX determines the elemental composition of the material under investigation [22].

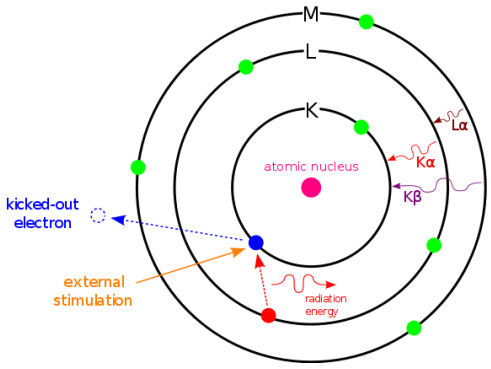

Figure 3: Principle of EDXA

2.2.3. X-ray diffraction (XRD)

X-ray diffraction method is known for the identification and determination of various crystalline forms (phases) present in the sample. It is one of the powerful technique to determine phases of the compound present in the powder or solid samples. X-ray diffraction occurs when electromagnetic waves (x-rays) fall on the regular array of atoms inside the crystal as shown in Fig. 4. X-rays are used to produce diffraction as they have the same wavelength λ (few angstroms), equal to the interlayer spacing between the planes of the crystal. When waves of x-rays strike the atoms' electron,

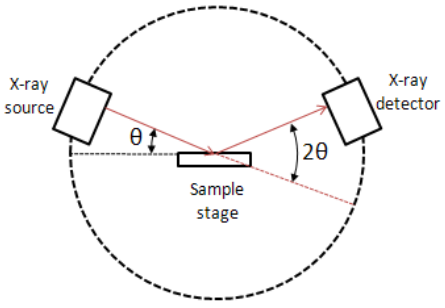

Figure 4: Principle of XRD [23]

there is a production of secondary waves by the produced by electron. This phenomenon is called elastic scattering. These scattered electrons produce a spherical wave. According to Bragg's law, waves in most of the directions cancel each other, destructive interference, however in few directions they add constructively.

$$n\lambda=2d\sin\theta, \quad (1)$$

where n is an integer, 0,1, 2,…, λ is the wavelength of beam, d is the inter-planer spacing, θ is incident angle [23],[24]. In this report, XRD data is recorded using Rigaku X-ray diffractometer (RINT-2200) in the step scanning mode θ - 2θ with Cu kα radiation source (λ) and step width of 0.02°.

Figure 5: Rikagu X-ray diffractometer

2.3. Seebeck coefficient measurement systems

For the development of new thermoelectric material, the measurement of Seebeck coefficient is of fundamental importance. It describes the ability of a material to create voltage under an applied temperature gradient. Integral and differential methods are the two conventional methods through which this parameter can be measured. This method is the easiest way to measure Seebeck coefficient. This method relies on the measurement of voltage generated by a reference wire and a thermocouple consisting of sample material wire. The main drawback of this method is to make the sample in the form of long wire, hence, it is not used in many cases However, the differential method is capable of measuring different varieties of samples and many setups have been reported with each apparatus designed for a particular sample shape [25],[26]. In the present thesis we have used differential method for the evaluation of Seebeck coefficient.

2.3.1. Vertical measurement system

Figure 6 shows a schematic diagram of a developed measurement system for Seebeck coefficient evaluation in the thickness direction of the sample. This has two T-type thermocouples (TCs) which are buried into Cu electrodes. One of the Cu electrodes with an area of 2 × 2 cm^2 is attached to a resistive heater and is set under the sample as a sample holder. The other with an area of 1 × 1 cm^2 is attached to a heat sink and is put on the sample. By flowing appropriate current to the heater, a temperature gradient can be applied to the sample along the vertical direction. In electrically characterizing the flexible materials, it is important to remove the influence of contact resistance at the electrode/sample interface. Therefore, in order to confirm and control the pressure between the electrode and the soft sample during the measurement, the above-mentioned equipment is constructed on a weighing machine, and some weights can be put on the heat sink, as drawn in Fig. 6. The weight of the heat sink was approximately 16 g. By using this system, stable and reproducible measurement can be performed in the same condition every time. The whole piece of equipment is positioned in a shield box to avoid the environmental influences. The heater current was supplied from a DC power supply (MATSUSADA PK160-2.5). The temperatures at the top (T_L) and bottom (T_H) of sample were measured by a digital multimeter (Keithley 2700/7700), and the thermoelectromotive force (TEMF) of the sample was measured by a nanovoltmeter (Keithley 2182A) through the Cu wires in the T-type TCs. The power supply and voltmeters were automatically controlled by a computer. After putting a sample between the Cu electrodes, the temperature gradient was applied along the sample in the thickness direction by heating. Time evolution of temperatures TL and TH were measured simultaneously with the TEMF. Then, the Seebeck coefficient was evaluated from the gradient of the linear relationship between the TEMF and the temperature difference, $\Delta T = T_H - T_L$.

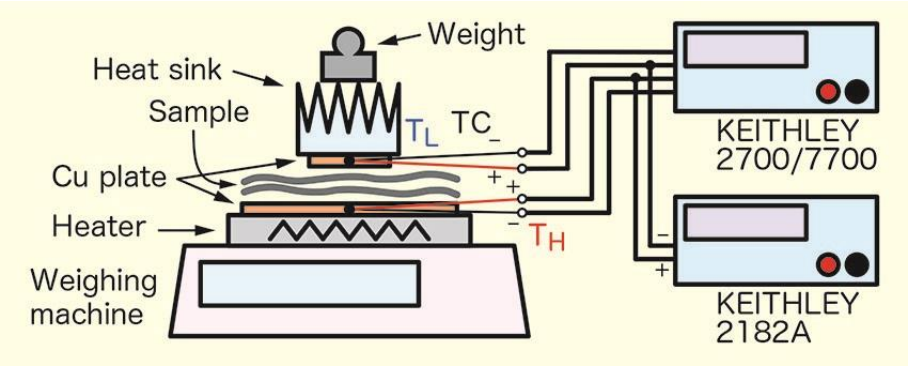

Figure 6: Schematic diagram of the developed Seebeck coefficient measurement system

2.3.1.1. Calibration and Precision

In general, the Seebeck coefficient is a relative value, that is, there is a criterion. Hence, the TEMF (ΔV) is expressed by [27], [28]

$$\Delta V = \int_{T_L}^{T_H} [S_X - S_{cr}]dT$$

where T is the temperature, Sx and Scr are the Seebeck coefficient of the sample X and the criterion material, respectively. T_H and T_L are the temperature at the hot and cold junctions, respectively. The criterion material is Cu in our equipment because Cu wires in the T-type TC are used for measuring the TEMF. For calibration of our system, we measured the Seebeck coefficient of a 2-mm-thick Cu plate (purity: 99.9%). According to Eq. (2), the TEMF obtained in measuring the Cu plate is ideally ΔV = 0 V [29]. However, finite TEMF values were measured under temperature gradient and the evaluated Seebeck coefficient was $S_{Cu} = -0.6$ μV/K. We performed the measurement 7 times and the obtained S_{Cu} values were barely scattered with a standard deviation of 0.1 μV/K, which indicates the good reproducibility. In addition, this fact suggests that our system has a parasitic component $S_{para} = -0.6$ μV/K, which is likely to come from the measurement environment. Therefore, when evaluating the Seebeck coefficient for a material X, S_X, by using the developed system, the true value of the material, S_X^*, should be calibrated by

$$S_X^* = S_X - S_{para}\,. \qquad (2)$$

Since the Seebeck coefficient of bulk Pb is well known [30], [31], a 0.5-mm-thick Pb plate (99.9%) was measured with the aim of confirming the precision of the developed system. The calibrated Seebeck coefficient for the Pb plate was $S_X^* = -1.9$ μV/K, with a standard deviation of 0.1 μV/K. The absolute Seebeck coefficient is 1.2 μV/K smaller than the reported value -3.1 μV/K with respect to Cu [32]. Accordingly, it can be concluded that our constructed system is valid for evaluating the Seebeck coefficient in the thickness direction with an error of about 1 μV/K [33].

The formed instrument used for the measurement of Seebeck coefficient is shown in Fig. 7[34].

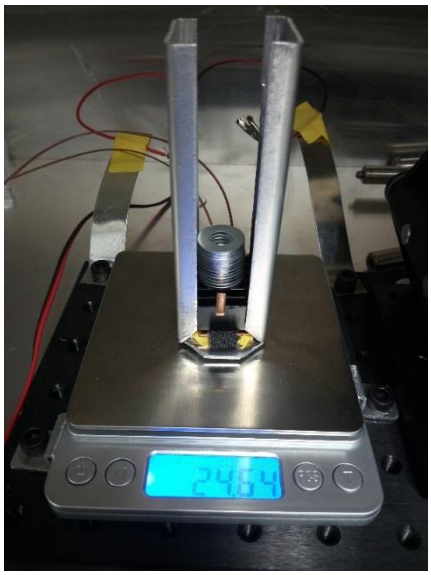

Figure 7: Picture of Seebeck instrument

2.3.2. Horizontal measurement system

This home-made apparatus is utilized to measure the Seebeck coefficient values in the horizontal direction. A spring-loaded sample mounting arrangement provides easy loading/unloading of samples. In addition, the response time of thermocouples is less than 0.1 s to measure the temperature on a wide range of materials, such as pellets, films, fabrics, sheets along with fixed pressure on the samples and even soft surfaces without damage. In the case of horizontal measurement, as shown in Fig. 8, two Peltier devices (TEC1- 12708) over the heat sink are positioned with a small gap between each other. The sample is set over these Peltier devices and T-type thermocouple (3×3 mm^2) electrodes are attached onto the sample surface. In this study, one Peltier device was heated for applying temperature gradient to the sample. Temperatures at the hot and cold region were measured simultaneously with TEMF. The Seebeck coefficient was evaluated from the gradient of the linear relationship between the TEMF and temperature difference.

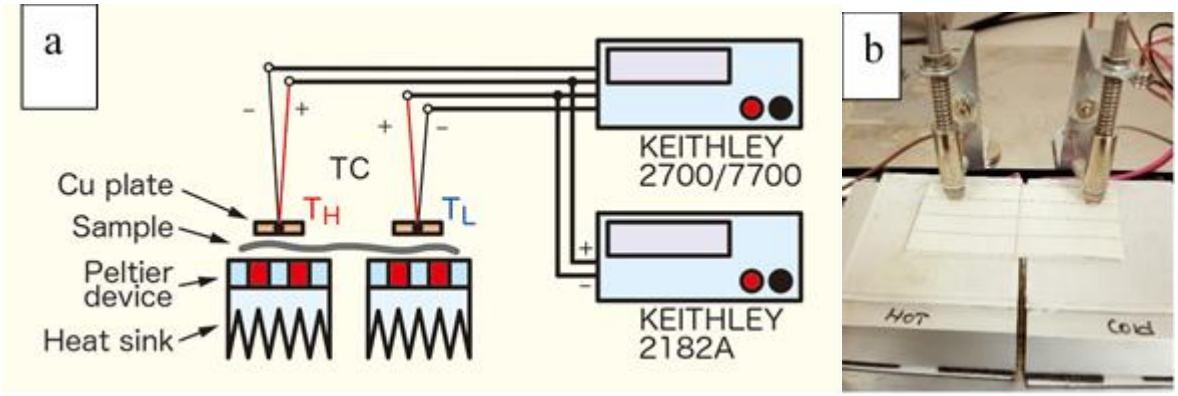

Figure 8: (a) Schematic diagram (b) Picture, of developed Seebeck coefficient measurement system for the horizontal direction

2.4. Electrical measurements

2.4.1. Hall measurement system

These electrical measurement systems are powerful systems capable of measuring not only surface and bulk resistivities of the sample but also carrier concentrations of the sample. These instruments are based on Hall effect given by Edwin Hall in 1879, which says, there will be a production of voltage difference across an electrical conductor, in the perpendicular direction of current in the conductor and perpendicular to the direction of applied magnetic field which

is in transverse direction to current flowing in the conductor[34].

Fig. 9 shows the hall instrument system used in this thesis, for the measurement of electrical resistivity of prepared samples, and to justify the readings of home-made electrical measurement system.

Figure 9: Hall Instrument

2.4.2. Vertical measurement system

Current-Voltage characteristics (the I-V curve) is a graph that gives a relationship between electrical current through the circuit/material and the corresponding voltage across it. The I-V curves give qualitative information about resistance characteristics and power generated/dissipation. However, it is possible to obtain much information about the properties of conducting materials or devices by analyzing the IV dependence both in DC and in AC regimes [1][35]. Resistivities of insulator material such as plastic, paper or rubber can easily be determined using two probe instruments, that is, by applying a voltage to the sample through two electrodes for a specified period of time and measuring the

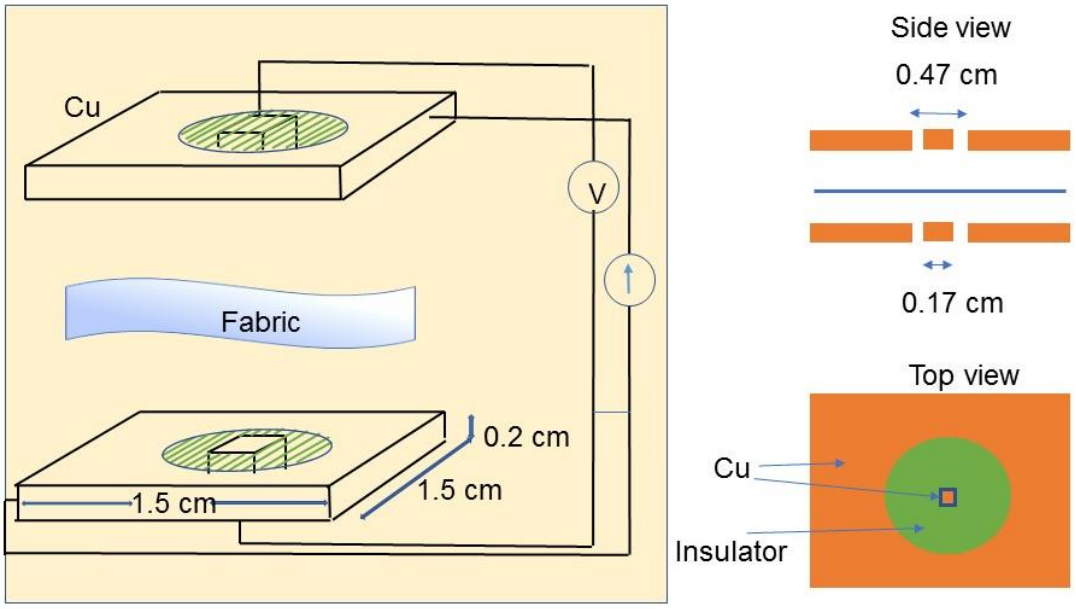

Figure 10: Schematic of electric resistivity measurement system in vertical direction

current by connecting ammeter to the same two points and finally calculating the resistivity through Ohm's law [36]. However, this kind of instrument is not possible for the resistivity measurement of metals or semiconductors because of high contact resistance. The measurement of resistivity of metals or semiconductors should be accurately and precisely measured because of their low resistivity value. Therefore, by keeping this point in mind, we have constructed a system based on the four-probe arrangement as shown in Fig 10. In this system two copper plates of thickness 0. 2 cm and cross-sectional area 1.5 × 1.5 cm2 are taken

as electrodes. A hole of 0.47cm is drilled at the center of the plate and another electrode of size 0.17×0.17 cm^2 is placed at the center. The gap between the center electrode and the outer electrode is filled with an insulating material (Araldite) to keep them insulating from each other, as shown in Fig. 11. The outer electrode is attached to the current source and the inner electrode is attached to the multimeter (Keithley 2700/7700). The sample is placed between two copper sheets and a fixed amount of weight is put over the non-conducting material. Current is increased gradually at a step of 0.05A and the forming voltage is measured. The resistivity of the sample is calculated by the formula

$$R = \frac{\rho . L}{A} , \qquad (3)$$

Where R is the resistance, L is the distance between voltage leads (thickness of sample), ρ is the resistivity of sample under investigation. The effective area to flow the current can be calculated as,

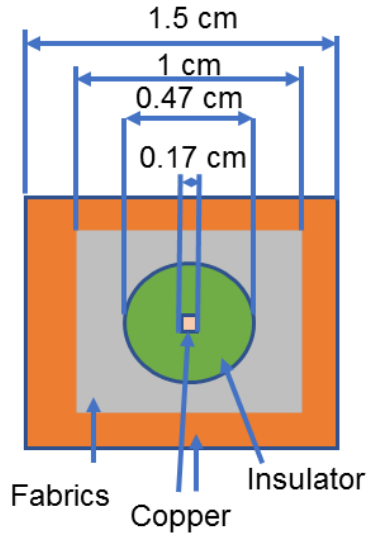

Figure 11: Dimensions of electrode

Diameter (insulating part), d = 0.47 cm,

Radius (insulating part), r = 0.235 cm,

Area of circle, a = πr^2= 3.14 x $(0.235)^2$ = 0.173 cm^2,

Effective area, A = Area of sample = 1 cm^2 - 0.173 cm^2= 0.827cm^2

References

1. Pandiyarasan Veluswamy, Suhasini Sathiyamoorthy, Hiroya Ikeda, Manikandan Elayaperumal and Malik Maaza, Recent Progress in Nanostructured Zinc Oxide Grown on Fabric for Wearable Thermoelectric Power Generator with UV Shielding, chapter 7, doi: 10.5772/intechopen.76672
2. Bolla G. Rao, Deboshree Mukherjee and Benjaram M. Reddy, novel approaches for preparation of nanoparticles, doi: 10.1016/B978-0-323-46142-9.00001-3
3. Yu Y, Pan W, Guo X, Gao L, Gu Y, Liu Y. A poly (arylene ether sulfone) hybrid membrane using titanium dioxide nanoparticles as the filler: Preparation, characterization and gas separation study. High Performance Polymers., 29(1) 26–35, 2017, doi:10.1177/095400 8315626990
4. M. Barczak, C. McDonagh, D. Wencel, Micro and nanostructured sol-gel-based materials for optical chemical sensing (2005-2015). Microchimica Acta., 183: 2085-2109., 2016, doi:10.1007/s00604-016-1863-y
5. Ong X, Zhi M, Gupta S, Chan Y. Wet-chemically synthesized colloidal semiconductor nanostructures as optical gain media. Chemphyschem: A European Journal of Chemical Physics and Physical Chemistry., 17, 582–597, 2016, doi:10.1002/cphc.201500975
6. Mikosch A, Ciftci S, Kuehne AJ. Colloidal crystal lasers from monodisperse conjugated polymer particles via bottom-up coassembly in a sol-gel matrix. ACS Nano,10, 10195-10201, 2016, doi:10.1021/acsnano.6b05538
7. Lee S-W, Kim H, Kim M-S, Youn H-C, Kang K, Cho B-W, Roh KC, Kim KB. Improved electrochemical performance of LiNi0.6Co0.2Mn0.2O2 cathode material synthesized by citric acid assisted sol-gel method for lithium ion batteries. Journal of Power Sources,315, 261-268, 2016
8. Adachi K, Tokushige M, Omata K, Yamazaki S, Iwadate Y. Kinetics of coloration in photochromic tungsten (VI) oxide/silicon oxycarbide/silica hybrid xerogel: Insight into cation self-diffusion mechanisms. ACS Applied Materials & Interfaces.,8, 14019-14028, 2016, doi:10.1021/acsami.6b04115
9. Mohana Priya S, Geetha A, Ramamurthi K. Structural, morphological and optical properties of tin oxide nanoparticles synthesized by sol-gel method adding hydrochloric acid. Journal of Sol-Gel Science and Technology.,78, 365-372., 2016, doi:10.1007/s10971-016-3966-7
10. Asad Mahmood and Abdul Naeem, Sol-Gel-Derived Doped ZnO Thin Films: Processing, Properties, and Applications, Recent Applications in Sol-Gel Synthesis, chapter 9, 169-193, doi-http://dx.doi.org/10.5772/67857

11. Damian C. Onwudiwe, Microwave-assisted synthesis of PbS nanostructures, Heliyon 5, 1-7, e01413, 2019.
12. T. Ding, J.-R. Zhang, S. Long, J.-J. Zhu, Synthesis of HgS and PbS nanocrystals in a polyol solvent by microwave heating, Microelectron. Eng. 66, 46e52, 2003.
13. D. P. Dubal, R. Holze, P. Gomez-Romero, Sci. Rep., 4, 2014, 7349.
14. R. S. Mane and C. D. Lokhande, Mater. Chem. Phys., 65, 1, 2000.
15. A. Gedanken, I. Perelshtein, Power ultrasound for the production of nanomaterials, Power Ultrasonics, chapter 18, 543-576, 2015.
16. A. D. Li, Nanjing University, P. R. China and W. C. Liu, Optical properties of ferroelectric nanocrystal/polymer composites, polymer composites, 4, 108-158, 2010.
17. Dongyuan Zhao and Ying Wan, Introduction to Zeolite Science and Practice Studies in Surface Science and Catalysis, 2007.
18. H.ZhongT.MirkovicG.D.Scholes, Reference Module in Materials Science and Materials Engineering, Nanocrystal Synthesis, 5, 153-201, 2011
19. Stokes, Debbie J., Principles and Practice of Variable Pressure Environmental Scanning Electron Microscopy (VP-ESEM). Chichester: John Wiley & Sons., (2008)
20. https://www.nanoscience.com/techniques/scanning-electron-microscopy/
21. Joseph Goldstein (2003). Scanning Electron Microscopy and X-Ray Microanalysis. Springer. ISBN 978-0-306-47292-3. Retrieved 26 May 2012.
22. Joseph Goldstein (2003). Scanning Electron Microscopy and X-Ray Microanalysis. Springer. ISBN 978-0-306-47292-3. Retrieved 2012.
23. https://chem.libretexts.org/Bookshelves/Analytical_Chemistry/Supplemental_Modules_(Analytical_Chemistry)/Instrumental_Analysis/Diffraction_Scattering_Techniques/Powder_X-ray_Diffraction
24. Von Laue M, "Concerning the detection of x-ray interferences" (PDF). Nobel Lectures, Physics. 1901–1921. Retrieved 2009.
25. Rowe, D. M. Thermoelectrics Handbook: Macro to Nano; CRC, Press, Taylor & Francis Group: Boca Raton, 22, 2-12, 2006
26. Rafiq Mulla and M. K. Rabinal, A Simple and Portable Setup for Thermopower Measurements, ACS Comb. Sci., 18, 177-181, 2016
27. Y. Zhou, D. Yang, L. Li, F. Li, and J.-F. Li, “Fast Seebeck coefficient measurement based on dynamic method,” Rev. Sci. Instrum., 85, 5. pp.054904-1-5, 2014.
28. J. Martin, “Apparatus for the high temperature measurement of the Seebeck coefficient in thermoelectric materials,” Rev. Sci. Instrum., 83, 6, 065101-1-9, 2012.
29. S.O. Kasap, Thermoelectric Effects in Metals: Thermocouples, University of Saskatchewan, Canada, 1-11, 2001.

30. J.W. Cristian, J.-P. Jan, W.B. Pearson, and I.M. Templeton, “Thermo-electricity at low temperatures. VI. A redetermination of the absolute scale of thermo-electric power of lead,” Proc. R. Soc. Lond. A, 245, 1241, 213–221, 1958.
31. R.B. Roberts, “The absolute scale of thermoelectricity II,” Philos. Mag. B., 43, 6, 1125–1135, 1981.
32. J. Bass, Electrical Resistivity, Thermoelectrical Power and Optical Properties, Landolt-Bornstein - Group III Condensed Matter, 15b, Springer-Verlag Berlin Heidelberg, 1985.
33. Edwin Hall, "On a New Action of the Magnet on Electric Currents". American Journal of Mathematics. 2 (3): 287–92. doi:10.2307/2369245. JSTOR 2369245. Archived from the original on 2011-07-27. Retrieved 2008-02-28, 1879.
34. Faizan Khan, Veluswamy Pandiyarasan, Shota Sakamoto, Mani Navaneethan, Masaru Shimomura, Kenji Murakami, Yasuhiro Hayakawa And Hiroya Ikeda, Seebeck Coefficient of Flexible Carbon Fabric for Wearable Thermoelectric Device, IEICE Trans. Electron., E101–C, 5, 2018.
35. Enrico Cataldo, Alberto Di Lieto, Francesco Maccarrone and Giampiero Paffuti, Measurements and analysis of current–voltage characteristic of a pn diode for an undergraduate physics laboratory, Physics Education, 2016
36. M.A.Tupta, Electronic Engineering Times Europe, January 2011.

Chapter 3: Fabrication of ZnO and rGO Nanostructures on Nickel Copper Fabric (NCF)

3.1. Introduction to NCF

Thermoelectric materials can be divided into three categories, low temperature, intermediate temperature and high temperature range materials. Low range temperature materials are the alloys based on Bismuth (Bi) in combinations with Antimony (An), Tellurium (Te) or Selenium (Se), and can be used up to 450K. Intermediate range temperature materials are alloys of Lead (Pb) and can be used up to 850K, while the high temperature range materials fabricated from SiGe alloys and can be used up to 1300K [1]. Thermoelectric efficiency in somehow related to figure-of-merit, hence researchers are trying to develop new thermoelectric materials for power generation by improving the Z. ZT of 1.3 is reported for a semiconductor compound named as ß-Zn_4Sb_3 and ZT of 2.6 is reported for single crystal of tin selenide [2], [3]. Besides, the improved figure of merit, attempts should be made in the other direction as well, such as development of eco-friendly, cost effective and high-power factor materials. In this chapter we will focus on conductive nickel copper fabric (NCF), as a flexible substrate. This conductive NCF is expected to increase the conductivity and hence Z. In addition, ZnO nanostructure coating on fabric will increase Seebeck coefficient due to confinement of carriers and phonon [4]-[6]. Several studies are reported on nickel doped ZnO [7]-[10] and copper doped ZnO [11]. Ni doping has the advantage of low cost compared to other materials like Ag doping [12]. However, few researchers studied the thermoelectric properties of ZnO on nickel substrate [13]-[14]. To our knowledge no one reported the thermoelectric properties of NCF, especially in vertical direction.

The fabric used in this thesis was purchased from Beijing, China. NCF contains 23% of copper, 27% of nickel and 50% of polyester. The thickness of NCF is 0.27 mm, yarn count is 80D, weight - 100gm/sqm, shielding efficiency is greater than 99.9 %. Fig. 1 shows the bare(original) SEM image of NCF at its zoom image.

3.2. Experimental procedure

3.2.1. Synthesis of ZnO nanostructures

In this study, a two-step hydrothermal method is used to synthesize the nanostructure of ZnO over the fabric. Formation of the seed layer (first step) is followed by growth step (second step). The morphology of ZnO structures is strongly influenced by the seed layer. The presence of the seed layer reduces the nucleation energy barrier and lattice mismatch effectively. Moreover, a thinner seed layer provides higher surface area for the formation of ZnO rods because of their small crystal size. Seed layers generally provide an optimum nucleation rate or growth of the later process's material in the specific direction. Without the seed layer, we can also grow our nanostructures, but a slower rate is expected, or in a form we would not expect. So, there are

some parameters which we can utilize to improve the growth process. For the optimization of nanostructures, synthesis is carried out at different ratios, temperatures and annealing time, as shown in table 1, and details are given for NC1, as an example. All the chemical used in this process were purchased from Wako Chemicals and used without any further purification.

Table 1: Types of sample and their specifications

Sample	Ratio (ZN:HMT)	Growth time (h)	Annealing temperature (°C)
NCF1	1:2	1	60
NCF2	1:2	1	120
NCF3	3:1	1	60
NCF4	3:1	1	120
NCF5	1:2	5	60
NCF6	1:2	5	120
NCF7	3:1	5	60
NCF8	3:1	5	120

Seed formation process (first step) for NCF1:

In "first step" process, seed layer of ZnO was prepared by mixing the solutions of 0.1 M of Zinc nitrate hexahydrate [$Zn(NO_3)_26H_2O$] in 50 mL of distilled (DI) water and 0.2 M of Hexamethylenetetramine $(CH_2)_6N_4$ in 50 mL of DI water. The solution is stirred at 50°C for 2h after immersing the NCF fabric. Then, the solution containing the fabric was set in an autoclave for 1h at 120°C and finally the sample is washed three times with DI water and then annealed at 60°C for 2 h, as shown in Fig 1.

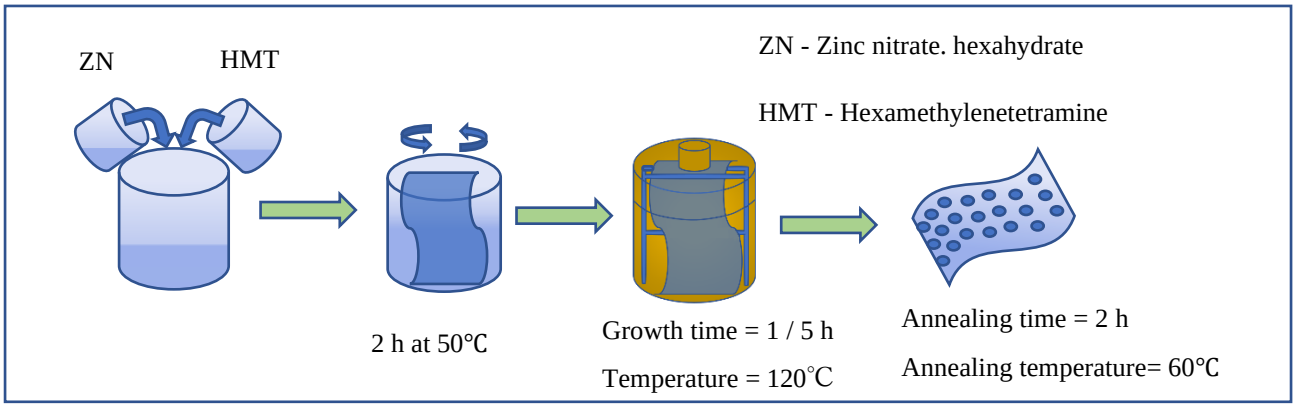

Figure 1: This figure shows the first step process

Nanostructure growth (second step) for NCF1: For the growth of nanostructures on the fabric, as a second step, solutions of molar ratio (1:2) of Zinc nitrate hexahydrate

[$Zn(NO_3)_26H_2O$] and $(CH_2)_6N_4$ is mixed together and the seed layer formed in first step is stirred with the solution for 2 h at 50℃ and growth time set to 5 h and finally the sample is washed three times with DI water and annealed at 60°C for 2 h, as shown in Fig 2.

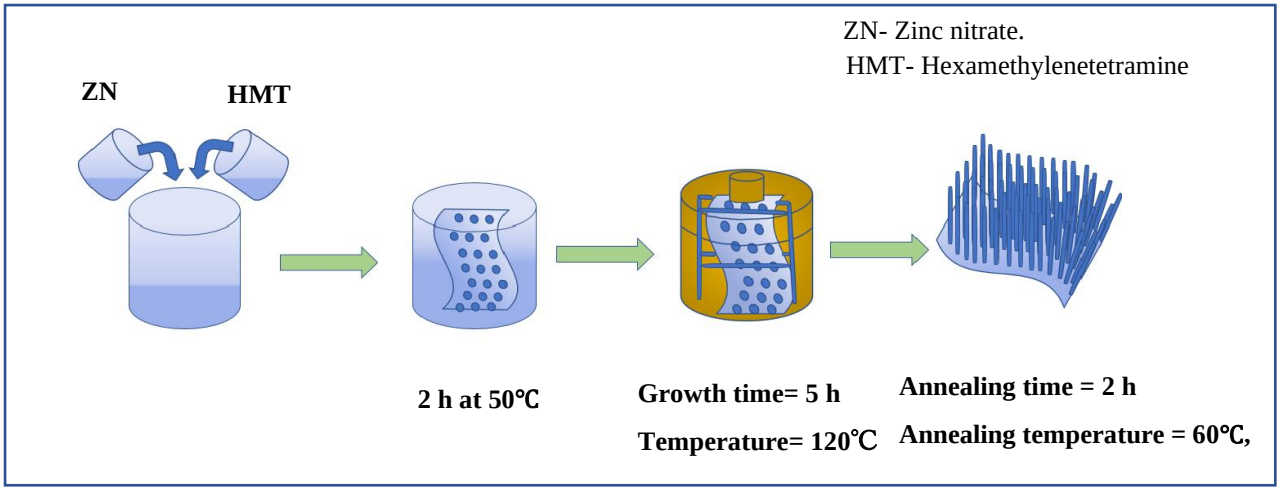

Figure 2: Shows the second step (growth step) followed by the first step

3.3. Result and discussion for ZnO

3.3.1. Scanning electron microscopy (SEM)

Fig 3 shows that SEM images of bare (original) and first step ZnO seed layer over NCF. Fig 3(a), (b), (c) shows the images for the original fabric which illustrate that the fabric is defect-free and there is no impurity over the fabric's fiber. The diameter of the fiber is estimated to be in the range of nano to micrometer. Fig 3(d), (e), (f) illustrate the images of NCF1, showing the best suitable condition, as there are many ZnO rods present along with the seed layer of ZnO all over the surface depicted by the magnified image. Fig 3(g), (h), (i), show the images for NCF2, although the seed layer structure is visible however there are very few or almost nil ZnO rods visible. There also appears to be particles agglomerated which are round in shape. Fig 3(j), (k), (l) shows the images for NCF3, in which the seed layer is almost visible, but no traces of ZnO rods. Finally, Fig 3(m), (n), (o) show the images for NCF4, with few ZnO rods stick to the NCF with agglomerated sheet-like structure at some parts. Similar trends can be seen in 4(a)-(l), in which the surface is not fully covered with ZnO seeds. However, Fig 4(g)-(i) shows good formation of hollow nanorods like structure. This scanning electron microscopy suggests that the best choice for proceeding to the second step is NCF1. Hence, we proceeded for the second step only for the NCF1.

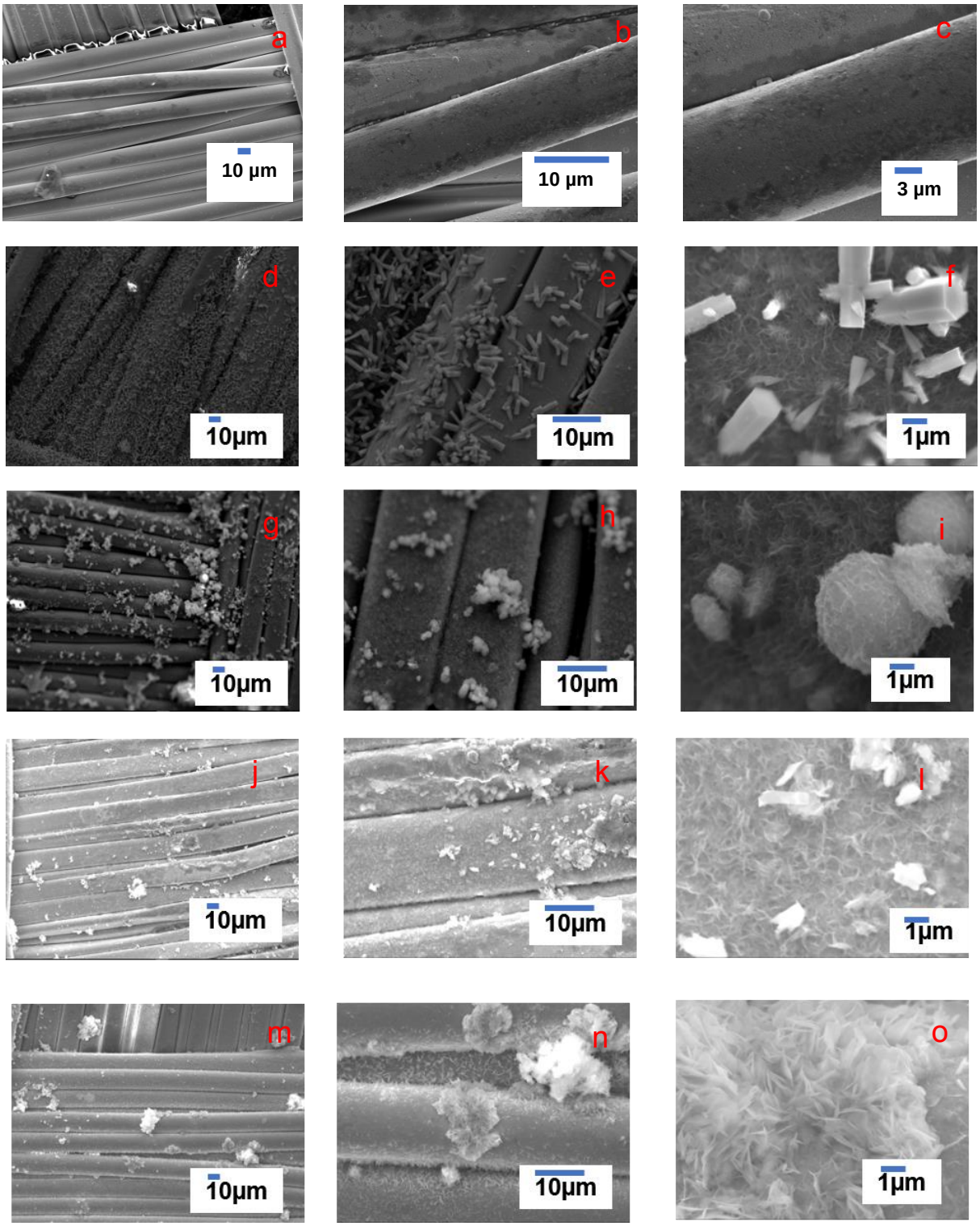

Figure 3: SEM images of NCF(original) to NCF4

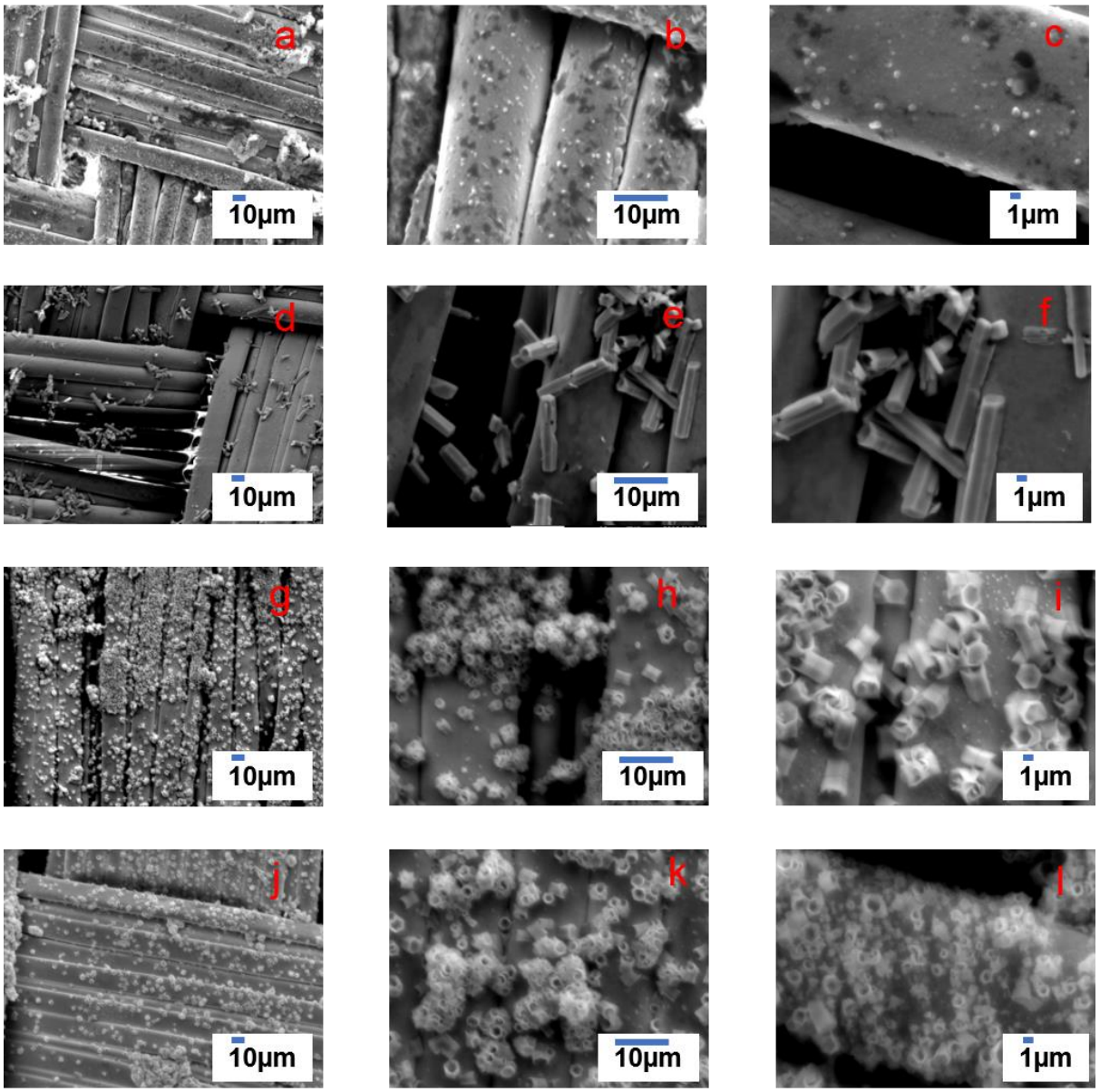

Figure 4: 4(a)-(l) show the SEM images of seed layered samples from NCF5 to NCF8

Fig 5 shows the SEM images for the second step in the process for NCF1 at different magnifications. It can be clearly seen that high dense nanorods have been grown over the surface of NCF. Few rods show the candle-like structure due to the formation of one rod over the another.

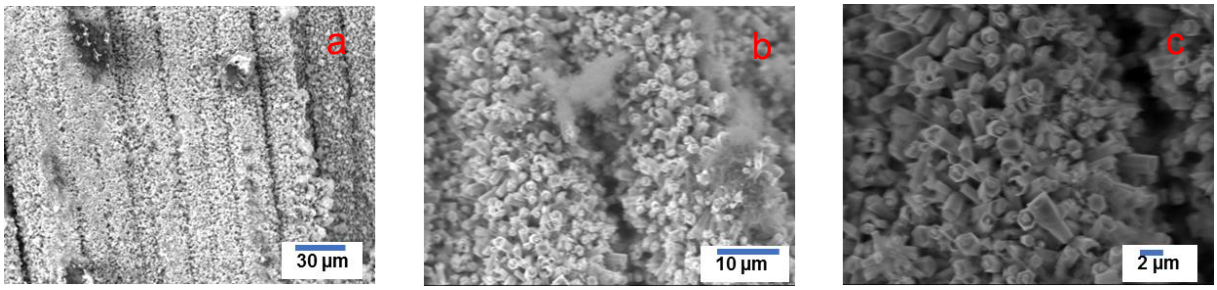

Figure 5: (a), (b), (c) show the SEM images of second step ZnO / NCF at different resolutions.

3.3.2. EDXA mapping

Energy dispersive x-ray mapping is a technique through which it is possible to identify the distribution of chemical over the surface. Fig 6(a)-(e) shows the EDXA mapping for original NCF, in which image (c), (e) clearly show the presence of copper and nickel present in the substrate. Similarly, images from 6(f)-(k) shows the images for first step ZnO / NCF, 6(l)-(r) show for the second step ZnO / NCF. The presence of Zn is clearly visible in 6(k), (r), and the presence of O can be seen in 6(i), (p). As we move from the first step to second step images gets clear because of the presence of more and more ZnO. However, images for carbon, nickel and copper get fainted due to the surface of ZnO over the substrate. The percentage of elements present is shown in table 2. Fig 7 shows that there is no impurity present in the formed nanostructures.

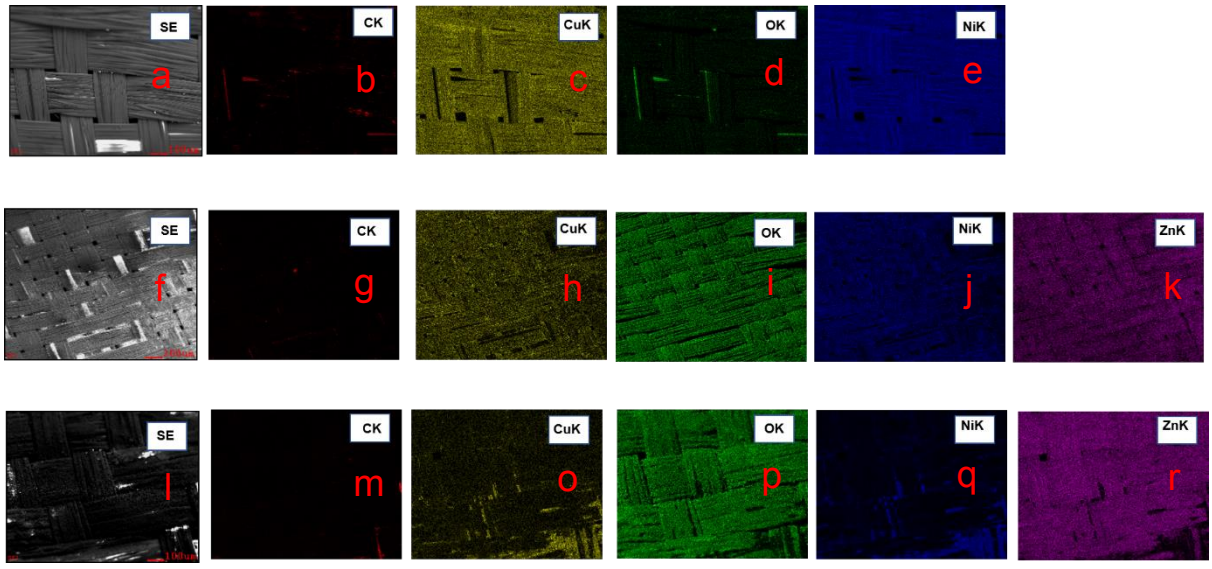

Figure 6: Mapping for original(a)-(e), 1st step ZnO / NCF(f)-(k) and 2nd step ZnO/NCF(l)-(r).

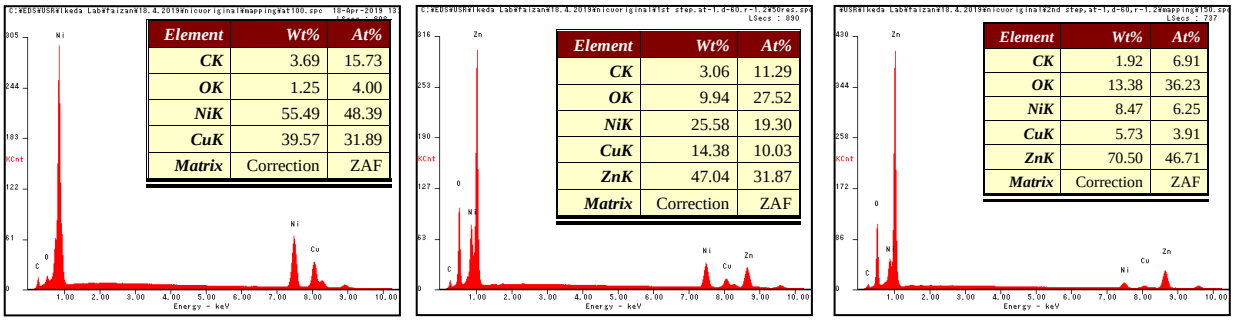

Figure 7: EDX analysis for (a) NCF, (b) 1st step ZnO / NCF, (c) 2nd ZnO / NCF

3.3.3. X-ray diffraction (XRD)

In this study, we have analyzed three different samples original NCF, 1st step ZnO/ NCF and 2nd step ZnO / NCF. Fig 8 represents the XRD data of these samples, that is employed to investigate crystallinity, crystalline phase, and direction of prepared nanorods. XRD pattern of original NCF shows clear peaks of nickel (ni) and copper(cu) at 44.349°, 51.674° and 43.298°, 50.434° (JCPDS card no. 01-089-7128, 00-004-0836) respectively for original NCF, as shown in Fig 8. Presence of seed layer and nanostructured ZnO prominent peaks can be seen in all steps at 31.619°, 34.335°, 36.100°, 47.367°, 56.313°, 62.645° and 68.737° (JCPDS card no. 01-079-0208), however the sharp peaks are visible only in second step, shows the crystallinity of ZnO material. Herein, the ZnO XRD patterns were indexed to the wurtzite structure of ZnO. Considering the ZnO nanorods' directions XRD results are perfectly matched with alignment of nanorods array on the surface of NCF observed in SEM images and EDAX graphs.

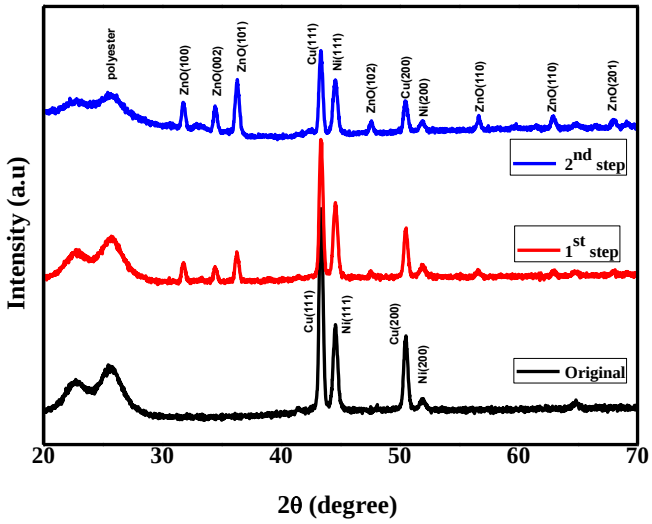

Figure 8: This figure shows the XRD graph for original NCF, 1st step ZnO/ NCF, 2nd step ZnO / NCF

3.3.4. Seebeck Coefficient

Vertical direction measurements of the Seebeck coefficient are made using the apparatus shown in figure 9, already discussed in the instrument section.

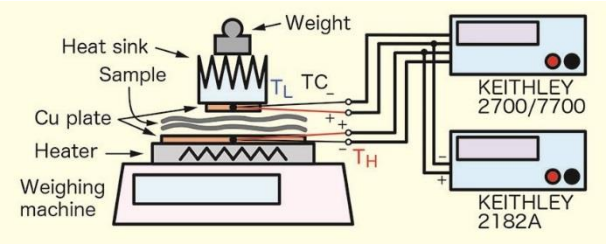

Figure 9: Schematic diagram of developed Seebeck coefficient measurement system.

The bare fabric was characterized by our system for confirming and optimizing the measurement conditions such as the TC-electrode/flexible-material contact. An example of the time evolutions of TEMF, T_L and T_H for the NCF is shown in Fig. 10. It is clearly observed that the TEMF positively increases with an increase in the temperature difference ΔT. Figure 11 shows the relationship between TEMF and temperature difference replotted from Fig. 10. In this figure, "Increase" means the data collected from the range where the temperature difference is increasing, and "Decrease" corresponds to the data under decreasing the temperature difference in Fig. 10. Both "Increase" and "Decrease" data are nearly identical. This fact means that the measured data is reliable even for flexible materials. In addition, both data make a linear relation, indicating that the Seebeck coefficient is nearly constant in the measured temperature range. The Seebeck coefficient S was evaluated from the TEMF ($\Delta V = V_H - V_L$) and the temperature difference ($\Delta T = T_H - T_L$) by $S = -\Delta V / \Delta T$ near room temperature. Therefore, the average Seebeck coefficient of NCF is evaluated from the gradient of the linear graph to be $S_{NCF} \sim -2.7$ μV/K, which is close to that of the same NCF obtained in the horizontal direction, -1.3 μV/K using the apparatus shown in previous chapter. The Seebeck coefficient is negative, indicating that the NCF used is a n-type material and increases with increasing the number of layers as shown in

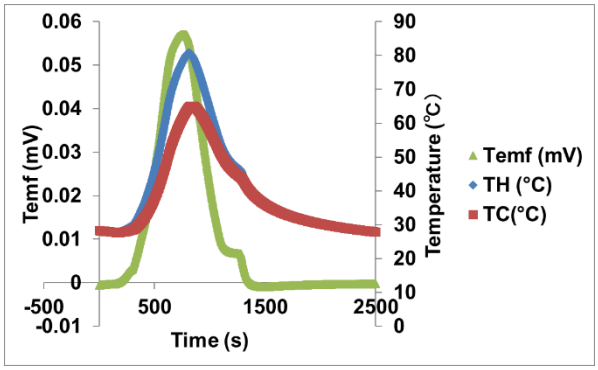

Figure 10. Time evolutions of TEMF and temperatures at hot T_H and cold T_L junctions for single NCF layer.

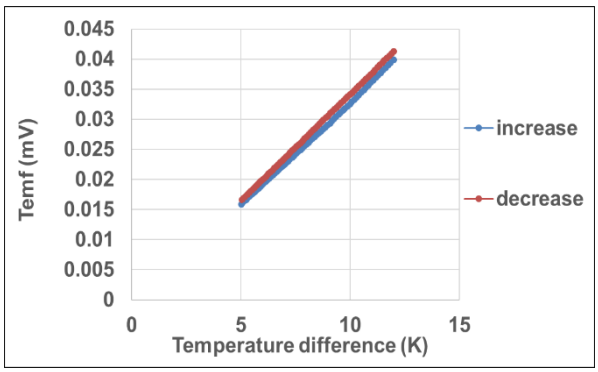

Figure 11: Relationship between TEMF and temperature difference for single NCF layer. "Increase" and "Decrease" correspond to the data collected from the range where the temperature difference is increasing and decreasing, respectively, in Fig. 10.

Fig 12. The vertical and horizontal Seebeck coefficients of these samples are summarized in Table 3, measured using our home-made apparatus. All samples have negative Seebeck coefficients, or an n-type semiconductor behavior. It is found that the Seebeck coefficient negatively increases by fabricating the ZnO on the NCF which may be due to oxygen vacancies. Considering that ZnO is usually an n-type semiconductor, the ZnO nanorod contributes to enhance the Seebeck coefficient.

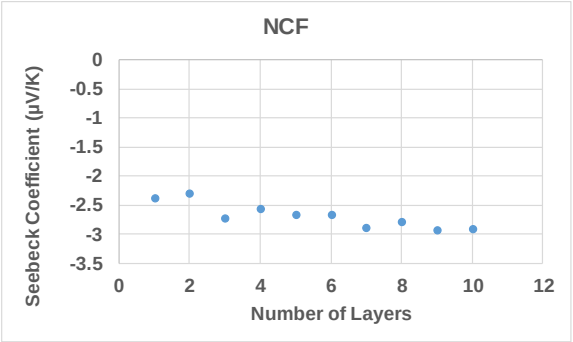

Figure 12: Relationship between Seebeck coefficient and the number of stacked NCF layers in vertical direction

Table 3: This table represents the Seebeck coefficient values of NCF and ZnO / NCF

NCF	S_{Vert} [μV/K]	S_{Horiz} [μV/K]
Original	-2.7	-1.3
1st Step ZnO / NCF	-3.4	-1.5
2nd Step ZnO / NCF	-4.5	-2.7

3.3.5. Laundering process

For checking the adhesiveness of our fabricated ZnO over NCF substrate, we have chosen a very simple and effective process. We have sonicated our fabricated sample 3 times for 5 min each in 50 mL of DI water, then the fabric is stirred in 100mL of DI water for 2 hours, and finally dried the product at 60℃ for 2 hours. During this process, no detergent or soap is used to avoid chemical reaction during the laundering process. The full process is shown in Fig 13.

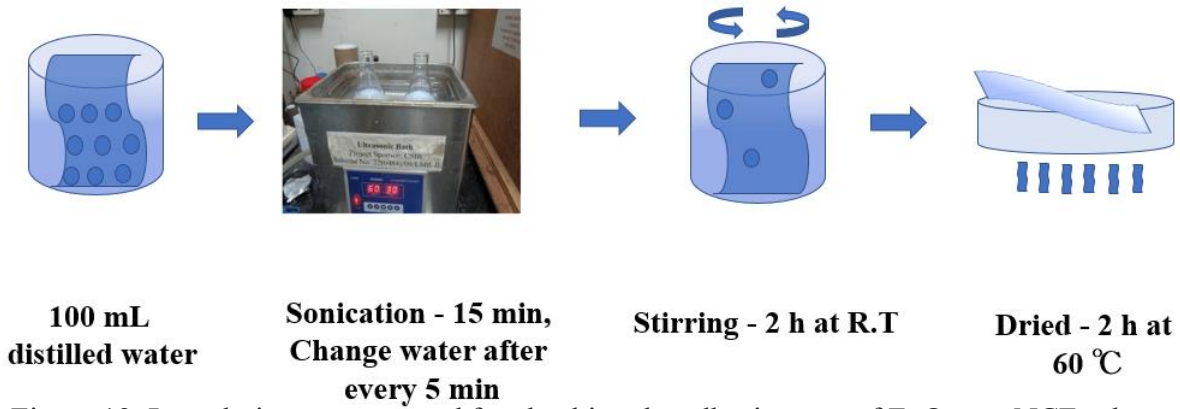

Figure 13: Laundering process used for checking the adhesiveness of ZnO over NCF substrate

Before and after laundering process, weight of 1cm^2 2nd step ZnO / NCF was measured three times and the difference of their averages is found to be 2.82 mg. Hence, we can say that only 2.82 mg of ZnO is removed from the fabric of 1 cm^2. The adhesiveness of ZnO after laundering

process is shown in SEM images of Fig 14. Furthermore, the adhesion is confirmed by XRD and Seebeck coefficient values, as shown in Fig 15. Furthermore, the same peaks of ZnO as observed for 2nd step ZnO before laundering and 2nd step ZnO after laundering can be seen in

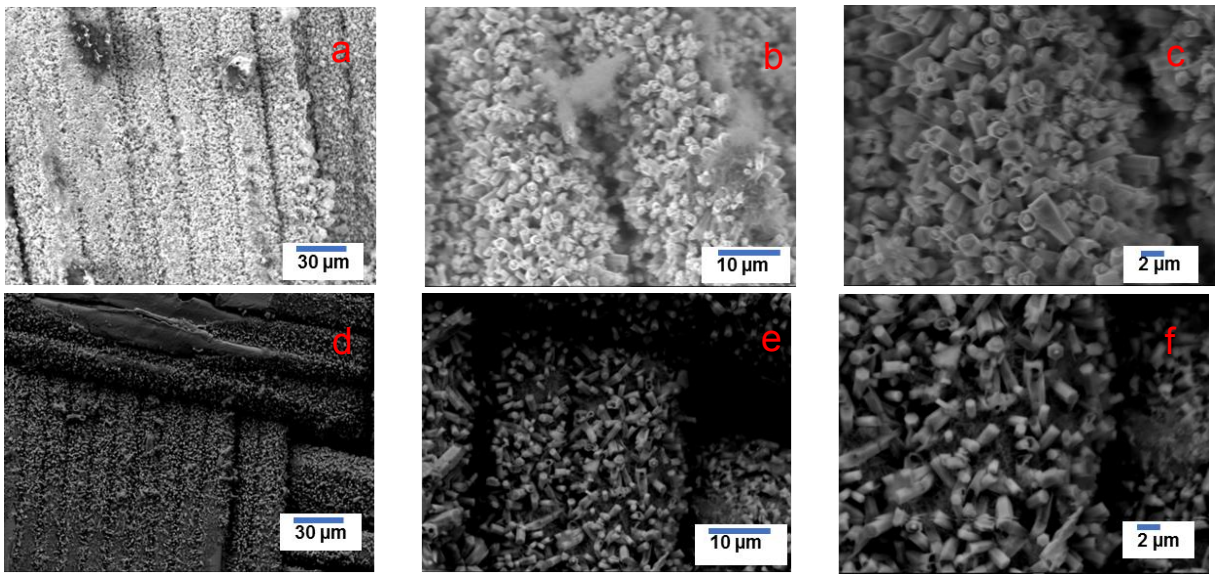

Figure 14: SEM images for (a)-(c) 1st step ZnO / NCF and (d)-(f) 2nd step ZnO / NCF after the laundering process

the XRD pattern of the samples as shown in Fig 15. However, the washed samples showed the decrement in their Seebeck coefficient values, depicted in table 4. The value of 1st step almost returned to its original value. However, 2nd step still shows some higher values, which confirms the adhesion of ZnO over the fabric. The slight increment in the horizontal values after laundering may come from instrument error. The Seebeck values before and after laundering are encapsulated in table 4.

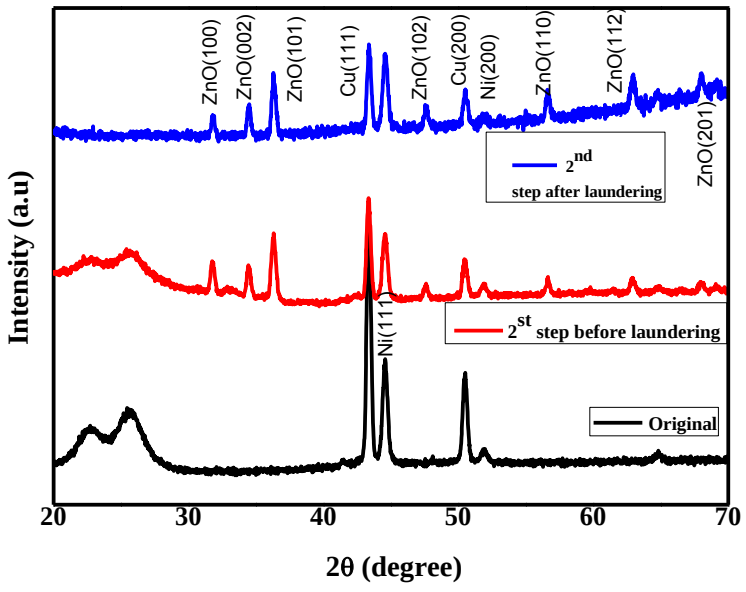

Figure 15. XRD after laundering effect

Table 4: This table represents the Seebeck coefficient values of NCF and ZnO / NCF after laundering process

NCF	S_{Vert} [µV/K]	S_{Horiz} [µV/K]
Original	-2.7	-1.3
2nd step	- 4.5	-2.7
2nd Step after laundering	-3.9	-3.1

3.3.6. Electrical conductivity

To calculate electrical conductivity in the vertical direction, we have measured electrical resistivity by our home-made apparatus. Since, it is difficult to measure the electrical resistivity of metals, because they have very low resistivity (in order of 10^{-8} Ω-m). Therefore, we have compared our values with that of measured with Hall effect instrument. Instrument for the measurement of electrical resistivity in vertical direction is shown in Fig 16, 17, detail of this instrument is already described in the instrumentation chapter. Current (A) is applied at the outer part of the electrode and voltage generated is measured through the inner electrodes. The IV graph for the single layer of NCF is shown in Fig 18. The resistance value of original NCF fabric is found to be around 363 mΩ and the resistivity is calculated to be around 111 mΩ.m.

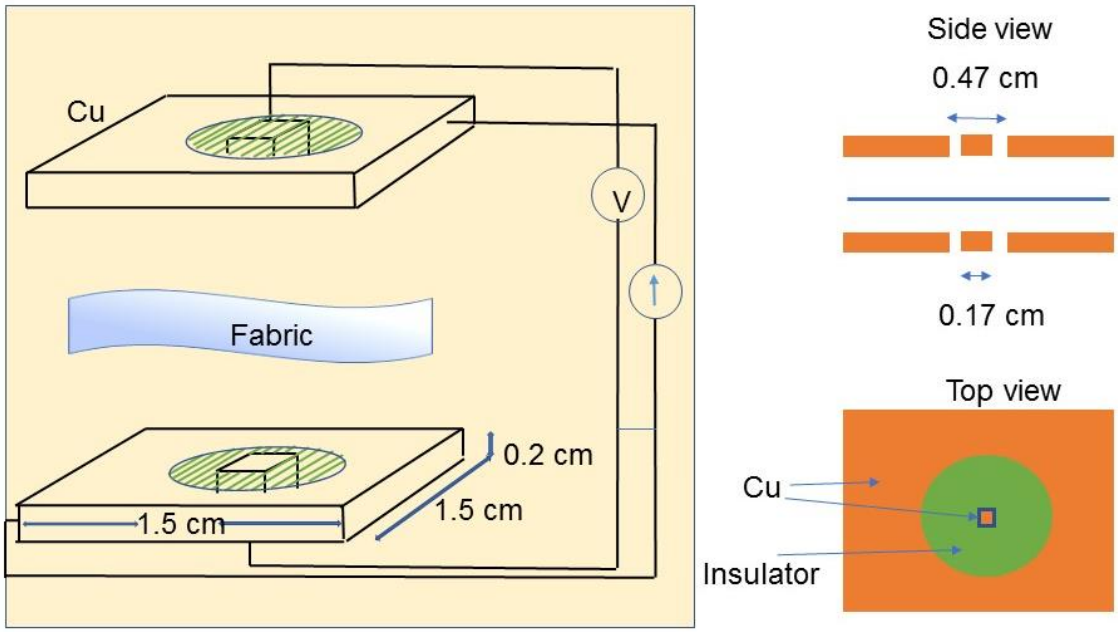

Fig 16: Electrical resistivity measurement system

$$R = \frac{\rho . L}{A} \qquad \text{.....(1)}$$

R= Resistance

L= Length between voltage leads

ρ = Resistivity of sample

Diameter, d = 0.47 cm

Radius, r = 0.235 cm

Area of circle, a = πr^2= 3.14 x $(0.235)^2$ = 0.173 cm^2

Area of sample = 1 cm^2

Effective area, A = Area of sample = 1 cm^2- 0.173 cm^2= 0.827cm^2

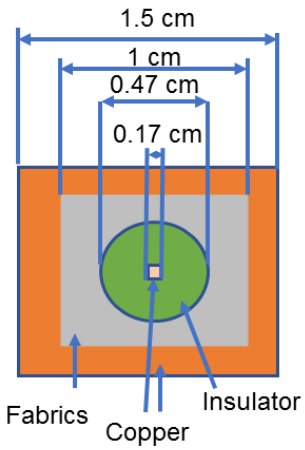

Figure 17: Dimension of electrode used in electrical measurement system

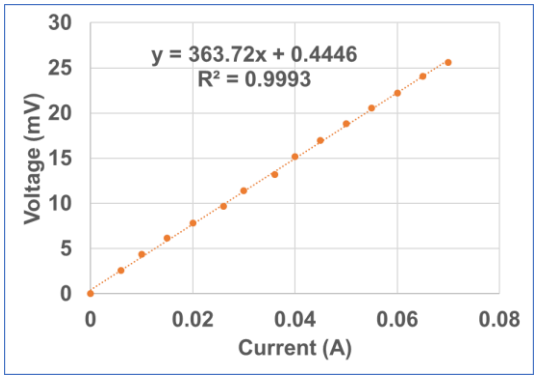

Figure 18: Evaluation of electrical resistance for the single layer of NCF

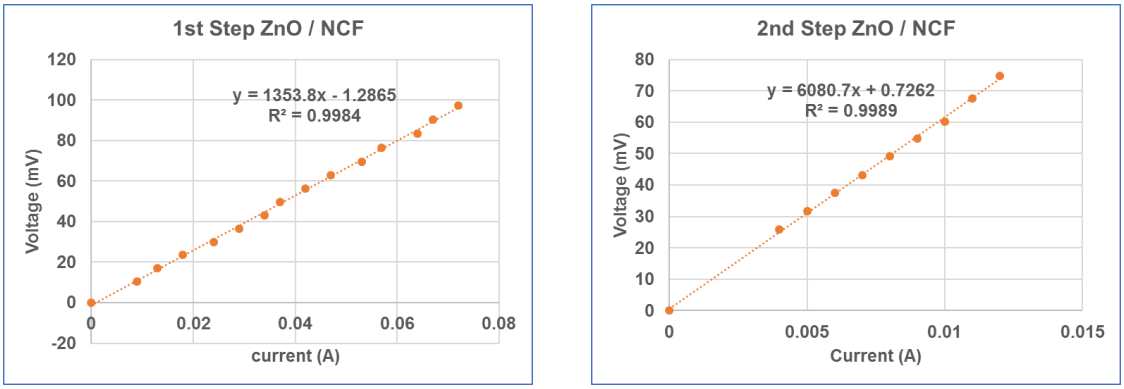

Figure 19: Comparison of resistance for 1st step ZnO/NCF and 2nd step ZnO/NCF in the vertical direction.

Fig 18 and 19 show the resistance of NCF and ZnO / NCF in the vertical direction. The resistivity is calculated from equation 1 described above, and the values are concluded in Table

5. The value of resistivity is found to increase after fabrication of ZnO, and further increases on increasing the quantity of ZnO. This increase in resistivity is considered because of presence of ZnO because ZnO itself is having high resistivity. Therefore, the complete structure of fabric with ZnO shows high resistivity.

Table 5: This table shows the resistivity of NCF and ZnO / NCF

Sample	Resistivity (mΩ.m)
NCF original	111.4
1st ZnO/NCF	414.66
2nd ZnO/NCF	1862.4

3.4. Synthesis of reduced graphene oxide nanostructures

All chemicals were in high purity and used without any further purification. The chemicals used in this process are graphite, sodium nitrate ($NaNo_3$), sulfuric acid (H_2SO_4), potassium permanganate ($KMnO_4$), hydrogen peroxide (H_2O_2), Hydrazine monohydrate (H_6N_2O). No scouring process or any other cleaning process was used for cleaning the fabric. The hydrothermal method was used to reduce GO to rGO directly on conductive fabric. Firstly, GO was synthesized using Hummer's method. Then, original fabric of 5 x 5 cm^2 was immersed in GO and ultra-sonicated for 24 h. After that, GO deposited conductive fabrics were washed three times with DI water and dried for 24 h at 45℃. In order to convert the deposited GO on fabric into rGO, the dried fabric was put in solution of 100 mL DI water and 0.5 M of mono-hydrazine and the solution was stirred for 5 min. Then, the stirred solution was transferred into Teflone - lined autoclave and was kept in furnace for 48 h at 90℃. Finally, dried the sample for 2 h at 60℃. The complete process is shown in flow chart below:

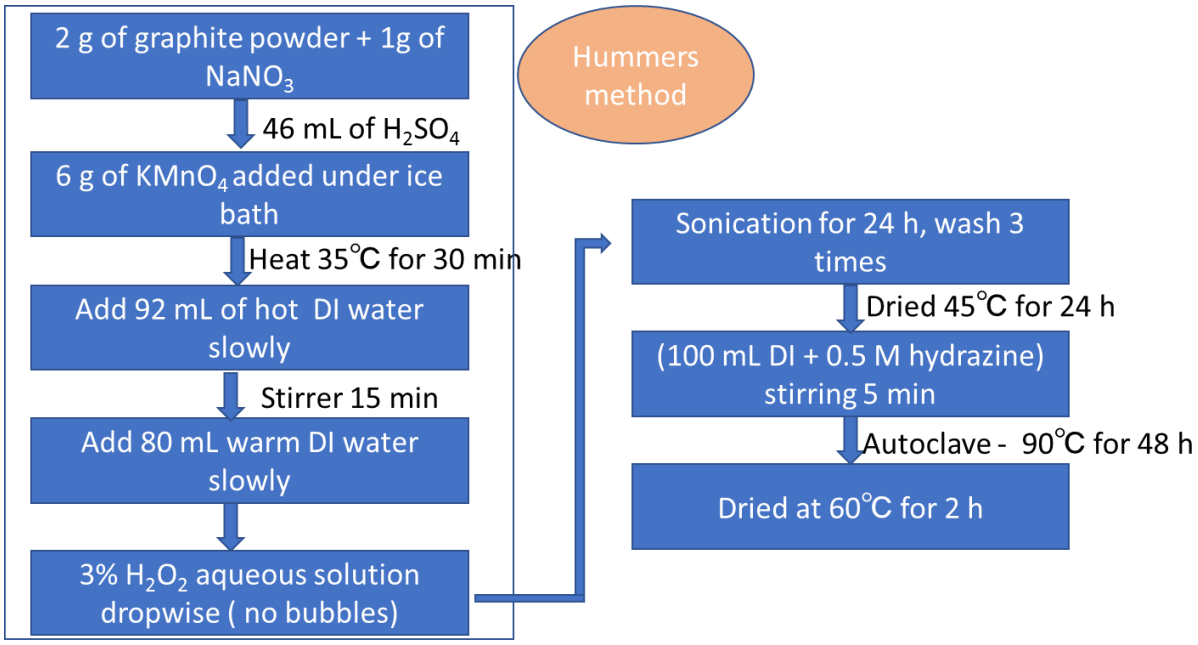

Figure 21: Flow chart for rGO synthesis

3.5. Result and discussion for rGO / NCF

3.5.1. Scanning electron microscopy (SEM)

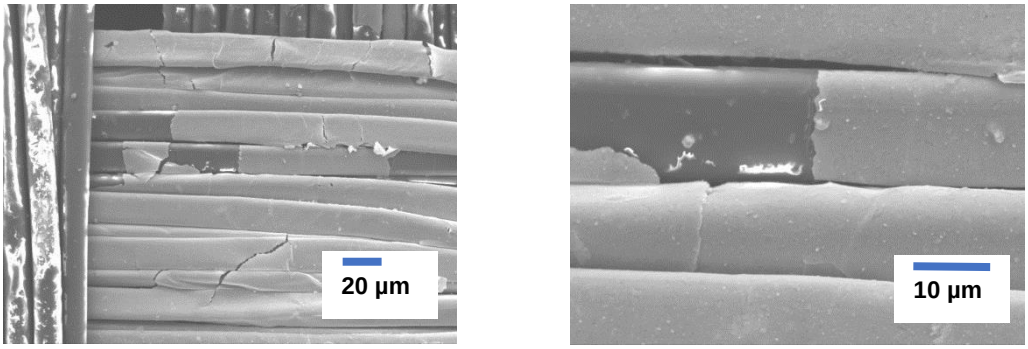

Figure 22: SEM images of rGO / NCF

The morphology of rGO on conductive NCF fabric is shown by the SEM images, which clearly tell that thick sheet-like structure is spread all over the surface. However, the remaining area which looks uncovered is actually covered with fine rGO sheets. This shows the good adhesion between the NCF fabric and the rGO.

3.5.2. X-ray diffraction

XRD pattern of original and rGO coated NCF is shown in Fig 23. The cu peak is completely disappearing in the rGO / NCF graph which may be due to thick layer of rGO sheets or may be due to the insertion of cu atoms inside the aromatic ring of rGO sheets. However, further investigation is required to give the exact explanation.

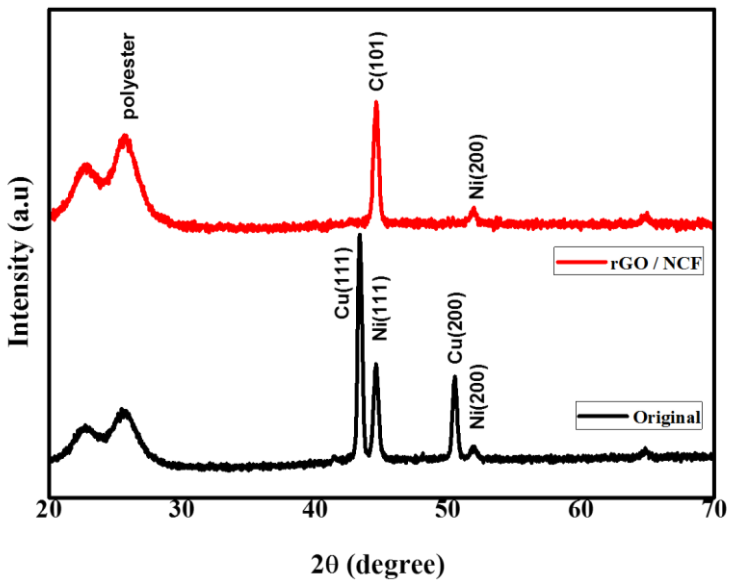

Figure 23: XRD pattern for rGO / NCF

3.5.3. Seebeck coefficient

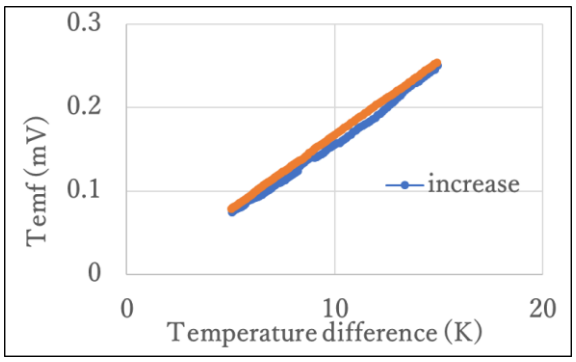

Figure 24: Relation between Temf and ΔT

Table 6: Seebeck coefficient of rGO / NCF

Sample	S_{vert} [μV/K]
Original	-2.7
rGO / NCF	-17.08

The relationship for single layer of rGO / NCF between thermoelectromotive force and temperature difference is shown in Fig 24, linearity of this graph suggest that the data is reliable and depicts the value of -17.08 μV/K for Seebeck coefficient. The comparison of Seebeck values for original single layer NCF and rGO / NCF measured in vertical direction is shown in table 6.

3.5.4. Electrical resistivity

The electrical resistance is found to ~ 37940 mΩ, which is quite high as compared to the original fabrics, and the resistivity is calculated to be 11620.8 mΩ.m. These high values of resistivity in the formed fabric comes from the irregularities/defect created during the formation of rGO or though the interface interaction between rGO and fabric surface. When the charge carrier moves through the material, it scatters with the defects or the grain boundaries present in the material. Some of the reporters suggested that the graphene oxide is not conductive, and the reason of its insulator type behavior is because of absence of π- conjugated orbital system. This conductive behavior of rGO suggests that the extensive conjugated sp^2 carbon network may be restored in the formed rGO.

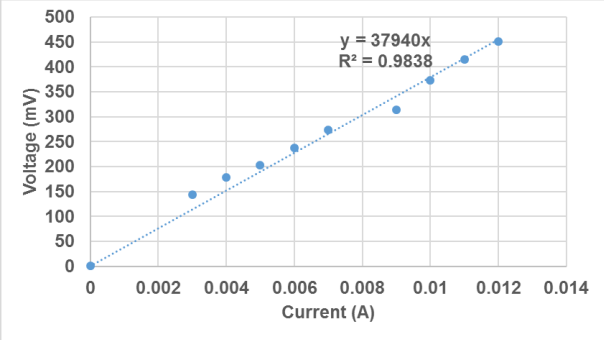

Fig 7: Evaluation of electrical resistance for rGO on NCF

3..6. Summary

For the application of thermoelectric power generators, highly dense and clearly grown ZnO nanostructures were fabricated on a conductive NCF in a vertical direction. The Seebeck coefficient was measured in horizontal and in vertical directions using our home-made apparatuses and found to be in order of -1.3 to -2.7 [μV/K] and -2.7 to - 4.5 [μV/K], respectively. Similarly, Seebeck values are measured with single and multiple layers for NCF and compared against horizontal direction. Moreover, it is found that the Seebeck coefficient negatively increases by fabricating the ZnO on the NCF. Considering that ZnO is usually an n-type semiconductor, the ZnO nanorod contributes to enhancing the Seebeck coefficient. Furthermore, the adhesiveness of ZnO nanostructures is also checked by a laundering process. It is found from SEM images that there are nano-microrod structures on the NCF surface which may be attached through physisorption only. Around 2.82 mg of ZnO nanorods per 1 cm^2 of substrate is removed by the laundering process, confirmed by Seebeck values. High crystallinity and hexagonal structures of nanostructure were depicted by XRD analysis. The resistivity in the vertical direction of ZnO/NCF has been evaluated and found to in the range of 111.4 to 1862.4 mΩ.m, while further values are confirmed by Hall effect instrument. rGO sheets on NCF have been confirmed by SEM and XRD analysis. Seebeck values for rGO shows sudden increase in values up to -17.08 [μV/K]. n-type semiconductor behavior is observed for both pristine and rGO/NCF. Electrical resistivity of rGO/NCF is evaluated to ~ 11620.8 mΩ.m.

Reference:

1- Ismail, Basel I.; Ahmed, Wael H. (2009-01-01). "Thermoelectric Power Generation Using Waste-Heat Energy as an Alternative Green Technology". Recent Patents on Electrical & Electronic Engineering (Formerly Recent Patents on Electrical Engineering). **2** (1): 27-39. doi:10.2174/1874476110902010027

2- Rowe DM. Thermoelectric waste heat recovery as a renewable energy source. Int J Innov Energy Syst Power, 1, 13-23, 2006.

3- M. Kanatzidis, "Ultralow thermal conductivity and high thermoelectric figure of merit in Sn Se crystals", Nature, 508 (7496), 373–377, 2014.

4- L.D. Hicks and M.S. Dresselhaus, "Thermoelectric figure of merit of a one-dimensional conductor," Phys. Rev. B, 47, 16631 - 16634, 1993.

5- D. Li, Y. Wu, P. Kim, L. Shi, P. Yang, and A. Majumdar, "Thermal conductivity of individual silicon nanowires," Appl. Phys. Lett., 83, 14, .2934–2936, 2003.

6- N. Neophytou and H. Kosina, "Effects of confinement and orientation on the thermoelectric power factor of silicon nanowire," Phys. Rev. B, 83, 24 245305-1–16, 2011.

7- M.E. Ghazi, M. Izadifard, F.E. Ghodsi, M. Yuonesi, J. Supercond. Nov. Magn. 25 101-108 2012.

8- A. Yildiz, B. Kayhan, B. Yurduguzel, A.P. Rambu, F. Iacomi, S. Simon, J. Mater. Sci. Mater. Elect., 22 1473-1478 ,2011.

9- X.Wang, L. Zhu, L. Zhang, J. Jiang, Z. Yang, Z. Ye, B. He, J. Alloys Compd. 509, 3282-3285, 2011.

10- G. Merhan Muğlu, S. Sarıtaş, T. Çakıcı , B. Şakar, M. Yıldırım Effect of Copper and Nickel Doping on the Optical and Structural Properties of ZnO, AIP Conference Proceedings 1815, 050008 , 2017

11- Mohammad Suja, Sunayna B. Bashar, Muhammad M. Morshed, and Jianlin Liu, Realization of Cu-Doped p-Type ZnO Thin Films by Molecular Beam Epitaxy, ACS Appl. Mater. Interfaces, 7, 8894−8899, 2015

12- Xueke Xia, a Jian Xie, Shichao Zhang, Bin Pan,d Gaoshao Caob and Xinbing Zhao, Ni3S2 nanosheets-anchored carbon submicron tubes arrays as high performance binder-free anode for Na-ion batteries, Electronic Supplementary Material (ESI) for Inorganic Chemistry Frontiers, 2016

13- M. Aziz Choudhary, Zahoor Ahmad, Aysha Hassan, Y. Khan & Muhammad Aslem 10-Synthesis and Characterization of ZnO/CuO nanocompsites on Porous 3D Ni Substrate and its Photo-electric Behavior., ISSN: 1553-3174, 2016

14- Jinping Liu,Yuanyuan Li, and Xintang Huang, Department of Physics, Central China Normal University, Wuhan 430079, Hubei, P.R. China ZnO Nanoneedle Arrays Directly Grown on Bulk Nickel Substrate for Li Ion Battery Electrodes with Improved Performance 978-1-4244-1573-1/08

Chapter 4: Fabrication of ZnO and rGO Nanostructures on Conductive Carbon Fabric (CAF)

4.1. Introduction to CAF

With the hope of increasing efficiency of thermoelectric generators, researchers are trying to focus more and more on investigating the new materials [1]. A recent boom in the usage of carbon fibers in aerospace, sports and automobile industries gather the attention of researchers. In 1977, M. Endo reported the thermoelectric power of carbon fibers prepared by benzene [2]. Priyanka R. Jagadish et al., reported the deposition of bismuth telluride (Bi2Te3) and bismuth sulfide (Bi2S3) over the virgin and recycled carbon fiber, and reported the Seebeck coefficient for the same [3]. Many researchers worked on the Seebeck coefficient of flexible carbon materials such as carbon fiber [3]-[6]. Graphite has enormous qualities that makes it useful in many applications. For example, flexible graphite exhibits large surface area, due to exfoliation process. And, because of the involvement of microstructural graphite layers parallel to the sheet surface, flexible graphite exhibits high thermal and electrical conductivities [7].
Besides, the improvement in figure of merit attempts should be made in the other direction as well such as the development of eco-friendly, cost-effective and high-power factor materials. In this chapter we will focus on conductive Carbon fabric (CAF), as a flexible substrate. This conductive CAF is expected to increase the electrical conductivity and hence Z. In addition, ZnO nanostructures coating over will increase Seebeck coefficient due to confinement of carriers and phonon [8]-[10]. Up to our knowledge no one reported the thermoelectric properties of CAF, especially in vertical direction.
The fabric used in this study was purchased from Sainergy fuel cell India pvt. ltd, weave construction plain, wrap per(cm)-19.3, weight- 132 g/m, measured thickness - 0.25 mm.

4.2. Experimental procedure

4.2.1. Synthesis of ZnO nanostructures

The same procedure as adopted for the NCF was taking into consideration, that is the creation of seed layer followed by nanostructured growth. In this study also, a two-step hydrothermal synthesis is used to synthesize the nanostructure of ZnO over the CAF as done for the NCF, formation of seed layer step (first step) followed by growth step (second step). The seed layer is grown during this first step process, in which seeds act as templates for the growth of crystal. For the proper growth of nanostructures, it is important to have proper nucleation all over the surface of the fabric. For the optimization of nanostructures, synthesis is carried out at different ratios, temperatures and annealing times as shown in table 1, and details are given for CAF1 as an example.

Table 1: Types of sample and their specifications

Sample	Ratio (ZN: HMT)	Growth time (h)	Annealing temperature (℃)
CAF1	1:2	1	60
CAF2	1:2	1	120
CAF3	3:1	1	60
CAF4	3:1	1	120
CAF5	1:2	5	60
CAF6	1:2	5	120
CAF7	3:1	5	60
CAF8	3:1	5	120

Formation of seed growth (first step) for CAF1:

In the first step, the seed layer of ZnO was prepared by mixing the solutions of 0.1 M of Zinc nitrate hexahydrate [$Zn(NO_3)_26H_2O$] in 50 mL of distilled(DI) water and 0.2 M of Hexamethylenetetramine $(CH2)_6N_4$ in 50 mL of DI water, and stirred the solution at 50°C for 2h after immersing the CAF fabric. During this stirring process, the water turned milky color and the black color fabric turned out to be whitish, indicating the formation of seeds over the fabric. Then, the solution containing the fabric was set in Teflon - lined autoclave for 1 h at 120°C. Finally, the sample is washed three times with DI water and then annealed at 60°C for 2 h., as shown in figure 1.

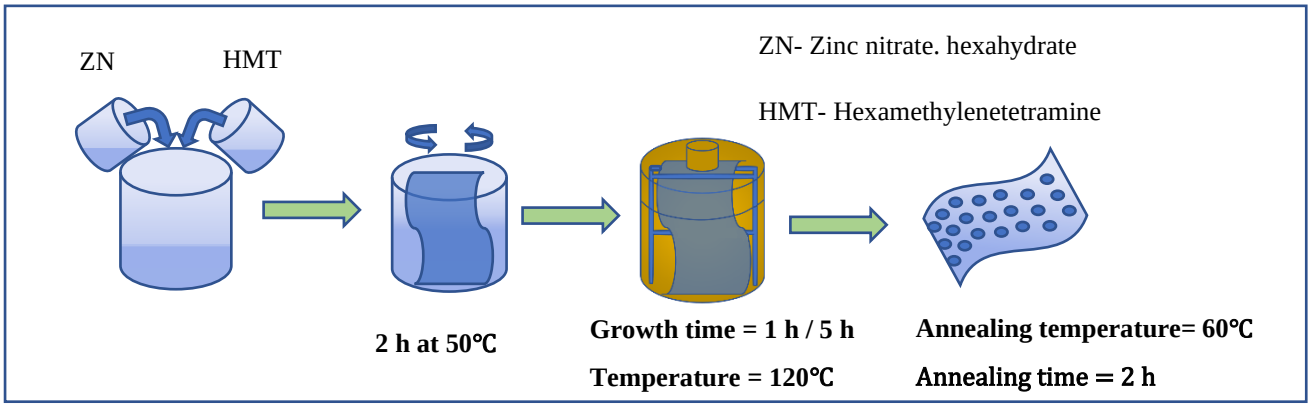

Figure 1: This figure shows the first step process

Nanostructure growth (second step) for CAF1: For the growth of nanostructures over the fabric, as a second step, solutions of molar ratio (1:2) of Zinc nitrate hexahydrate [$Zn(NO_3)_26H_2O$] and $(CH2)_6N_4$ are mixed together and solution with seed layer formed in first step is stirred with the solution of 2 h at 50℃ and growth time set to 5 h and finally the

sample is washed three times with DI water and annealed at 50°C for 2 h, as shown in Fig.2

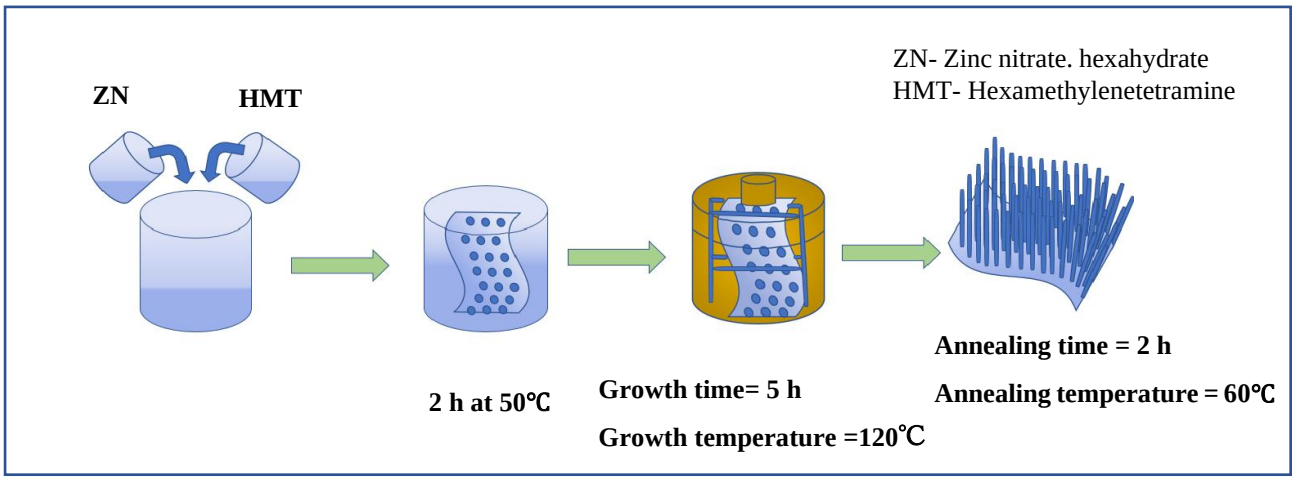

Figure 2: Shows the second step (growth) process for CAF

4.3. Result and discussion

4.3.1. Scanning electron microscope (SEM)

Fig 3 shows that SEM images of bare (original) and first step ZnO seed layer over CAF. Fig 3(a),(b),(c) shows the images for the original fabric which illustrate that the fabric is free of defect and there is no impurity over the fabric's fiber. The diameter of fiber is estimated to be 3-5µm. Fig 3(d),(e),(f) illustrate the images of CAF 1, showing the best suitable condition, as full surface is covered by the seed layer(thread-like structures) of ZnO, depicted by zoomed image. Fig 3(g), (h), (i), show the images for CAF2, no seed layer structure is visible, only agglomerated particles of ZnO are visible and after agglomeration they took the round shape. Fig 3(j),(k),(l) shows the images for CAF3, in which seed layer is almost not visible but thin nanorods, tightly bound to the surface in the parallel direction are visible and finally Fig 3(m),(n),(o) shows the images for CAF4, having few ZnO sticks to the CAF with agglomerated sheet-like structure at some parts. Similar trends can be seen in 4(a)-(l), where the surface is not fully covered with ZnO seeds. However, Fig 4(g)-(i) shows good formation of solid, well-shaped (hexagonal), and well - separated nanorods. This scanning electron microscopy suggest that the best choice, that is CAF1, hence we proceed for the second step only for the CAF1.

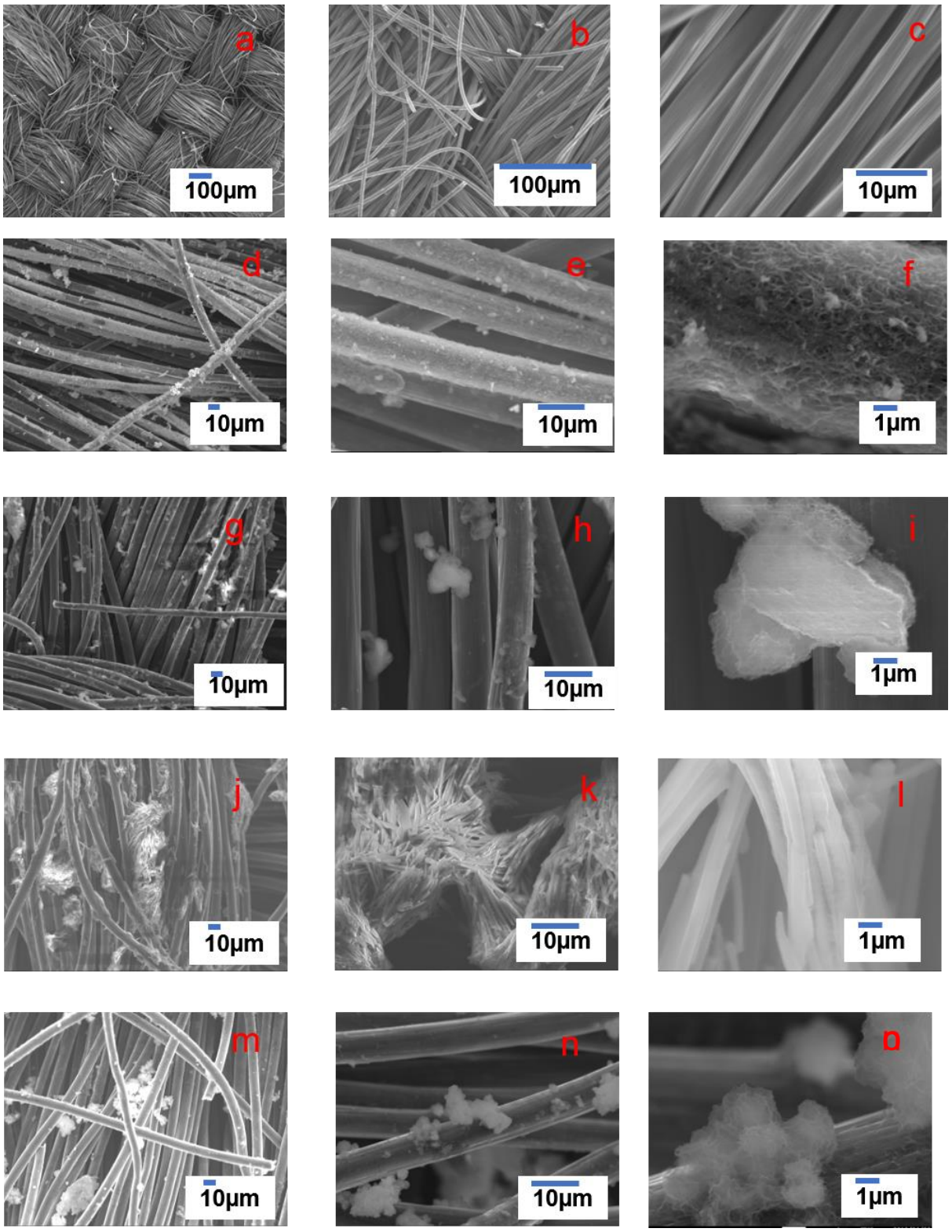

Figure 3: Show the SEM images of CAF to CAF4

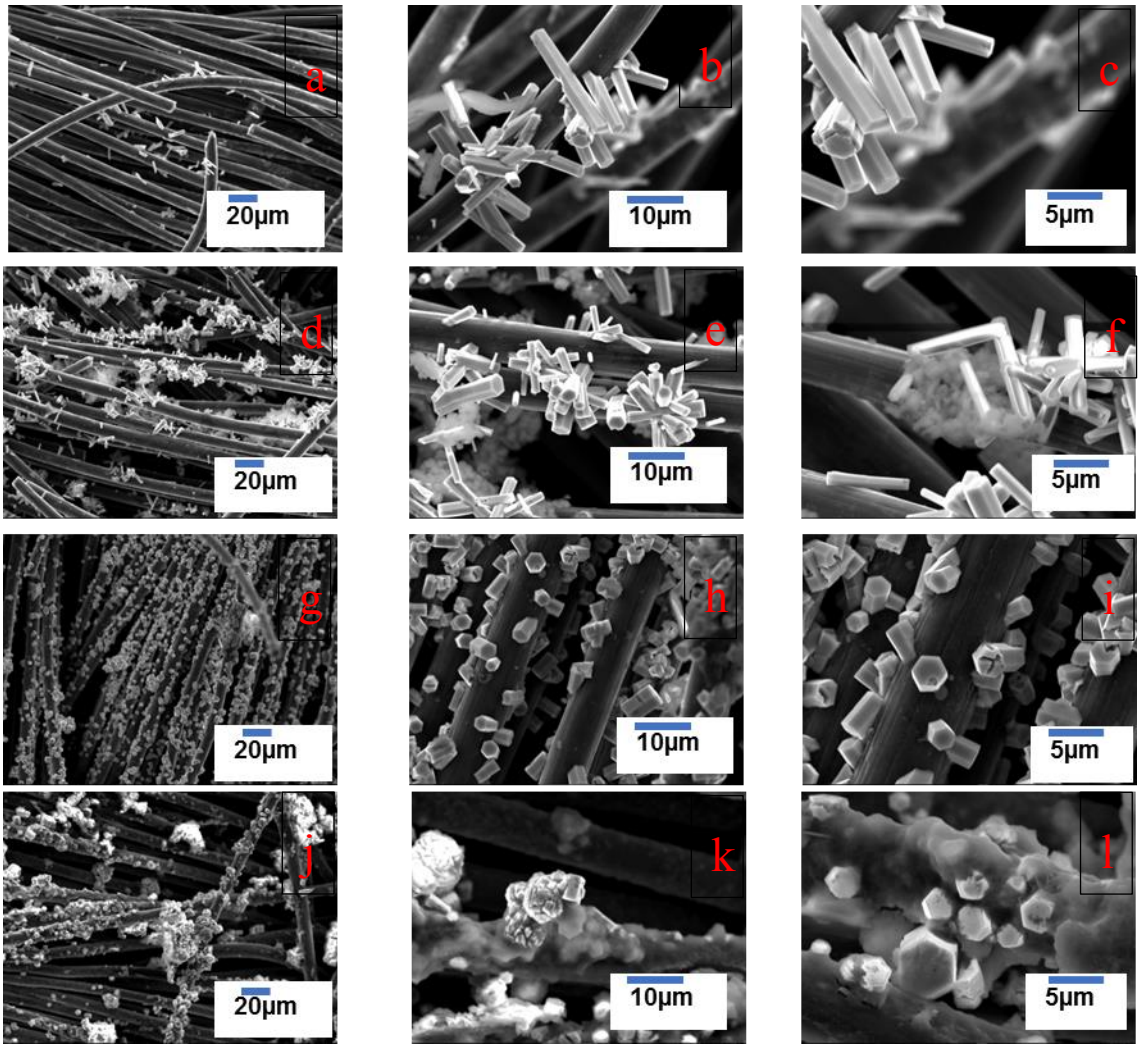

Figure 4: (a)-(c), (d)-(f), (g)-(i) and (j)-(l) show the SEM images of CAF5, CAF6, CAF7 and CAF8, respectively

Figure 5 shows the SEM images for second step process for CAF1 at different zoom. It can be clearly seen that only few nanorods have been grown over the surface of CAF, but almost full surface is covered with the thread/sheet like structures.

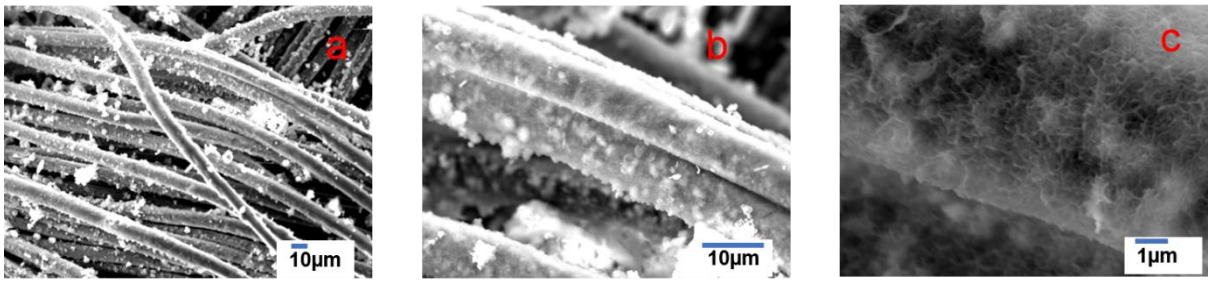

Figure 5: (a), (b), (c) shows the SEM images of second step ZnO / CAF at different resolutions.

4.3.2. EDXA mapping

Chemical composition is analyzed by EDXA mapping technique. Fig 6(a)-(c) shows the EDAX mapping for original CAF, in which image (c) clearly shows the presence of carbon, similarly images from 6(d)-(g) shows the images for first step ZnO / CAF , 6(h)-(k) show the images for second step ZnO / CAF. The presence of Zn can be clearly seen in 6(g), (k). As we move from first step to second step images gets clear because of presence of more and more Zn and O content, present in ZnO, however images for carbon gets fainted due to the thick surface of ZnO over CAF. The percentage of elements present is shown by tables attached to graphs. Fig 7 shows that there is no impurity in the formed nanostructures.

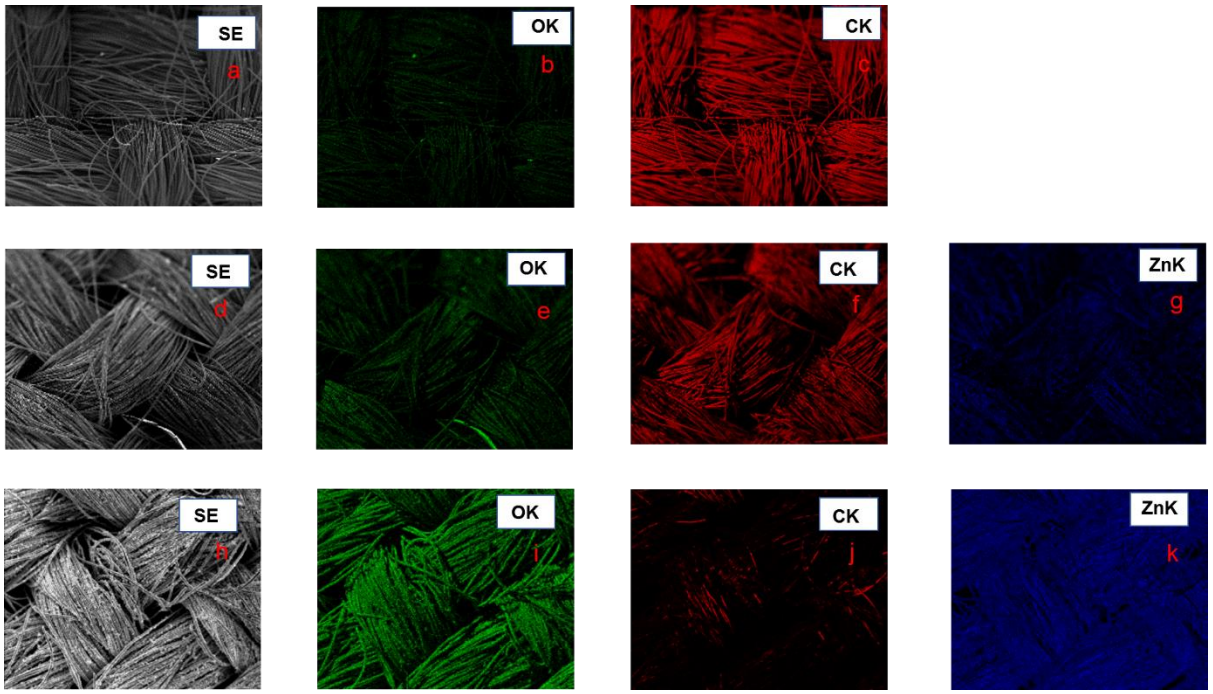

Figure 6: Mapping for original CAF (a)-(c), 1st step ZnO / CAF (d)-(g) and 2nd step ZnO / CAF(h)-(k).

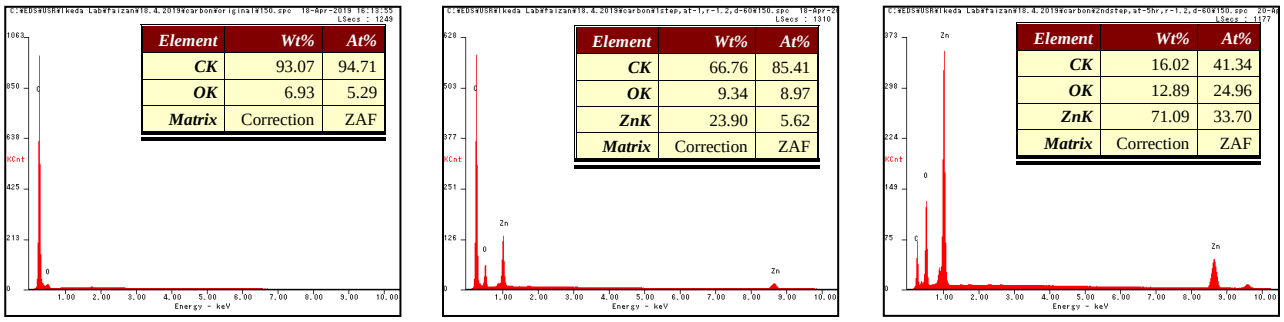

Figure 7: EDX analysis for (a) original CAF, (b) 1st step ZnO / CAF, (c) 2nd ZnO / CAF

4.3.3. X-ray diffraction (XRD)

In this study, we have analyzed three different samples of original CAF, 1st step ZnO/ CAF and 2nd step ZnO / CAF. Fig 8 represents the XRD data of these samples that is employed to investigate crystallinity, crystalline phase, and direction of prepared nanorods. The XRD pattern of original CAF shows clear peak of graphite at 26°[11] and a small one at 45°[11],depicting in Fig 8. Only one peak of ZnO at 36.100° is present in the 1st step. However, presence of nanostructured ZnO prominent peaks can be seen in the 2nd steps more clearly, such as at 31.619°, 34.335°, 36.100°, 47.367°, 56.313°, 62.645° and 68.737° (JCPDS card no. 01-079-0208), however the sharp peaks are visible only in second step, shows the crystallinity of ZnO material. Herein, the ZnO XRD patterns were indexed to the wurtzite structure of ZnO. Considering the ZnO nanorods' directions XRD results are perfectly matched with alignment of nanorods array on the surface of CAF observed in SEM images and EDAX graphs.

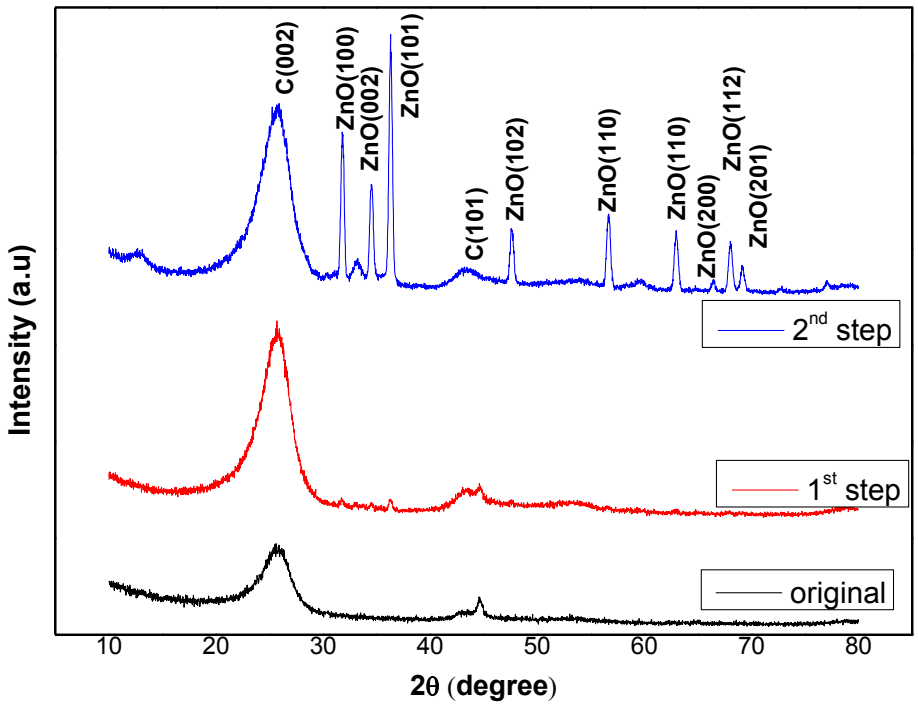

Figure 8: This figure shows the XRD graph for original CAF, 1st step ZnO/ CAF, 2nd step ZnO / CAF

4.3.4. Seebeck Coefficient

Similar to previous procedures, same procedure is applied to find out the Seebeck coefficient of CAF and fabricated carbon fabric. An example of the time evolutions of TEMF, T_L and T_H for the CAF is shown in Fig. 10. It is clearly observed that the TEMF negatively increases with the temperature difference ΔT. Figure 11 shows the relationship between TEMF and temperature difference replotted from Fig. 10. In this figure, "Increase" means the data collected from the range where the temperature difference is increasing, and "Decrease" corresponds to the data under decreasing the temperature difference in Fig. 10. Both "Increase" and "Decrease" data are nearly identical. This fact means that the measured data are reliable even for flexible materials. In addition, both data make a linear relation, indicating that the Seebeck coefficient is nearly constant in the measured temperature range. The Seebeck coefficient S was evaluated from the TEMF ($\Delta V = V_H - V_L$) and the temperature difference ($\Delta T = T_H - T_L$) by $S = -\Delta V / \Delta T$ near room temperature. Therefore, the average Seebeck coefficient of CAF is evaluated from the gradient of the linear graph to be $S_{CAF} \sim 5.05$ μV/K, which is close to that of the same CAF obtained in the horizontal direction, 5.32 μV/K using the apparatus shown in Fig 9 and described in previous chapters. Values of the Seebeck coefficient increases with the number of layers, as shown in Fig 12, which is considered due to the presence of air gaps between each two layers of CAF. The Seebeck coefficient is positive, indicating that the CAF used is a p-type material. The vertical and horizontal Seebeck coefficients of these samples are summarized in Table 2. All samples have positive Seebeck coefficients or a p-type semiconductor. It is found that the

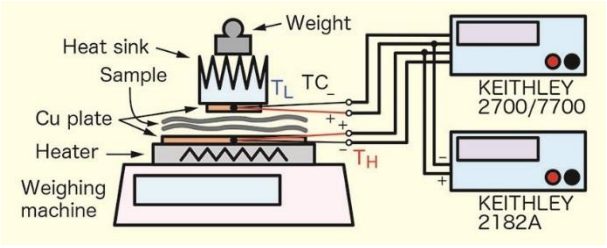

Figure 9: Schematic diagram of developed Seebeck coefficient measurement system.

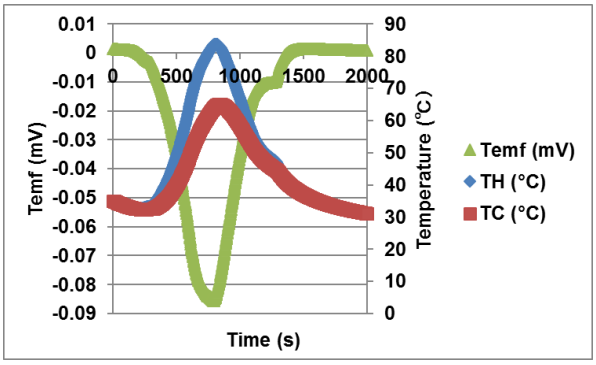

Figure 10: Time evolutions of TEMF and temperatures at hot T_H and cold T_L junctions for single CAF layer

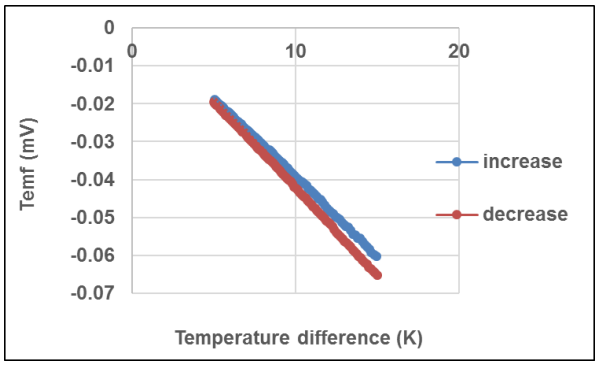

Figure 11: Relationship between TEMF and temperature difference for single CAF layer. "Increase" and "Decrease" correspond to the data collected from the range where the temperature difference is increasing and decreasing, respectively, in Fig. 10.

Seebeck coefficient decreases by fabricating the ZnO on the CAF. Considering that ZnO is usually an n-type semiconductor, the ZnO nanorod contributes to enhancing the Seebeck coefficient in the negative direction. As can be seen, Seebeck is decreasing more in the vertical direction, which is the obvious reason, i.e. double layer of ZnO over both sides of fabric.

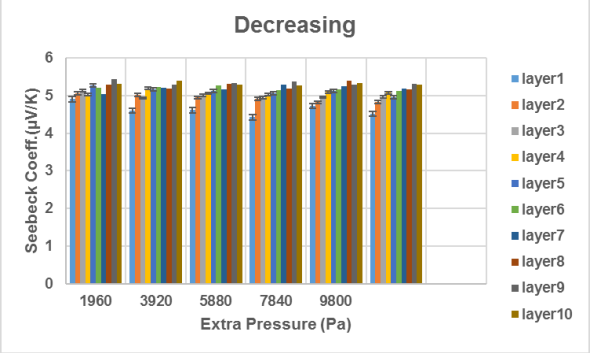

Figure 12: Relationship between Seebeck coefficient and the number of stacked CAF layers

Table 2: This table represents the Seebeck coefficient values of CAF and ZnO / CAF

CAF	S_{Vert} [μV/K]	S_{Horiz} [μV/K]
Original	5.05	5.32
1st Step ZnO / CAF	4.95	5.20
2nd Step ZnO / CAF	4.98	5.06

4.3.5. Laundering process

Same procedure of laundering is applied for this fabric also, just to check the adhesiveness of ZnO over the CAF substrate. This time also the fabricated fabric is sonicated for 3 times 5 min for each in 50 mL of DI water, then fabric is stirred in 100 mL of DI water for 2 hours, and finally dried at 60℃ for 2 hours. During this process, no detergent or soap is used, to avoid chemical reaction during the laundering process. The detail of full process is described in the previous chapter. The weight of removed ZnO from the CAF is calculated around 1.9 mg, these readings are the average of three readings, taking before and after of washing process.
Adhesiveness of ZnO after laundering process is shown in SEM images of Fig 13, furthermore, the adhesion is confirmed by XRD, as shown in Fig 14.

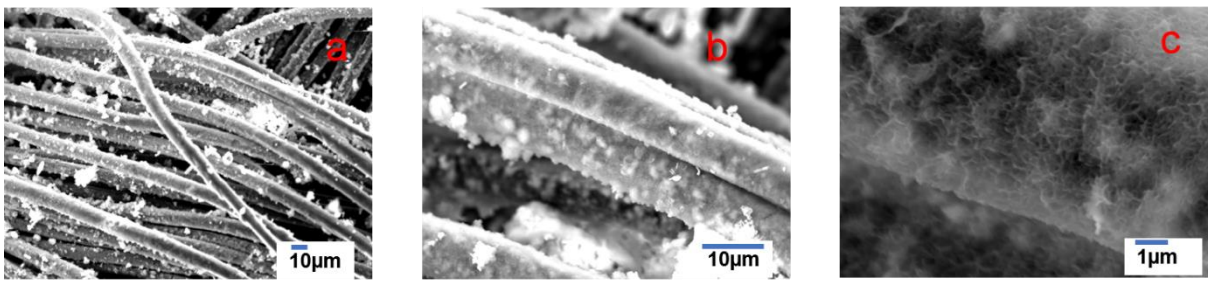

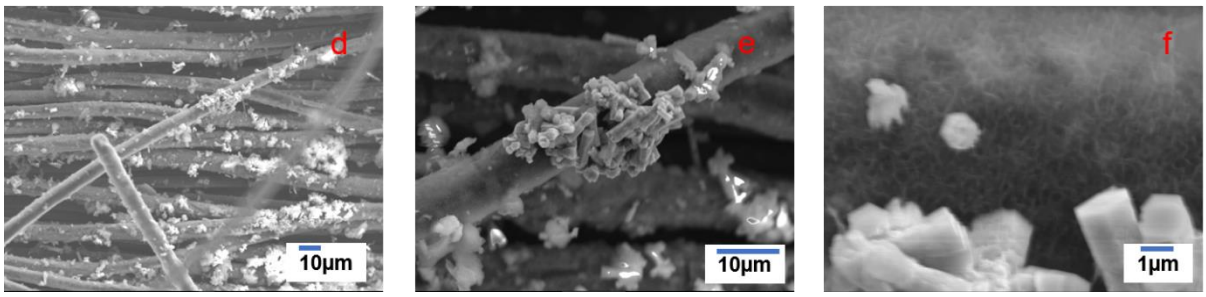

Figure 13: SEM images of, (a)-(c) 2nd step ZnO / CAF before laundering, (d)-(f) 2nd step ZnO / CAF after the laundering process

In addition, the same peaks of ZnO as observed for 2nd step ZnO sample before laundering can be seen in the XRD of samples after the laundering process. However, the peaks are reduced drastically, which may be attributed to less ZnO over the substrate or because of residual water present in the sample.

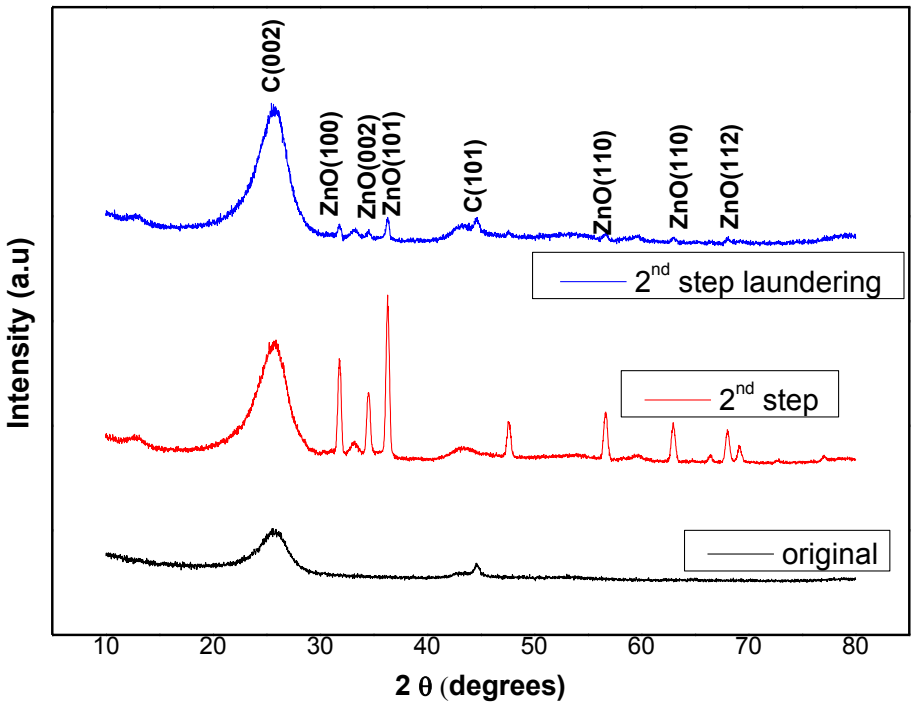

Figure 14: XRD patterns for original and ZnO formed CAF after laundering effect

4.3.6. Electrical conductivity

With the aim of measuring electrical conductivity, same home-made apparatuses are used for the measurement of CAF and ZnO fabricated as described in previous chapters. Used fabric is having as mentioned electrical resistivity of 100.8 mΩ.m. Current (A) is applied at the outer part of the electrode and voltage (mV) generated is measured through the inner electrodes. The I-V graph for the single layer of CAF is shown in Fig 15.

$$R = \frac{\rho . L}{A} \qquad \text{.....(1)}$$

R= Resistance

L= Length between voltage leads

ρ = Resistivity of sample

Diameter, d = 0.47 cm

Radius, r = 0.235 cm

Area of circle, a = πr^2= 3.14 x (0.235)2 = 0.173 cm^2

Area of sample = 1 cm^2

Effective area, A = Area of sample = 1 cm^2- 0.173 cm^2= 0.827cm^2

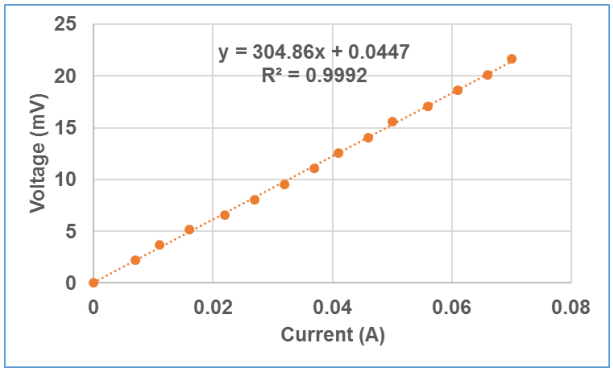

Figure 15: Evaluation of resistance for single layer of CAF

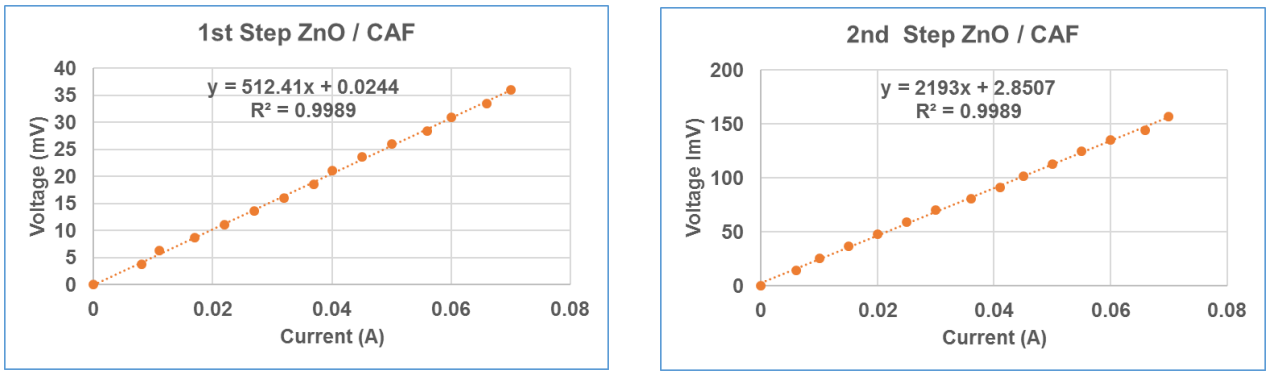

Figure 16: I-V graph to compare the resistance of 1st step ZnO/CAF and 2nd step ZnO/CAF in vertical direction.

The resistivity is calculated using equation 1, described above. Table 3 explains the combined resistivity of CAF and ZnO/CAF. Further the values of electrical resistivity are increasing on increasing the content of ZnO.

Table 3: This table explain the resistivity in vertical direction for original CAF and ZnO /CAF

Sample	Resistivity (mΩ-m)
CAF original	100.8
1st ZnO/CAF	169.5
2nd ZnO/CAF	725.4

4.4. Fabrication process rGO on CAF

The same fabrication process was adopted as proceeded for NCF, this time instead of NCF fabric carbon fabric is taken as a fabric of investigation. Hummer's method was deployed followed by hydrothermal method. A complete flow chart is shown in the Fig 18.

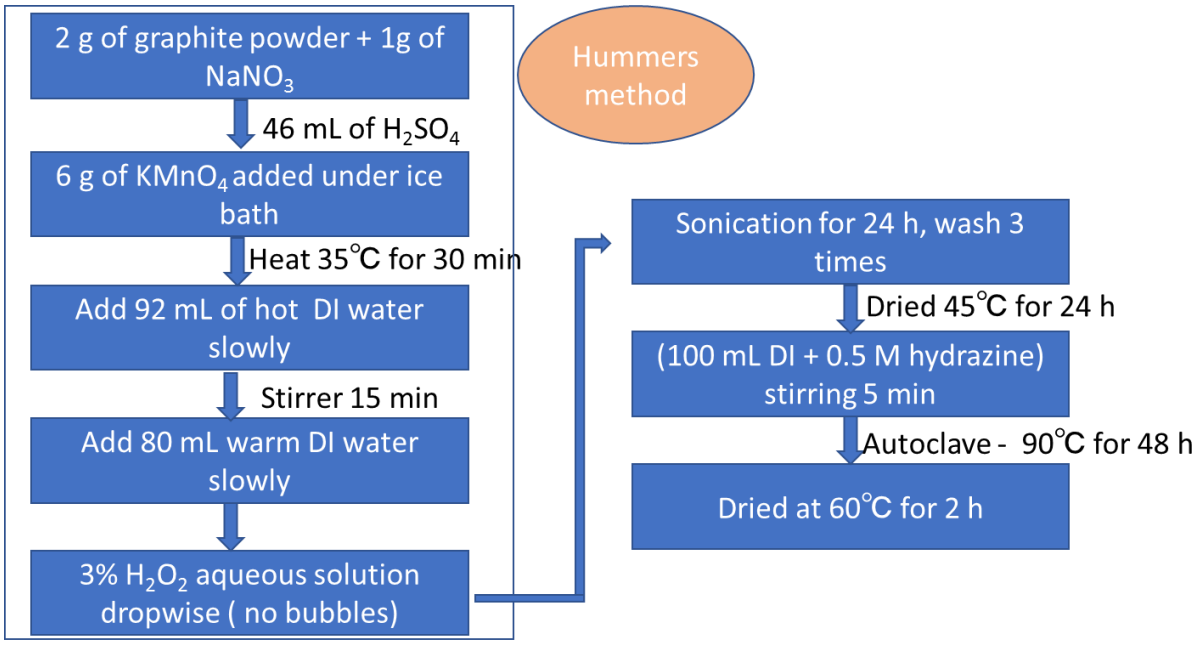

Figure 18: Flow chart for rGO synthesis

4.5. Result and discussion for rGO on CAF

4.5.1. Scanning electron microscopy (SEM)

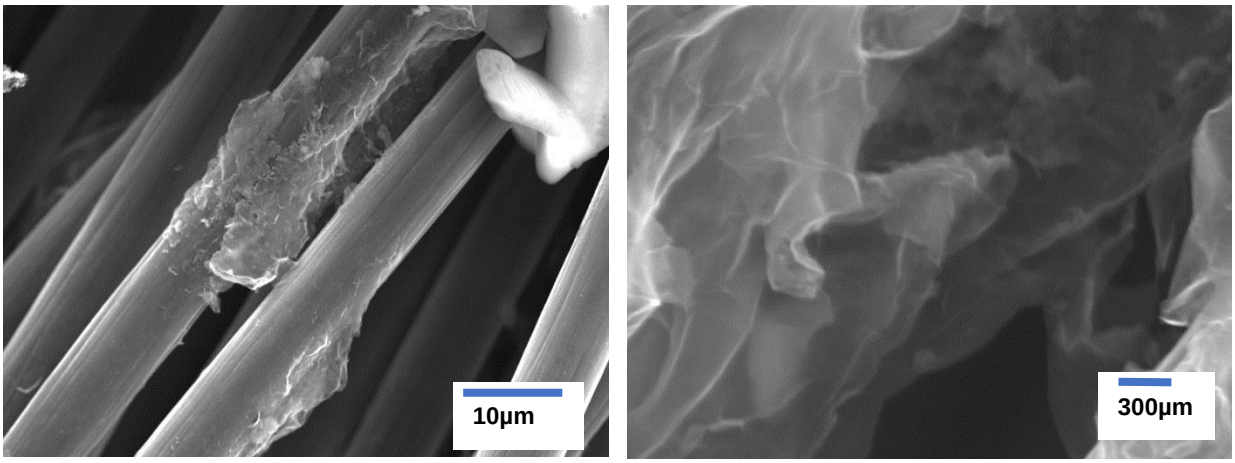

Figure 19: SEM images of rGO / CAF

These SEM images tell the morphology of formed rGO on carbon fabric. The sheets are showing fine structures but not spread all over the fabric, which may be attributed to the less surface energy of carbon atom, due to which it is not possible for carbon atoms to attract another material. Hence, sticking of rGO at only few regions is due to less adhesion between the carbon surface and rGO.

4.5.2. X-ray diffraction (XRD)

XRD images of rGO on CAF is shown in Fig 20. The major peak at 26° and 45° is for graphite. However, it can be clearly seen that there a hike in the peak at 45° degrees, which is due to the formation of rGO sheets. However, the peak at around 65° is still unknown and need further investigation.

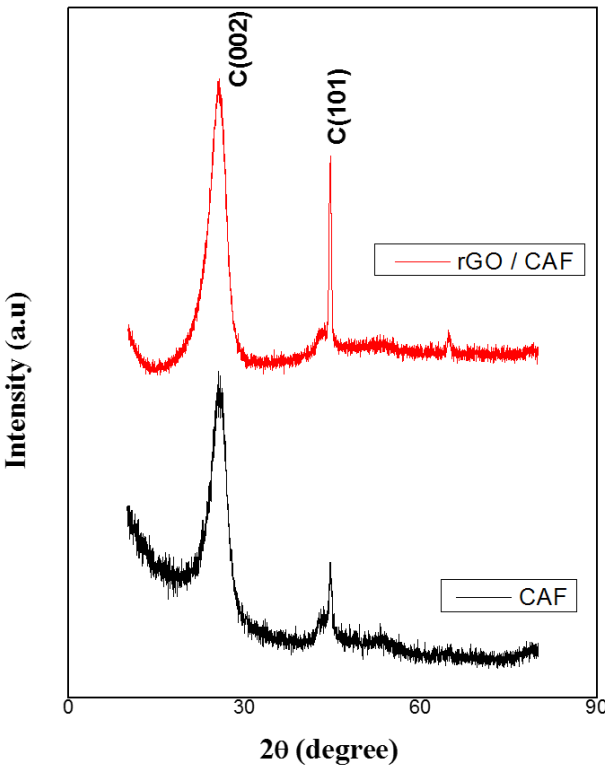

Fig 20: XRD graph for rGO/CAF

4.5.3. Seebeck coefficient of rGO / CAF

As discussed above, there are few sheets formed on CAF surface. Hence, no change is found in the Seebeck coefficient values. The values before and after fabrication of rGO are listed in table 4. Seebeck value after fabrication is ~ 4.7µV/K, which is somewhat lesser than the original fabric. This lesser value is considered due to the error in our measurement system. Hence, we can say that rGO formed over CAF are lesser in quantity and hardly affects the Seebeck coefficient values. The primary influence of these values is due to substrate only.

Table 4: Seebeck values for original and rGO / CAF

Sample	S_{vert} [µV/K]
Original	5.05
rGO / CAF	4.7

4.5.4. Electrical resistivity

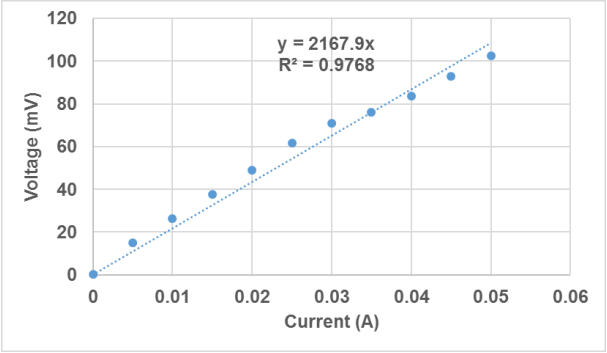

Fig 21: Evaluation of electrical resistance for rGO on CAF

Electrical resistance is found to be increased up to the values of 2167 mΩ after fabrication, and the resistivity is calculated to be ~ 717.4 mΩ.m. This increase in the electrical values is attributed to the defects present in the formed rGO during the formation process.

The slope of the graph shown in Fig 21 shows the resistance value and the linearity predicts the reliability of the data. Some of the reporters suggested that the graphene oxide is not conductive, and the reason of its insulator type behavior is because of absence of π-conjugated orbital system. This conductive behavior of rGO suggests that the extensive conjugated sp^2 carbon network may be restored in the formed rGO, and, hence the final structure of rGO with fabric is showing fine conductivity.

4.6. Summary

To increase the efficiency of thermoelectric power generators and hence ZT values, highly conductive CAF was chosen as a flexible material. Highly crystalline and closely packed ZnO nanostructures were fabricated on CAF. At different ratios and growth time, different structures were obtained. Seebeck coefficients were measured in the horizontal and in vertical directions using our home-made apparatuses. The effect of air gaps is checked by staking a large number of layers and the Seebeck coefficient is measured in vertical direction. It is found that on increasing the number of layers, Seebeck coefficient is increasing. Similarly, Seebeck values are measured for the single layer of CAF with and without ZnO fabrication and the values were compared against horizontal direction. It is found that the Seebeck coefficient decreases by fabricating the ZnO on the CAF. Considering that ZnO is usually an n-type semiconductor, the ZnO nanostructures contribute to enhance the Seebeck coefficient. Furthermore, the adhesiveness of ZnO nanostructures is also checked by a laundering process. It is found from SEM images that there are thread/sheet like nanostructures grown on the CAF surface which may be attached to it through physisorption only. Around 1.9 mg of ZnO nanorods per 1 cm^2 of substrate are removed by the laundering process. High crystallinity and hexagonal structures of nanostructure were depicted by XRD analysis. The vertical electrical resistivity of CAF before and after fabrication have been evaluated. It is found that after fabrication of CAF with ZnO and rGO nanostructures the electrical resistivity goes up to 725.4 mΩ.m and 717.4 mΩ.m, respectively, and the values are confirmed against Hall effect instrument values.

Reference:

1. Priyanka R. Jagadish, Lau Phei Li, Andy Chan and Mohammad Khalid Effect of Annealing on Virgin and Recycled Carbon Fiber Electrochemically Deposited with N-type Bismuth Telluride and Bismuth Sulfide, Materials and Manufacturing Processes, 0: 1–9, 2016.
2. M. Endo, I. Tamagawa and T. Koyama, Thermoelectric power of carbon fibers prepared from benzene, Japanese journal of applied physics, 16, 10, 1771-1774, 1977.
3. D. Robson, F.Y.I. Assabghy, and D.J.E. Ingram, "Some electronic properties of polycrylonitrile-based carbon fibers," J. Phys. D: Appl. Phys., 5, 1, 169–179, 1972.
4. H.Y. Cao, W. Yao, and J.J. Qin, "Seebeck effect in graphite carbon fiber cement-based composite," Adv. Mat. Res., 177, 566–569, 2011.
5. E.J.X. Pang, A. Chan, and S.J. Pickering, "Thermoelectrical properties of intercalated recycled carbon fiber composite," Composites: Part A, 42, 10, 1406–1411, 2011.
6. E.J.X. Pang, S.J. Pickering, A. Chan, K.H. Wong, and P.L. Lau, "Ntype thermoelectric recycled carbon fiber sheet with electrochemically deposited Bi2Te3," J. Solid State Chem., 193, 147–153, 2012.
7. Yie Meng Hoi, D.D.L. Chung, Flexible graphite as a compliant thermoelectric material,
8. Carbon 40 ,1131 –1150, 2002.
9. L.D. Hicks and M.S. Dresselhaus, "Thermoelectric figure of merit of a one-dimensional conductor," Phys. Rev. B, 47, 16631– 16634, 1993.
10. D. Li, Y. Wu, P. Kim, L. Shi, P. Yang, and A. Majumdar, "Thermal conductivity of individual silicon nanowires," Appl. Phys. Lett., 83, 14, 2934–2936, 2003.
11. N. Neophytou and H. Kosina, "Effects of confinement and orientation on the thermoelectric power factor of silicon nanowire," Phys. Rev. B, 83, 24 245305-1–16, 2011.
12. Claudia C. Luhrs, Michael Moberg, Ashley Maxson, Luke Brewer and Sarath Menon, IF-WS2/Nanostructured Carbon Hybrids Generation and Their Characterization, Inorganics, 2, 211-232, 2014

Chapter 5: Fabrication of ZnO and rGO Nanostructures on Conductive Silver Fabric (Ag)

5.1. Introduction to Silver fabric (50% Ag)

Silver is one of the most important elements in the periodic table, having atomic number 47 and symbol Ag, known for its highest electrical and thermal conductivity [1]. Not only in the field of medicine, Jewellery and silverware, Electronics, Brazing alloys, Chemical equipment, Photography[2][5], having applications in almost every field. In the field of thermoelectric also Ag is getting its roots deeper day by day. Further enhancement in different applications takes place, due to its easy transformation into nanoparticles. Much literature is available on the thermoelectric properties of silver [6], [7], but, with the aim of wearable flexible thermoelectric generators (WTEG), Ag cannot be used singly, it must need some polymer that can make it flexible and usable for wearable applications. Nylon is a synthetic polymer based on aliphatic or semi-aromatic polyamides[8], with applications in fabric and fibers, food packaging, in shape formation(cars, machines)[9].

Besides, the improvement in figure of merit attempts should be made in other directions as well, such as development in eco-friendly, cost effective and high-power factor materials. In this chapter we will focus on conductive Silver fabric (50% Ag), as a flexible substrate. This conductive Ag is expected to increase the electrical conductivity and hence Z. In addition, ZnO nanostructures coating over it will increase the Seebeck coefficient due to confinement of carriers and phonon [10]-[12]. Up to our knowledge, we are the first who is going to report thermoelectric properties of Ag, especially in vertical direction.

The fabric used in this study was purchased from Beijing, China. This fabric consists of 50% silver and 50% nylon. It has weight of 80 g/ sqm, yarn count (fineness or coarseness) 40d, shielding efficiency > 99.9% and measured thickness of 0.15 mm.

5.2. Experimental procedure

5.2.1. Synthesis of ZnO nanostructures

Alone neither Ag nor nylon may not be capable of producing good thermoelectric results, as Ag has good electrical conductivity but a lower Seebeck coefficient (metal) and nylon has very inferior electrical conductivity [13]. Therefore, we have focused our attention on this fabric consisting of half silver and half nylon. The same synthesis method and same procedure are applied as we did for NCF and CAF. Therefore, a two-step hydrothermal synthesis is used to synthesize the nanostructured ZnO over 50% Ag, seed formation step (first step) followed by growth step (second step). The seed layer is grown during the first step process, in which seeds act as templates for the growth of crystal. For the proper growth of nanostructures, it is important to have proper nucleation all over the surface of fabric. Therefore, a polymer is a right choice to bind ZnO with the fabric surface. For the optimization of nanostructures, synthesis is carried out at different ratio, temperature and annealing time as shown in table 1,

and details are given for Ag1 as an example.

Table 1: Types of sample and their specifications

Sample	Ratio (ZN: HMT)	Growth time (h)	Annealing temperature (℃)
Ag1	1:2	1	60
Ag2	1:2	1	120
Ag3	3:1	1	60
Ag4	3:1	1	120
Ag5	1:2	5	60
Ag6	1:2	5	120
Ag7	3:1	5	60
Ag8	3:1	5	120

Seed formation (first step) for Ag1:

In the first step, a seed layer of ZnO was prepared by mixing the solutions of 0.1 M of Zinc nitrate hexahydrate [$Zn(NO_3)_26H_2O$] in 50 mL of distilled (DI) water and 0.2 M of Hexamethylenetetramine $(CH_2)_6N_4$ in 50 mL of DI water, and stirred the solution at 50°C for 2 h after immersing the Ag fabric. During the stirring process, the water turned milky color and the gray color fabric turned out to be whitish, indicating the formation of seeds over the fabric. Then, the solution containing the fabric was set in Teflon - lined autoclave for 1 h at 120°C and finally the sample is washed three times with DI water and then annealed at 60°C for 2 h., as shown in figure 1.

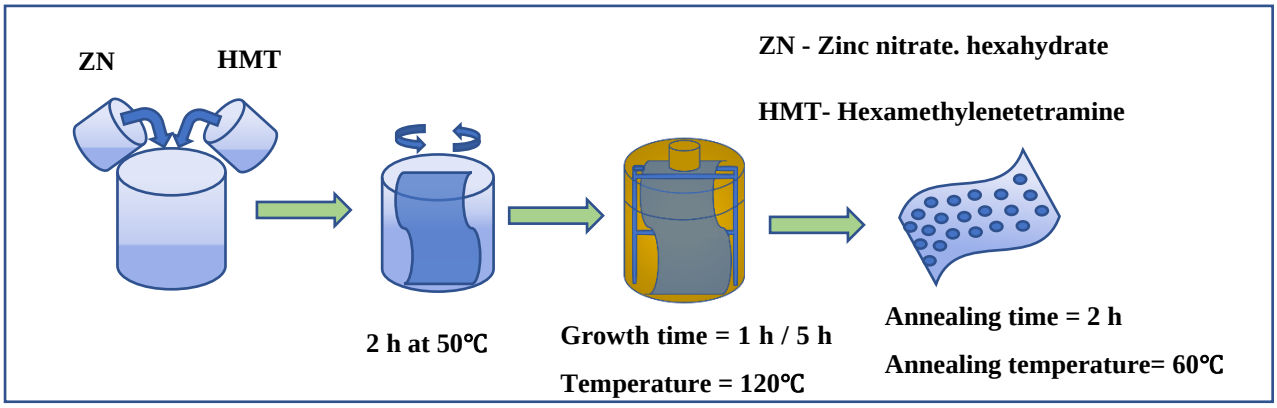

Figure 1: This figure shows the first step process

Nanostructure growth (second step) for Ag1: For the growth of nanostructures over the fabric, as a second step, solutions of molar ratio (1:2) of Zinc nitrate hexahydrate [$Zn(NO_3)_26H_2O$] and $(CH_2)_6N_4$ are mixed together and solution with seed layer formed in first step is stirred with the solution of 2 h at 50℃ and growth time set to 5 hours and finally the sample is washed three times with DI water and annealed at 50°C for 2 h, as shown in Fig2.

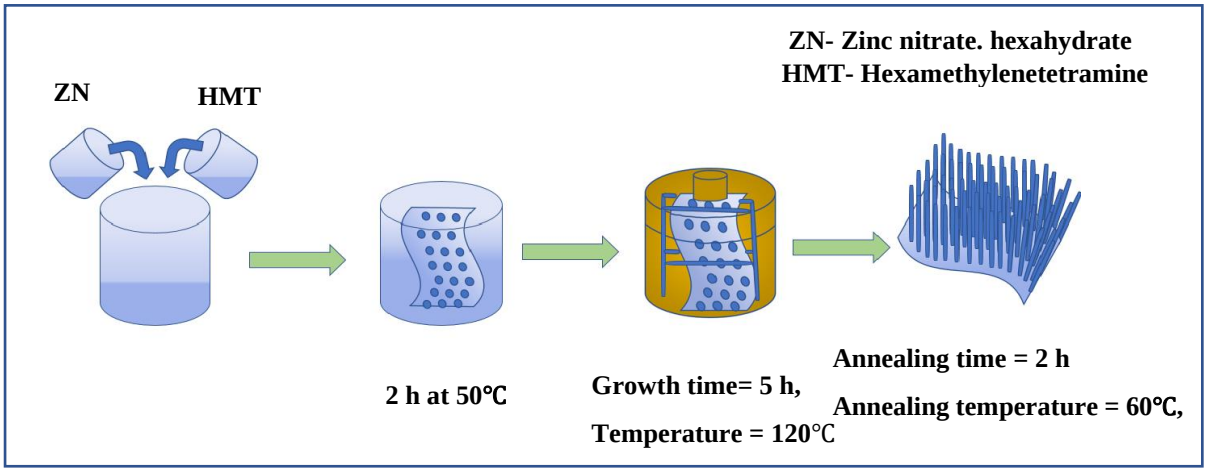

Figure 2: Shows the second step (growth) process for 50% Ag fabric

5.3. Result and discussion

5.3.1. Scanning electron microscope

Fig 3 shows that SEM images of bare (original) and first step ZnO seed layer over 50% Ag fabric. Fig 3(a), (b), (c) shows the images for the original fabric which illustrate that the fabric is defect-free and there is no impurity over the fabric's fiber. The Fig3(a) is intentionally fixed at different resolution, to show the full surface of the fabric. The diameter of fiber is estimated to be 10-15µm. Fig 3(d), (e), (f) illustrate the images of Ag 1, showing the best suitable condition, as the full surface is covered by the seed layer and nanorods of ZnO, depicted by the magnified image. Average size of rods is found to be in the range of nano to micro. Most of the nanorods are in perpendicular direction to the fabric's fiber. Fig 3(g), (h), (i), shows the images for Ag2, seed layer structure clearly visible, with some agglomerated particles of ZnO. Fig 3(j),(k),(l) shows the images for Ag3, in which finely formed hexagonal ZnO rods are visible, these rods having average diameter of 3-5µm. Finally Fig 3(m),(n),(o) show the images for Ag4, no ZnO nanorod is visible, but the fabric is wrapped with sheet like structure. Unlike previously with NCF and CAF, this fabric shows a nice formation of ZnO nanoseeds and nanostructures in all the conditions of 4(a)-(l), except that of Fig 4(j)-(l)which show some agglomeration between the particles. This scanning electron microscopy suggest the best choice, that is Ag1. Hence, we proceed for the second step only for the Ag1.

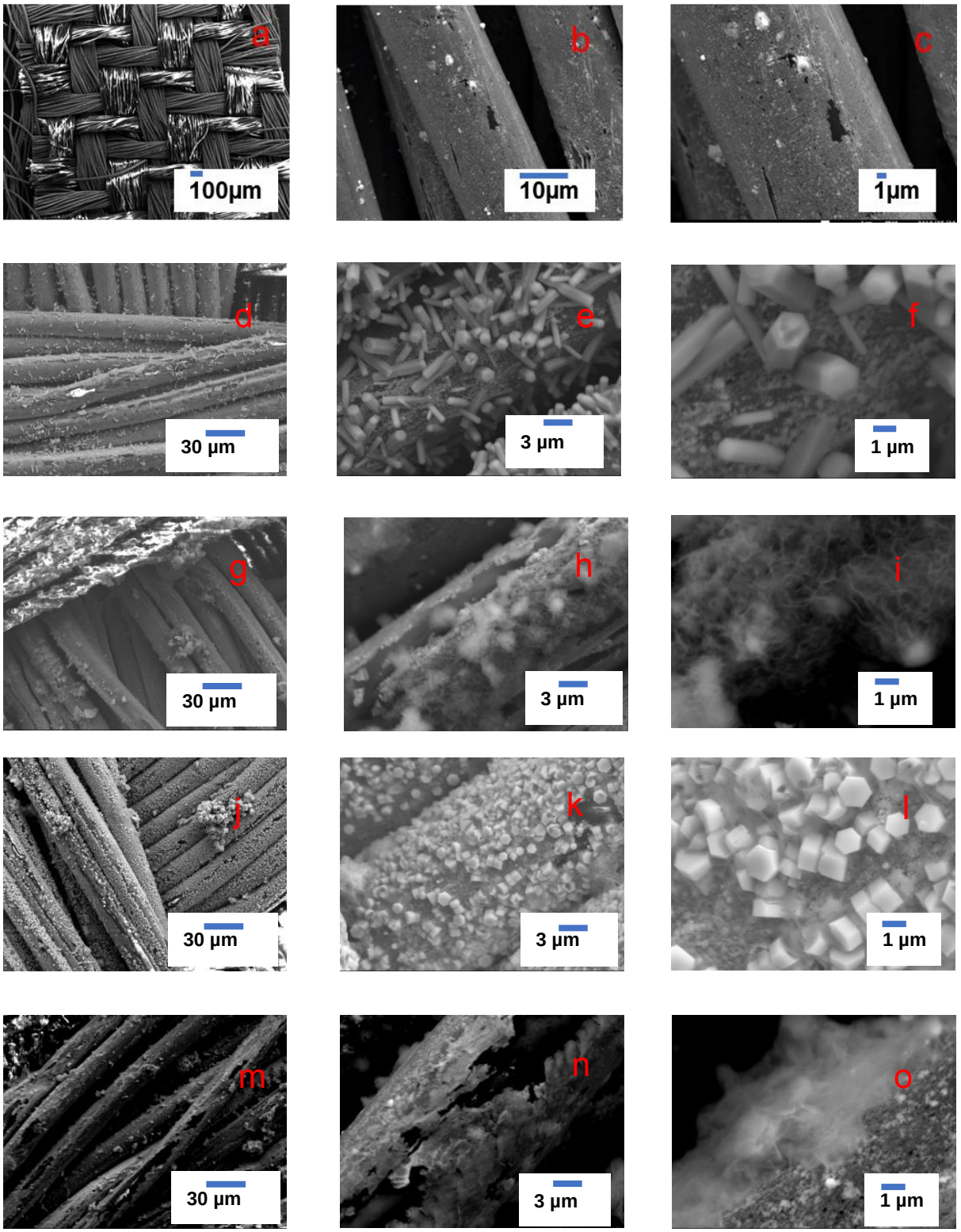

Figure 3: Show the SEM images of Ag to Ag4

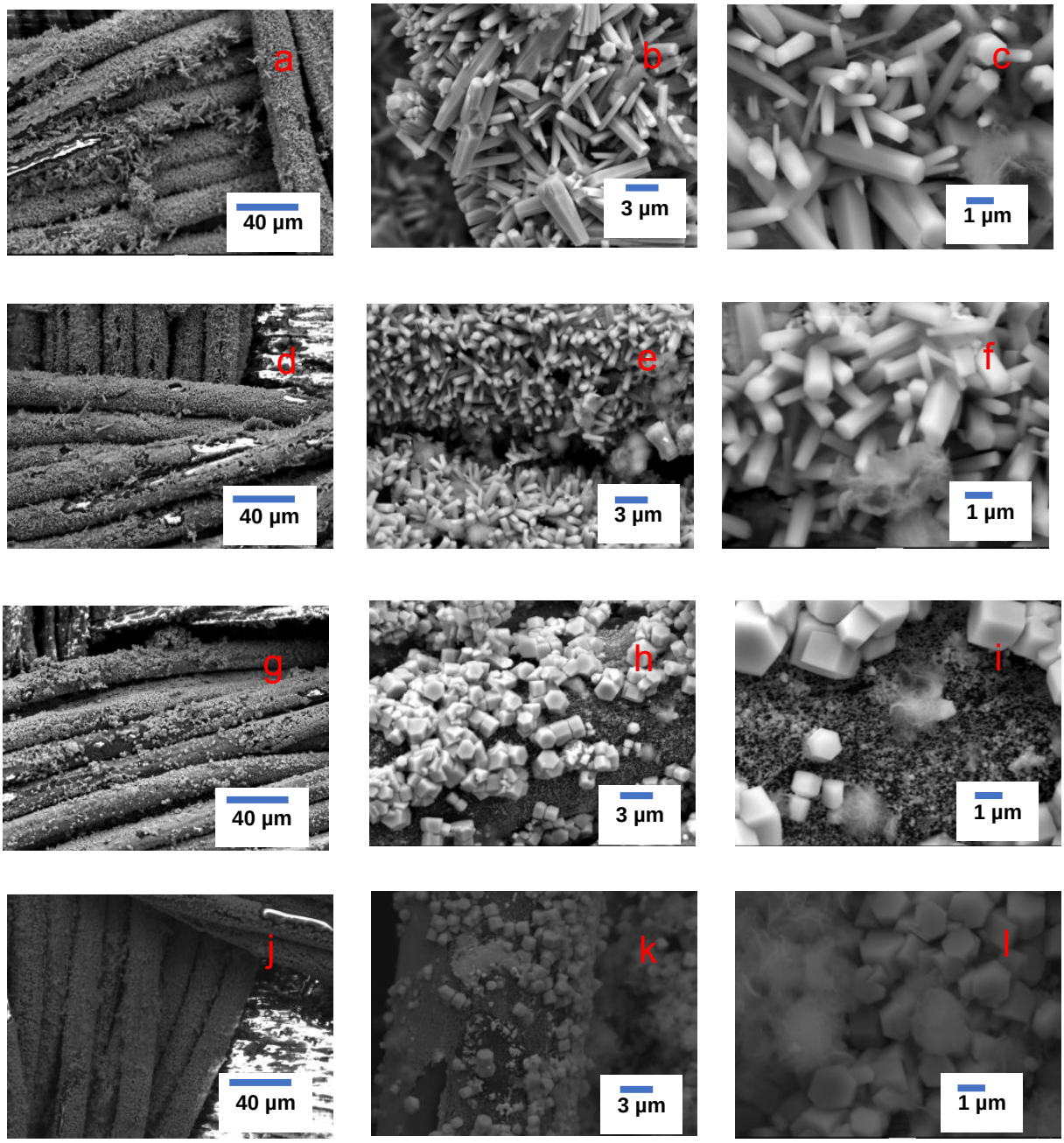

Figure 4: (a)-(c), (d)-(f), (g)-(i) and (j)-(l) show the SEM images of Ag5, Ag6, Ag7 and Ag8, respectively

Figure 5 shows the SEM images for the second step process for Ag1 at different zoom. It can be clearly seen that only a few nanorods have been grown over the surface of Ag, but almost full surface is covered with the thread/sheet like structures. The diameter and the length are almost same as grew in first step. However, the quantity and density of nanorods are increased.

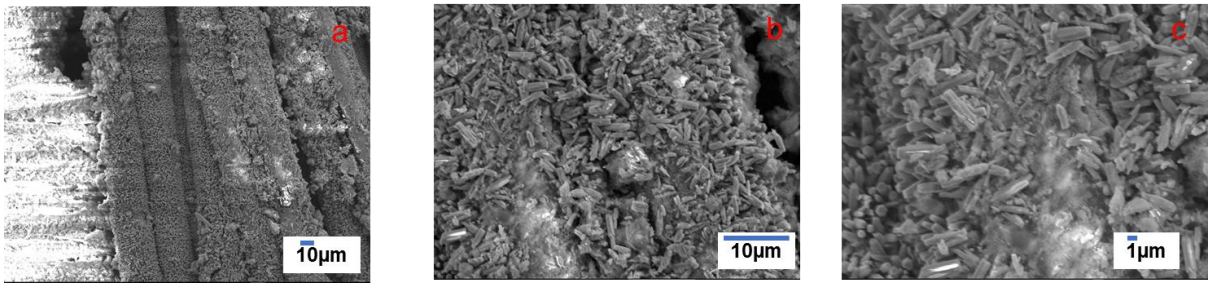

Figure 5: 5(a), (b), (c) shows the SEM images of second step ZnO / 50% Ag at different resolutions.

5.3.2. EDXA mapping

At this point, it is crucial to say which material Ag or nylon is favorable for ZnO adhesions. Chemical composition is analyzed by EDXA mapping technique. Fig 6(a)-(d) shows the EDXA mapping for original 50% Ag, in which image (d) clearly show the presence of Silver, similarly images from 6(e)-(i) shows the images for first step ZnO / 50% Ag, 6(j)-(n) show the images for second step ZnO / 50% Ag. The presence of Zn can clearly seen in 6(i), (n). As we move from first step to second step images get clear because of presence of more and more Zn and O content, present in ZnOH. However, images for Silver gets fainted due to the thick surface of ZnO over fabric. The percentage of elements present is shown by tables attached to graphs. Fig 7 shows that there is no impurity in the formed nanostructures.

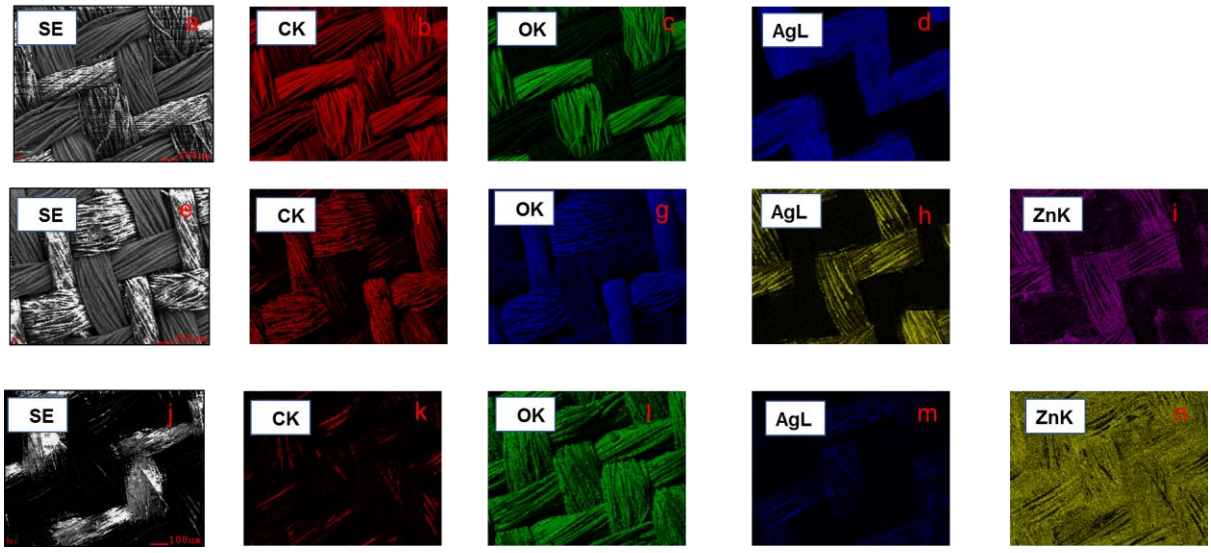

Figure 6: Mapping for original 50% Ag (a)-(d), 1st step ZnO / 50% Ag (e)-(i) and 2nd step ZnO /50% Ag(j)-(n).

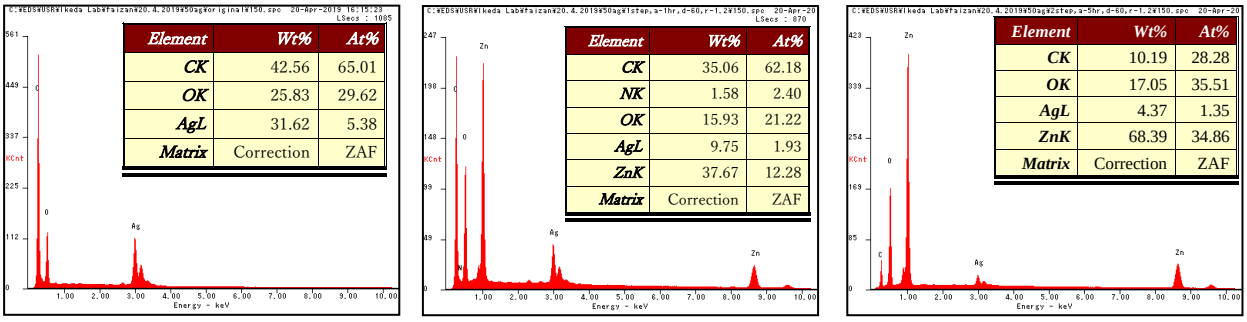

Figure 7: EDX analysis for (a) original Ag, (b) 1st step ZnO / 50% Ag, (c) 2nd ZnO / 50% Ag

5.3.3. X-ray diffraction (XRD)

Nano to micro-structured ZnO fabricated substrate is investigated by XRD technique (Fig 8). The conventional XRD is carried out in the range of 2θ form 20° to 80° According to standards of XRD (PXRD, Ref. No. 01- 087-0718, the peaks at 38.2º, 44.3º and 64.5º, 77.6º corresponds to the crystallographic planes of (111), (200) and (220) and (311) for face-centered cube(fcc) silver crystal, respectively[15]. Only one peak of ZnO at 36.100° is present in the 1st step. However, presence of nanostructured ZnO prominent peaks can be seen in 2nd steps more clearly, such as at 31.619°, 34.335°, 36.100°, 47.367°, 56.313°, 62.645° and 68.737° (JCPDS card no. 01-079-0208), however the sharp peaks visible only in the second step, show the crystallinity of ZnO material. Herein, the ZnO XRD patterns were indexed to the wurtzite structure of ZnO. Considering the ZnO nanorods' directions XRD results are perfectly matched with alignment of nanorods array on the surface of Ag observed in SEM images and EDAX graphs.

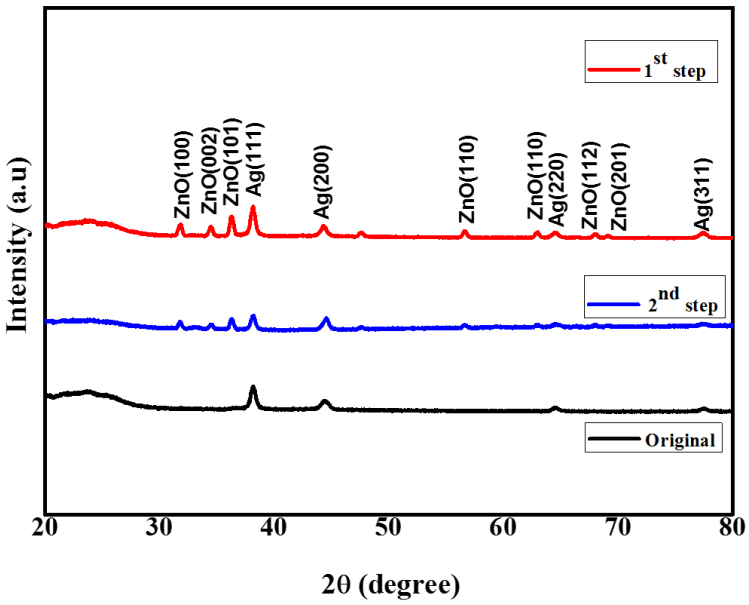

Figure 8: XRD graph for original 50% Ag, 1st step ZnO/ 50% Ag, 2nd step ZnO / 50% Ag

5.3.4. Seebeck Coefficient

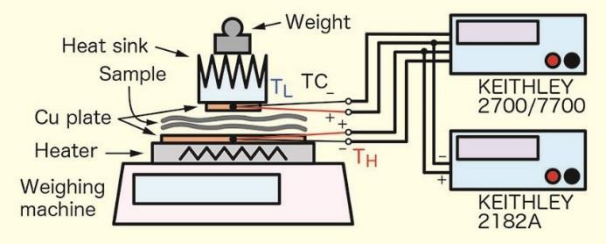

Figure 9 : Schematic diagram of developed Seebeck coefficient measurement system.

Like previous procedure, same procedure is applied again to find out the Seebeck coefficient of 50% Ag and fabricated 50% Ag fabric. An example of the time evolutions of TEMF, T_L and T_H for the Ag is shown in Fig. 10. It is clearly observed that the TEMF positively increases with an increase in the temperature difference ΔT. Figure 11 shows the relationship between TEMF and temperature difference replotted from Fig. 10. In this figure, "Increase" means the data collected from the range where the temperature difference is increasing, and "Decrease" corresponds to the data under decreasing the temperature difference in Fig. 10. Both "Increase" and "Decrease" data are nearly identical. This fact means that the measured data is reliable even for flexible materials. In addition, both data make a linear relation, indicating that the Seebeck coefficient is nearly constant in the measured temperature range. The Seebeck coefficient S was evaluated from the TEMF ($\Delta V = V_H - V_L$) and the temperature difference ($\Delta T = T_H - T_L$) by $S = -\Delta V / \Delta T$ near room temperature [16]. Therefore, the average Seebeck coefficient of Ag is evaluated from the gradient of the linear graph to be S^*_{Ag} ~ 0.43 μV/K, which is close to that of the same 50% Ag obtained in the horizontal direction, 0.245 μV/K using the apparatus shown in Fig 9 and described in previous chapters. Values of Seebeck coefficient are almost constant on increasing the number of layers, as shown in Fig 12, which is considered due to the high electrical conductivity of Ag. The Seebeck coefficient is positive, indicating that the Ag used is a p-type material (in opposition of the graph). The Seebeck coefficient phenomena is not fully understand yet and need more understanding about the calibration or phenomena

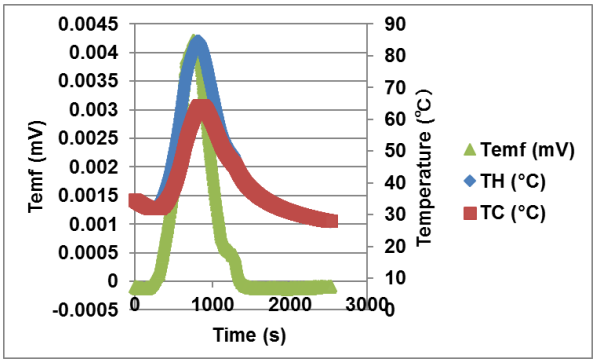

Figure 10: Time evolutions of TEMF and temperatures at hot T_H and cold T_L junctions for single Ag layer

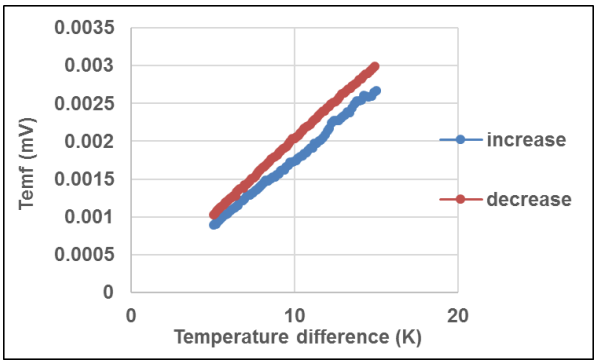

Figure 11: Relationship between TEMF and temperature difference for single Ag layer. "Increase" and "Decrease" correspond to the data collected from the range where the temperature difference is increasing and decreasing, respectively, in Fig. 10.

occurring. The vertical and horizontal Seebeck coefficients of these samples are summarized in Table 2. Almost all samples have positive Seebeck coefficients, or an p-type semiconductor. It is found that the Seebeck coefficient decreases by fabricating the ZnO on the 50% Ag. Considering that ZnO is usually an n-type semiconductor, the ZnO nanorod contributes to enhance the Seebeck coefficient in negative direction. As can be seen, Seebeck is decreasing more in the vertical direction, which is the obvious reason, i.e. double layer of ZnO over both sides of fabric.

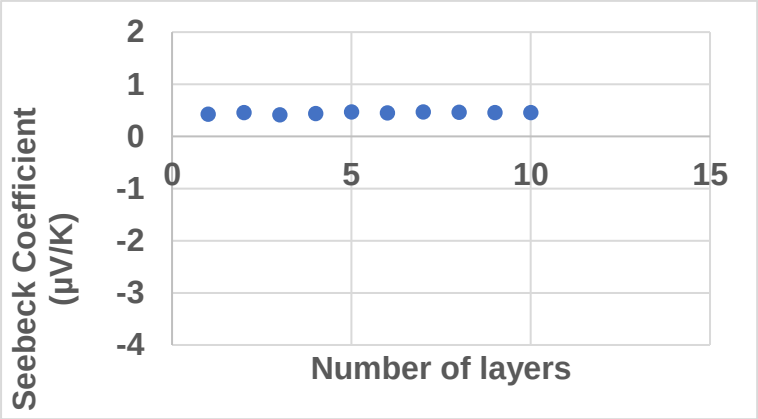

Figure 12: Relationship between Seebeck coefficient and the number of stacked Ag layers in vertical direction

Table 2: This table represents the Seebeck coefficient values of 50% Ag and ZnO / 50% Ag

Sample	S_{Vert} [μV/K]	S_{Horiz} [μV/K]
Original (50% Ag)	0.43	0.24
1st Step ZnO / 50%Ag	0.26	-1.15
2nd Step ZnO / 50%Ag	0.32	0.27

5.3.5. Laundering process

The same procedure of laundering is applied for this fabric also, just to check the adhesiveness of ZnO over the Ag substrate. This time also the fabricated fabric is sonicated 3 times for 5 min for each in 50 mL of DI water, then fabric is stirred in 100 mL of DI water for 2 hours, and finally dried at 60℃ for 2 hours. During this process, no detergent or soap is used, to avoid a chemical reaction during the laundering process. The details of the full process is described in the previous chapter. The weight of removed ZnO from the Ag fabric is calculated around 1.28 mg, these readings are the average of three readings, taking before and after of washing process. The adhesiveness of ZnO after laundering process is shown in SEM images of Fig 13, furthermore, the adhesion is confirmed by XRD as shown in Fig 14.

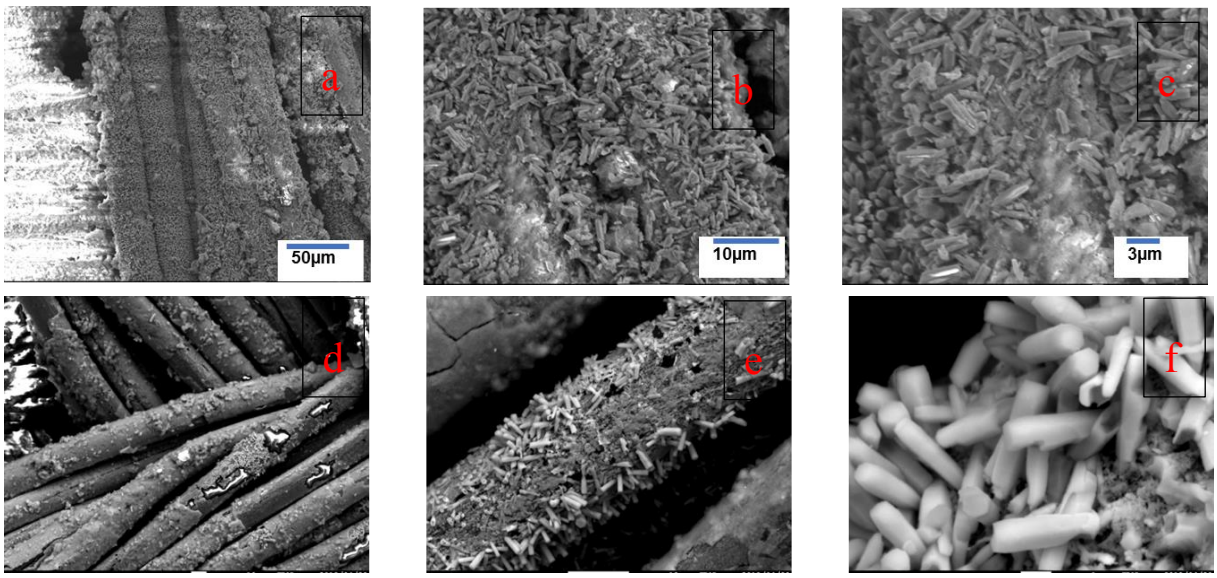

Figure 13: SEM images of 13(a)-(c) 2nd step ZnO / 50% Ag before laundering, 13(d)-(f) 2nd step ZnO / 50%Ag, after the laundering process

In addition, the same peaks of ZnO as observed for the 2nd step ZnO before laundering and after the laundering process can be seen in XRD patterns as shown in Fig 14. However, the peaks are reduced drastically, which may be attributed to removal of few ZnO from the substrate

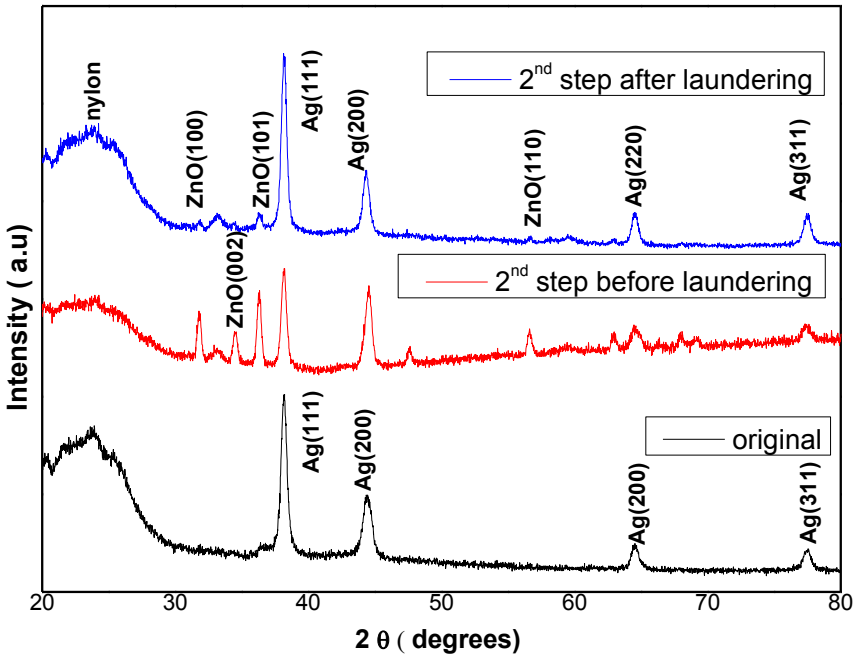

Figure 14: XRD patterns for original and ZnO formed 50% Ag after laundering effect

5.3.6. Electrical conductivity

With the aim of measuring electrical conductivity, the same home-made apparatuses are used for the measurement of 50% Ag fabric and ZnO fabricated Ag fabric with the same procedure as described in previous chapters. Current (A) is applied at the outer part of the electrode and voltage (mV) generated is measured through the inner electrodes. The I-V graph for single layer of Ag is shown in Fig 15.

$$R = \frac{\rho.L}{A} \qquad \text{.....(1)}$$

R= Resistance

L= Length between voltage leads (equal to thickness of fabric)

ρ = Resistivity of sample

Diameter, d = 0.47 cm

Radius, r = 0.235 cm

Area of circle, a = πr^2= 3.14 x $(0.235)^2$ = 0.173 cm^2

Area of sample = 1 cm^2

Effective area, A = Area of sample = 1 cm^2- 0.173 cm^2= 0.827cm^2

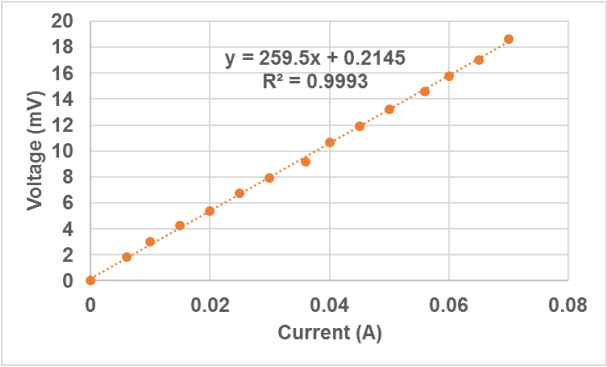

Figure 15: Evaluation of resistance for single layer of 50% Ag

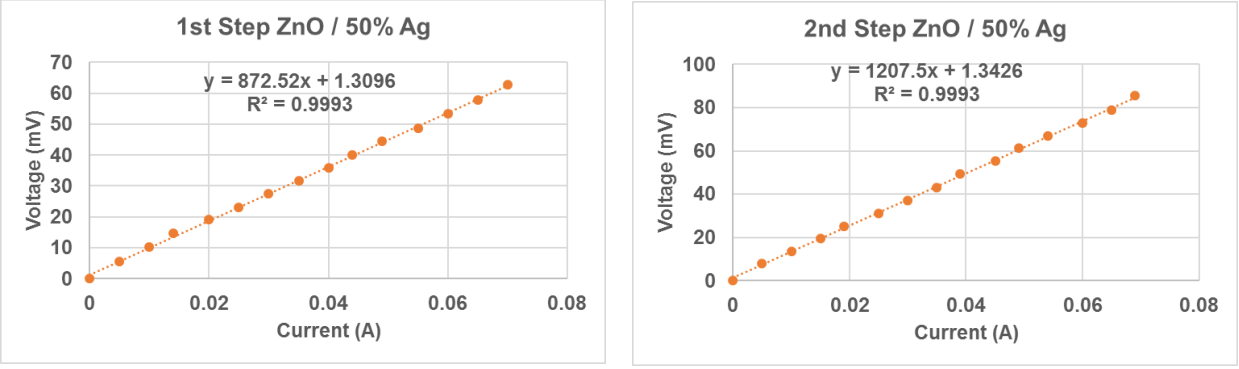

Figure 16: I-V graph to compare the resistance of 1st step ZnO/50%Ag and 2nd step ZnO/50% Ag in vertical direction.

The resistivity is calculated using the equation 1, described above. Table 3 explains the resistivities of original and ZnO fabricated sample. Further, the values of electrical resistivity are increasing on increasing the content of ZnO.

Table 3: This table explains the resistivity relation values for original and ZnO / 50% Ag.

Sample	Vertical resistivity (mΩ.m)
Ag original	143.07
1st ZnO/Ag	481.04
2nd ZnO/Ag	665.7

5.4. Fabrication of rGO on 50% Ag

The same procedure as proceeded for other two fabrics has been chosen for the fabrication of rGO on 50% Ag fabric. Same concentration and same chemicals were used in this process, GO followed by rGO.

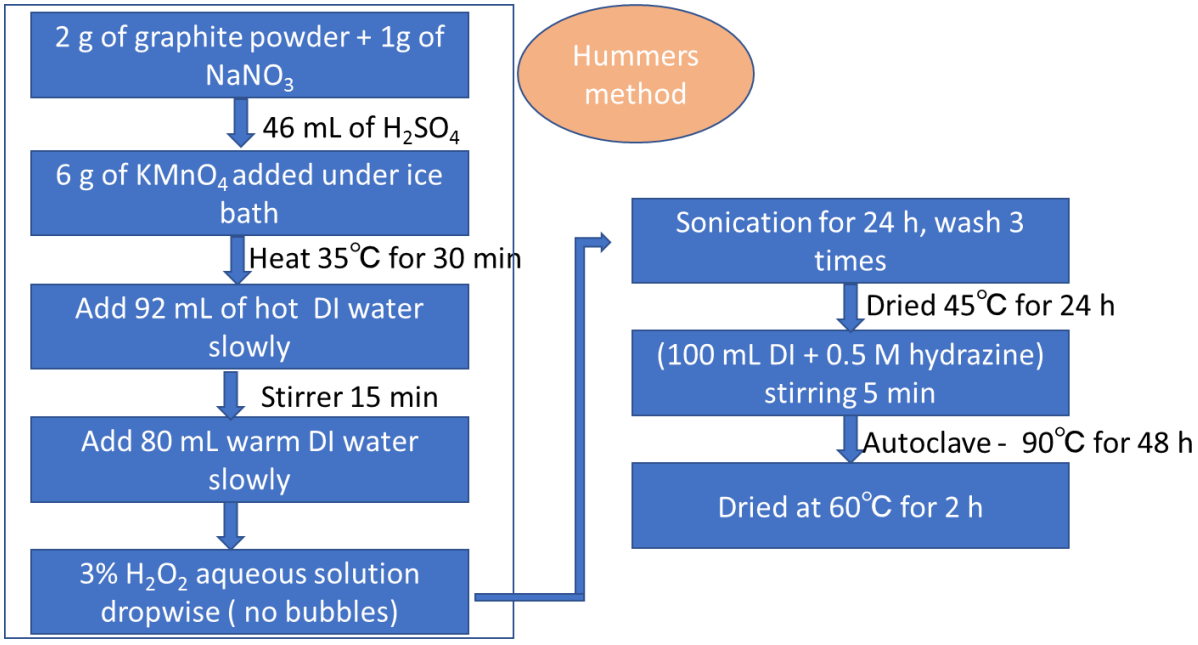

Figure 18: Flow chart of rGO synthesis

5.5. Result and discussion

5.5.1. Scanning electron microscopy (SEM)

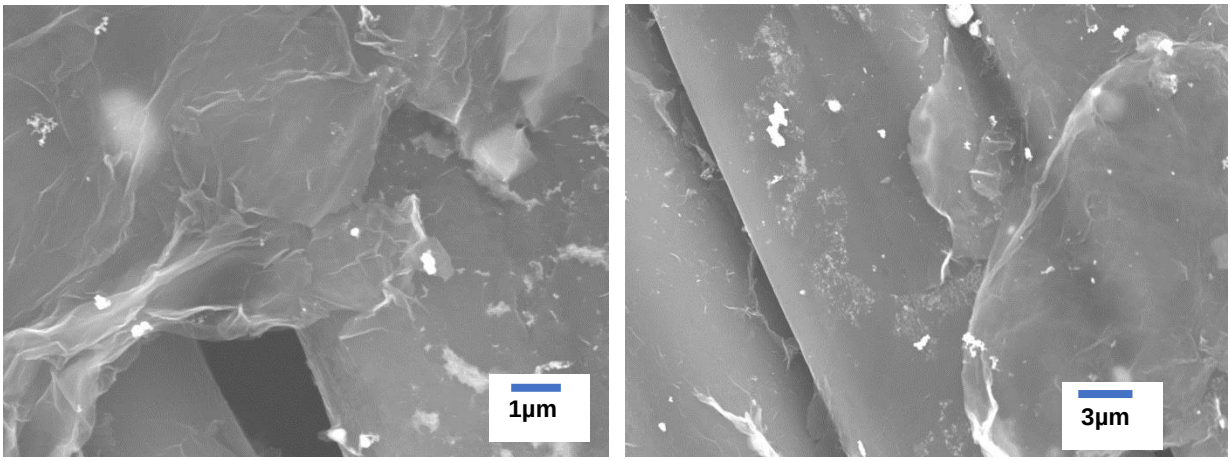

Figure 19: SEM images of rGO on 50% Ag

Clear images of SEM depict the morphology of formed rGO on the surface of the fabric. It is clearly visible that the fabric is fully covered with the formed rGO sheets and the sheets appeared to be transparent. These rGO sheets cover the whole fabric irrespective of presence of Ag or nylon, which suggest that both the materials are equally favorable for the formation of rGO over the surface. However adhesion behavior or the chemical reaction between Ag or nylon and the rGO is still unknown at this stage and further investigation is required.

5.5.2. X-ray diffraction

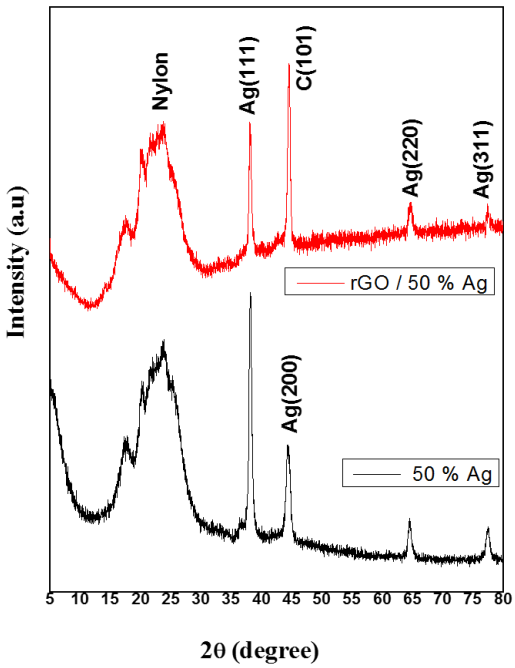

Figure 20: XRD graph for rGO / 50% Ag

XRD of the rGO fabricated sample shows almost identical peaks of Ag at 38.2º, 44.3º and 64.5º, 77.6º corresponding to the crystallographic planes of (111), (200) and (220) and (311) for face-centered cube (fcc) silver crystal, respectively with a single peaks of

rGO which is overlapping with Ag (200) peak at 44.3º. However, there is less intensity of the peak at 38.2º, which is due to the insertion of Ag atoms inside the aromatic ring of rGO.

5.5.3. Seebeck coefficient

Seebeck values for rGO / 50 % measured in vertical direction is found to increase drastically in comparison to original values of the fabric. The fabric after fabrication with rGO shows strong p-type semiconductor effect. Seebeck values in vertical direction after fabrication are approximately 5.59 µV/K.

Table 4: Seebeck values for rGO / 50% Ag

Sample	S_{vert} [µV/K]
Original	0.43
rGO / 50 % Ag	5.59

5.5.4. Electrical resistivity

Fig 21 shows, the I-V relationship of the formed rGO on the silver fabric. Resistance is found to be 166061 mΩ and the resistivity is calculated to be ~ 91554.96 mΩ.m. Some of the reporters suggested that the graphene oxide is not conductive, and the reason of its insulator type behavior is because of absence of π- conjugated orbital system. This conductive behavior of rGO suggests that the extensive conjugated sp^2 carbon network may be restored in the formed rGO.

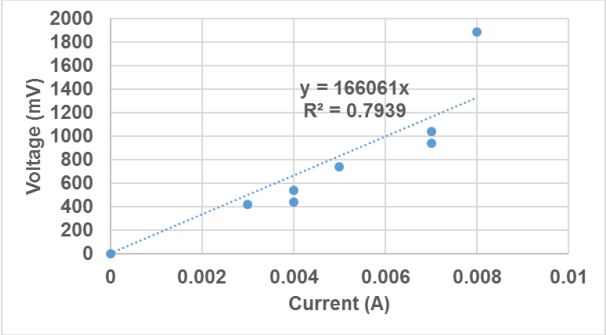

Fig 21: Evaluation of electrical resistance for rGO on CAF

5.6. Summary

To increase the efficiency of thermoelectric power generators and ZT values, highly conductive Ag was chosen as a flexible material. Highly crystalline and closely packed ZnO nanostructures were fabricated on Ag. At different ratios and growth time, different structures were obtained. Seebeck coefficient were measured in horizontal and vertical directions using our home-made apparatuses. Effect of air gaps is checked by staking large number of layer and Seebeck is measured in vertical direction. It is found that on increasing the number of layers, Seebeck is almost constant. Similarly, Seebeck values are measured for the single layer of 50%Ag with and without ZnO fabrication and the values were compared against horizontal direction. It is found that the Seebeck coefficient decreases by fabricating the ZnO on the 50% Ag. Considering that ZnO is usually an n-type semiconductor, the ZnO nanostructures contribute to enhance the Seebeck coefficient. SEM analysis is done to find out different morphologies. It is found from SEM images that there are crystalline nanorods are grown on the fabric surface which may be attached to it through physisorption only. Furthermore, the adhesiveness of ZnO nanostructures is also checked by a laundering process. Around 1.28 mg of ZnO nanorods per 1 cm^2 of substrate are removed by the laundering process. High crystallinity and hexagonal structures of nanostructure were depicted by XRD analysis. The electrical resistivity in the vertical direction of 50% Ag before and after fabrication have been evaluated. It is found that after fabrication of 50% Ag with ZnO nanostructures the electrical resistivity increased from 143.07 mΩ.m to 665.7 mΩ.m, compared against Hall effect instrument.

Reduced graphene oxide sheets have been prepared on the surface of 50% Ag, SEM images show the morphology of sheets are thin and transparent in nature. Seebeck values reach up to 5.59 µV/K and the fabric shows p-type semiconductor behavior. Electrical resistivity after fabrication of rGO on fabric is found to be 91554.96 mΩ.m.

Reference:

1. R.N. Caron, Copper: Alloying, Encyclopedia of Materials: Science and Technology, 2001
2. Rosenblatt. A, Stamford T.C, Niederman R. "Silver diamine fluoride: a caries "silver-fluoride bullet". Journal of Dental Research. 88 (2): 116–25, 2009.
3. Maillard, Jean-Yves; Hartemann, Philippe, "Silver as an antimicrobial: Facts and gaps in knowledge". Critical Reviews in Microbiology. 39 (4): 373–83, 2012.
4. Hammond, C. R., The Elements, in Handbook of Chemistry and Physics (81st ed.). CRC press, 2004.
5. BullionVault, "A Big Source of Silver Bullion Demand Has Disappeared", Retrieved 20, July 2014.
6. D. Kojda, R. Mitdank,1 M. Handwerg, A. Mogilatenko, M. Albrecht, Z. Wang, J. Ruhhammer, M. Kroener, P. Woias and S. F. Fischer, Temperature-dependent thermoelectric properties of individual silver nanowires, PHYSICAL REVIEW B 91, 024302, 2015.
7. Haiyu Fang, Haoran Yang, and Yue Wu, Thermoelectric Properties of Silver Telluride−Bismuth Telluride Nanowire Heterostructure Synthesized by Site-Selective Conversion, Chem. Mater. 2014, 26, 3322−3327, 2014.
8. Vogler. H, "Wettstreit um die Polyamidfasern". Chemie in unserer Zeit. 47: 62–63, 2013.
9. "Nylons (Polyamide)". British Plastics Federation. Retrieved 19 June 2017.
10. L.D. Hicks and M.S. Dresselhaus, “Thermoelectric figure of merit of a one-dimensional conductor,” Phys. Rev. B, 47, 16631– 16634, 1993.
11. D. Li, Y. Wu, P. Kim, L. Shi, P. Yang, and A. Majumdar, “Thermal conductivity of individual silicon nanowires,” Appl. Phys. Lett., 83, 14, 2934–2936, 2003.
12. N. Neophytou and H. Kosina, “Effects of confinement and orientation on the thermoelectric power factor of silicon nanowire,” Phys. Rev. B, 83,24, 245305-1–16, 2011.
13. Ravi Raj Vankayala, Wei-Jen Petrick Lai, Kuo-Chung Cheng, Kuo Chu Hwang, Enhanced electrical conductivity of nylon 6 composite using polyaniline-coated multi-walled carbon nanotubes as additives Polymer 52, 3337-3343, 2011.
14. F. Heidarpour, W. A. Wan ab. Karim ghani, F. R. Bin ahmadun, S. Sobri, M. Zargar, M. R. Mozafari, nano silver-coated polypropylene water filter: I. Manufacture by electron beam g un using a modified balzers 760 machine digest journal of nanomaterials and biostructures , 5, 3, 787-796, 2010.
15. F. Khan, V. Pandiyarasan, S. Sakamoto, M. Navaneethan, M. Shimomura, K. Murakami, Y. Hayakawa and H.Ikeda, Seebeck Coefficient of Flexible Cabon Fabric for Wearable Thermoelectric Device, IEICE TRANS. ELECTRON., E101-C, 5, 343-346, 2018.

Chapter 6 - Comparison Between All Combination of Oxide Semiconductors and Fabrics

With the intention of explaining the results more clearly and concretely, we have gathered all data (in vertical direction) in the form of different tables. From table 1, we can see that NCF is showing negative values of Seebeck coefficient which may be because of higher concentration of nickel inside the fabric. While CAF and 50% Ag show p-type structure by showing positive values of the Seebeck coefficient. Resistivities of all fabric show low values among which CAF shows the least and 50% Ag shows highest value. However, table 2 and 3 show the corresponding values of 1st step ZnO/fabric and 2nd step ZnO/fabric, respectively. These tables suggested that on increasing the content of ZnO, Seebeck values are getting lower, and the minimum value is found for NCF that is – 4.5 μV/K, this effect is due to the n-type nature of ZnO. As the measurement is in vertical direction, therefore, longer will be the nanorods higher will be the temperature difference and hence higher will be the effect of ZnO. Power factor is found to decrease in every fabric with the fabrication with ZnO micro-nanostructures, which is due to heavy increase in the electrical resistivity.

Table 1: comparison between Seebeck values, resistivity and power factor of all three original fabrics

Original fabric	NCF	CAF	50% Ag
Seebeck coefficient (μV/K)	-2.7	5.05	0.43
Resistivity (mΩ.m)	111.4	100.8	143.07
Power factor (nW/K^{2}m)	0.065	0.253	0.0012

Table 2: comparison between Seebeck values, resistivity and power factor of all three 1st step ZnO / fabrics

1st step ZnO / fabric	NCF	CAF	50% Ag
Seebeck coefficient(μV/K)	-3.4	4.95	0.26
Resistivity (mΩ.m)	414.66	169.5	481.04
Power factor (nW/K^{2}m)	0.02	0.144	0.0001

Table 3: comparison between Seebeck values, resistivity and power factor of all three 2nd step ZnO / fabrics

2st step ZnO / fabric	NCF	CAF	50% Ag
Structure	Nanorods-microrods	Nano-sheets	Nanorods-microrods
Seebeck coefficient	-4.5	4.98	0.32
Resistivity (mΩ.m)	1862.4	725.4	665.7
Power factor (nW/K^{2}m)	0.010	0.034	0.0001

However, in case of rGO on the fabric, NCF shows the n-type behavior while CAF and 50%

Ag show the p-type behavior. High Seebeck values may be attributed to the insertion of copper particles stuck inside the hexagonal ring of rGO. Seebeck coefficient values for CAF is almost equal, which shows the maximum effect is because of carbon substrate only and not because of the material deposited or because of less deposition of rGO on the surface of carbon. However, the power factor is found to decrease in all fabrics.

Table 4: Comparison between Seebeck values of rGO / fabrics

rGO/ fabric	**NCF**	**CAF**	**50%Ag**
Seebeck coefficient(μV/K)	-17.08	4.7	5.59
Resistivity (mΩ.m)	11620.8	717.41	91554.96
Power factor (nW/K^2m)	0.025	0.006	0.0003

Chapter 7: Final Summary and Future Scope

7.1. Conclusion

Due to significant energy crisis, it has been a serious issue to think about the control of resources to fulfil our daily needs. One way to live happy life is to save more energy and use it efficiently. Another way is to produce more energy and use more but appropriately. Therefore, we have focused our attention on thermoelectric generators (TEGs) so that we can utilize waste heat and produce electricity for our daily electronic gadgets. But, the working of TEGs are strictly dependent on efficiency, which depends on figure of merit (ZT). Hence, with the aim of developing new material that can enhance the efficiency and hence ZT, we have focused our attention towards ZnO and rGO nanomaterials. These materials should enhance the Seebeck coefficient values while decreasing thermal conductivity altogether, due to charge and phonon confinement effect. In our laboratory, we have already investigated the effect of nanostructured ZnO and rGO over cotton fabric. As cotton is an insulator, electrical conductivity was a matter of concern. In this thesis, we have successfully fabricated nanostructured ZnO and rGO over three different conducting fabrics using two-step hydrothermal method. Different parameters such as concentration ratio, growth time, annealing temperature are optimized to grow fine and perpendicular micro-nanorods. The morphology the formed nanostructures are analyzed by XRD, SEM and EDXA spectroscopy. It has been found from the XRD spectrum that the highly crystalline nanostructures are grown with hexagonal phase and the direction of formed ZnO is in the vertical direction of the fabric's fiber. SEM images confirm the formation of nanorods with different diameter and different lengths. EDXA analysis confirms the presence of different material in different regions of the fabric. Furthermore, the Seebeck coefficient and electrical conductivity of original and prepared nanostructures over the fabric is measured by home-made apparatus in vertical direction, and the values are compared along the horizontal direction. It has been found that the Seebeck coefficient of original carbon fabric and silver fabric is positive, showing p-type behavior, however, n-type for original nickel-copper fabric. Further, the layer and weight effect are analyzed by putting different layers and different weights to see the effect of air gaps and pressure, respectively. It has been found that Seebeck values increases with increases number of layers of fabric, however, it is independent of amount of weight over the fabric. Similarly, electrical resistivity is measured by our home-made apparatus in the vertical direction. For the confirmation of electrical resistivities, values are compared with the values measured by Hall effect instrument. In addition, it is found that resistivity of the fabric has been increased on fabricating with ZnO and rGO.

7.2. Detection Limits

During the construction of Seebeck coefficient measurement, we went through different hurdles, such as selection of electrode material, material for the validation of instrument, e.t.c. Still some of the problems go unresolved. For example, although the electrodes, thermocouple wire, voltmeter, power source and other instruments, are identical for both the instrument, vertical direction and horizontal direction, the vertical direction instrument shows a null value of -0.6 μV/K. That is, according to the basics of Seebeck it is not possible to generate voltage if you connect two wires of the same type, mathematically,

$$\Delta V = \int_{T_L}^{T_H} [S_X - S_r]\, dT$$

Where

ΔV is the voltage generated, S_x and S_r are the Seebeck coefficient of sample and reference material, respectively. Hence, if S_X will be equal to S_r, then ΔV should be zero. Secondly, there is very less voltage generated in the vertical direction between the top and bottom surface to the material, hence it is very difficult to measure the Seebeck coefficient of metal in this direction, with some exception of metals like lead.

7.3. Future Scope

At this level the thermoelectric values of ZnO and rGO along with the fabrics are still not showing enough values for the application of wearable power generators (WTEG), these values can be further enhanced by the process of doping inside the ZnO or rGO nanostructures. From the electronics point of view also, it is possible to increase the efficiency of TEG, hence with the aim of improvement of efficiency for WTEG, we tried a little bit to form a small amplifier based on Joules Thief Theorem. Maximum of 148 V volts has been created by using 9 V battery. Hence, integration of WTEG with some amplifier that can enhance voltage level from microvolts to millivolts can be a fruitful idea for the generation of large voltages. With the aim of preparing WTEG, we have created WTEG with only bare fabrics so far using cotton as a base and NCF and CAF as a n-type and p-type materials, respectively. The prepared WTEG produced maximum voltage of 0.27 mV at a temperature difference of 6℃.